

IDENTIFICATION OF METAL LIGANDS IN AMICYANIN, HEMOCYANIN AND CATALASE
BY RESONANCE RAMAN SPECTROSCOPY

Kamala Devi Sharma
B.S., Meerut University (INDIA), 1970
M.S., Meerut University (INDIA), 1973
M.S., University of Oregon, 1983

A dissertation submitted to the faculty
of the Oregon Graduate Center
in partial fulfillment of the
requirements for the degree
Doctor of Philosophy
in
Biochemistry
August, 1988

The dissertation "Identification of Metal Ligands in Amicyanin, Hemocyanin, and Catalase by Resonance Raman Spectroscopy" by Kamala Devi Sharma has been examined and approved by the following Examination Committee:

Thomas M. Loehr, Thesis Research Advisor
Professor

Jeann Sanders-Loehr, Thesis Research Advisor
Professor

James K. Hurst
Professor

William Fish
Assistant Professor

ACKNOWLEDGEMENT

From the bottom of my heart I wish to express my unfathomable gratitude and thanks to my thesis advisors, Professor Thomas M. Loehr and Professor Joann Sanders-Loehr for their wonderful guidance, helpful comments, suggestions, and for providing me with the encouragement in an intellectually stimulating environment to pursue my goals. I credit any success that I have experienced during these last four and a half years of work to the patience and nurturing of my two advisors. I thank Laura A. Andersson for guiding me through the earlier part of my research. Thanks are due to Andrew K. Shiemke, William D. Wheeler and Scott S. Sibbett for their instruction and help in running the spectrophotometer.

I owe special thanks to Nancy Christie and Madeline Dalrymple for their moral support. Finally, I thank my husband, Eddie D. Griswold, for his support and confidence in me. Special thanks to him for his beautiful drawings for my thesis.

DEDICATION

To my parents

Late Tulasi R. Sharma and late Ganga D. Sharma

TABLE OF CONTENTS

	Page
ACKNOWLEDGEMENT	iii
LIST OF TABLES	ix
LIST OF FIGURES	xi
ABSTRACT	xv
CHAPTER I: METHODS FOR CHARACTERIZING METAL COORDINATION SITES IN PROTEINS	
Introduction	1
Absorption Spectroscopy	2
X-ray Crystallography	3
X-ray Absorption Spectroscopy	5
Nuclear Magnetic Resonance Spectroscopy	7
Electron Paramagnetic Resonance Spectroscopy	9
Resonance Raman Spectroscopy	12
References	20
Tables	27
Figure Legends	32
Figures	34
CHAPTER II: EXPERIMENTAL METHODS	41
Catalase Preparations	42

Cytochromes c_1 and c	47
Copper Complexes	48
Iron Complexes	49
Factors Affecting Resonance Raman Scattering Intensity	50
Quantitation of Depolarization Ratios	54
References	56
Tables	58
Figure Legends	61
Figures	63
CHAPTER III: RESONANCE RAMAN SPECTROSCOPY OF AMICYANIN,	
A BLUE COPPER PROTEIN FROM <u>Paracoccus denitrificans</u>	
Introduction	68
Experimental Procedures	72
Results and Discussion	73
References	78
Tables	81
Figure Legends	84
Figures	85
CHAPTER IV: RESONANCE RAMAN SPECTROSCOPY OF OXYHEMOCYANIN.	
ISOTOPE EFFECTS DUE TO SOLVENT HYDROGEN AND OXYGEN	
Introduction	87
Experimental Procedures	91
Results and Discussion	99
Conclusions	103
References	105

Tables	109
Figure Legends	110
Figures	113
CHAPTER V: RESONANCE RAMAN SPECTROSCOPY OF IN MAMMALIAN, FUNGAL AND MICROBIAL CATALASES. EVIDENCE FOR IRON-TYROSINATE COORDINATION	
Introduction	123
Materials and Methods	126
Results and Discussion	130
References	139
Tables	144
Figure Legends	149
Figures	153
CHAPTER VI: RESONANCE RAMAN SPECTRA OF 5-(2-HYDROXYPHENYL)-10,15, 20-(TRITOLYL)IRON(III)PORPHYRIN AND ITS DIMERIC COMPLEXES	
Introduction	158
Material and Methods	161
Results and Discussion	162
References	169
Tables	171
Figure Legends	173
Figures	175

APPENDIX:	RESONANCE RAMAN STUDIES OF CYTOCHROMES C_1 AND C_2 .	
	A COMPARATIVE STUDY WITH AND WITHOUT HINGE PROTEIN	
	Introduction	181
	Materials and Methods	182
	Results and Discussion	183
	References	188
	Tables	189
	Figure Legends	191
	Figures	193
BIOGRAPHICAL NOTE		197

LIST OF TABLES

		Page
CHAPTER I.		
Table I.	Electronic Absorption Spectra of Metalloproteins.	27
Table II.	Metal-Binding Sites Identified by X-ray Crystallography.	28
Table III.	Comparison of Plastocyanin Copper-ligand Distances Obtained by X-ray Crystallography and EXAFS.	29
Table IV.	EPR Properties of Metal Ions Found in Biochemical Systems.	30
Table V.	Structure Sensitive Vibrational Modes of Heme Proteins.	31
 CHAPTER II.		
Table I.	Effect of Sampling Geometry and Light Polarization of the Intensity of CCl_4 Modes.	58
Table II.	Comparison of Raman Peak Heights of $\nu_1(\text{NO}_3^{-1})$, $\nu_1(\text{SO}_4^{2-})$, and $\nu(\text{Cu-S})$ of Amicyanin at a Constant Excitation Power and Constant Plot Gain.	60
 CHAPTER III.		
Table I.	Resonance Raman Vibrational Frequencies for Azurins, Plastocyanin, and Amicyanin.	81
Table II.	Overtone and Combination Bands (in cm^{-1}) in the Resonance Raman Spectrum of <u>P. denitrificans</u> Amicyanin.	83
 CHAPTER IV.		
Table I.	Assignment of Resonance Raman Vibrational Modes in Hemocyanin from <u>Busycon canaliculatum</u> .	109

CHAPTER V.		
Table I.	Raman Frequencies for Catalases from Bovine Liver (BL), <i>A. niger</i> (AN), and <i>M. luteus</i> (ML), and from High-spin Ferric Porphyrins.	144
Table II.	Characteristic Raman Frequencies for Ferric Phenolates.	147
CHAPTER VI.		
Table I.	Resonance Raman Frequencies (cm^{-1}) and Assignments for (TTOPH)FeCl, [(TTOP)Fe] ₂ , (TPPFe) ₂ O, and (TPPFe) ₂ N complexes.	171
APPENDIX.		
Table I.	Key Resonance Raman Frequencies (in cm^{-1}) for Heme Proteins.	189
Table II.	Vibrational Frequencies (in cm^{-1}) of all the Samples.	190

LIST OF FIGURES

		Page
CHAPTER I.		
Figure 1.	Electron density map of a tyrosine residue of rubredoxin showing the dependence of structural details on the resolution and phase refinement.	34
Figure 2.	EXAFS of reduced and oxidized copper in plastocyanin.	35
Figure 3.	300-MHz ^1H NMR spectra of pink and purple uteroferrin (1 mM) in 100 mM sodium acetate buffer, pH 4.9, at 30° C.	36
Figure 4.	EPR spectra of the fluoride and azide complexes of horse erythrocyte catalase.	37
Figure 5.	EPR spectra of ferrous manganese peroxidase with ^{14}NO and ^{15}NO and of ferrous horseradish peroxidase with ^{14}NO and ^{15}NO .	38
Figure 6.	Resonance Raman spectrum of purple acid phosphatase.	39
Figure 7.	Resonance Raman spectrum of spinach ferredoxin.	40
CHAPTER II.		
Figure 1.	Fluorescence spectra of bovine liver catalase, 1.2 μM in 0.05 M phosphate buffer (pH 7.05).	63
Figure 2.	Use of spinning sample holder for solid samples at room temperature.	64
Figure 3.	Effect of grinding time on the intensity of the ν_1 mode of sulfate and nitrate salts.	65
Figure 4.	Instrumental setup for the measurement of depolarization ratio of a liquid sample using 90° scattering and 150° back-scattering geometry.	66

Figure 5.	Raman spectra of CCl_4 at room temperature obtained with the broadband polarizer (analyzer) in the "Not Cut Down" (NCD) or parallel and "Cut Down" (CD) or perpendicular orientations.	67
CHAPTER III.		
Figure 1.	Resonance Raman spectrum of <u><i>P. denitrificans</i></u> amicyanin in the low frequency region.	85
Figure 2.	Resonance Raman spectra of <u><i>P. denitrificans</i></u> amicyanin in the overtone and combination region.	86
CHAPTER IV.		
Figure 1.	(A) Active site structure of deoxy hemocyanin based on X-ray crystallography. (B) Proposed structures for deoxy and oxy-hemocyanin.	113
Figure 2.	(A) Channeled whelk (<u><i>Busycotypus canaliculatum</i></u>). (B) Cross-section of <u><i>Hexis aspersa</i></u> , a related gastropod.	114
Figure 3.	Arrangement of passing Ar gas through the sample of hemocyanin for its anaerobic reduction.	115
Figure 4.	Mass spectra to determine ^{18}O content of hemocyanin sample.	116
Figure 5.	Closed-cycle helium Displex used to obtain Raman spectra at 15 K.	117
Figure 6.	Absorption spectrum of oxyhemocyanin.	118
Figure 7.	Raman spectra of oxyhemocyanin with visible excitation.	119
Figure 8.	Raman spectra of oxyhemocyanin in H_2O and D_2O with visible excitation.	120
Figure 9.	Raman spectra of oxyhemocyanin in H_2O and H_2^{18}O with UV excitation at 363.8 nm.	121

Figure 10.	Low frequency Raman spectra of oxyhemocyanin in H ₂ O and H ₂ ¹⁸ O with UV excitation at 363.8 nm.	122
CHAPTER V.		
Figure 1.	High frequency RR spectra of bovine liver catalase with visible excitations.	153
Figure 2.	High frequency RR spectra of <u>A. niger</u> with Soret and visible excitations.	154
Figure 3.	High frequency RR spectra of native and cyano-adduct of <u>M. luteus</u> catalase with 514.5-nm excitation.	155
Figure 4.	Low frequency RR spectra of <u>M. luteus</u> , <u>A. niger</u> catalases and of ClFe(III)PPIX with excitations of Soret and 457.9 nm respectively.	156
Figure 5.	High frequency spectra of bovine liver catalase and ClFe(III)PPIX.DME with excitations of 457.9 and 488.0 nm.	157
CHAPTER VI.		
Figure 1.	Structure of dimer of 5-(2-hydroxyphenyl)-10,15,20-(tritoyl)Fe(III)porphyrinato complex.	175
Figure 2.	Electronic absorption spectra of (TTOPH)FeCl and [(TTOP)Fe] ₂ in toluene.	176
Figure 3.	High frequency spectra of the monomer and the dimer in a spinning sample holder in 150° backscattering geometry with an excitation of 457.9 nm.	177
Figure 4.	High frequency spectra of the dimer and the monomer with 514.5 nm excitation.	178
Figure 5.	Low frequency spectra of the monomer and the dimer with an excitation of 488.0 nm.	179
Figure 6.	IR spectra of the dimer and monomer as KBr pellets.	180

APPENDIX

Figure 1.	Prosthetic group of cytochromes \underline{c}_1 and \underline{c} .	193
Figure 2.	Resonance Raman spectra of cytochromes \underline{c} and \underline{c}_1 with an excitation of 514.5 nm.	194
Figure 3.	Resonance Raman spectra of cytochromes \underline{c}_1 with and without hinge protein.	195
Figure 4.	Resonance Raman spectra of $\underline{c}_1 + \underline{c}$ with and without hinge protein.	196

ABSTRACT

IDENTIFICATION OF METAL LIGANDS IN AMICYANIN, HEMOCYANIN AND CATALASE BY RESONANCE RAMAN SPECTROSCOPY

Kamala Devi Sharma, Ph.D.

Oregon Graduate Center, 1988

Supervising Professors: Thomas M. Loehr and Joann Sanders-Loehr

Amicyanin is a blue copper protein which functions as a redox mediator in Paracoccus denitrificans. Its resonance Raman (RR) spectrum exhibits intense peaks in the 300-500 cm^{-1} region, suggesting that the copper is ligated to a cysteine thiolate. Most of the RR peaks shift 0.5-1.5 cm^{-1} to lower energy upon equilibration with D_2O , indicating that the cysteine sulfur is hydrogen-bonded to the polypeptide backbone. The high energy of the fundamental RR bands suggest a short Cu-S(Cys) bond distance and their multiplicity implies coupling of Cu-S stretch with internal ligand vibrational modes. These characteristics suggest a distorted trigonal copper site similar to that of azurin and plastocyanin.

Hemocyanin, a binuclear copper protein, exhibits RR peaks at 747 cm^{-1} and 550 cm^{-1} which have been assigned to $\nu(\text{O-O})$ and $\nu(\text{Cu-O}_2)$, respectively, of a coordinated peroxide. Neither peak show

any frequency shift when the protein is equilibrated in D₂O. This implies the absence of hydrogen bond between the peroxide oxygens and the protein. In addition, neither the peroxide-related vibrations at 747 and 550 cm⁻¹ nor the copper-imidazole vibrations at 230, 269, and 313 cm⁻¹ show any sensitivity to solvent ¹⁸O-substitution. This suggest that each of these is a relatively pure vibrational mode and that if a hydroxide bridging ligand is present, its vibrations are not enhanced by excitation within the 345 or 565 nm absorption bands.

Catalase is a heme enzyme responsible for the disproportionation of hydrogen peroxide. The crystal structures of homologous enzymes from bovine liver and Penicillium vitale show tyrosine as an axial ligand to the iron. Resonance Raman spectra of catalase from mammalian, fungal, and bacterial sources were found to be characteristic of a high spin pentacoordinate Fe(III) heme. In addition, new peaks at ~1610 and 1245 cm⁻¹ were observed which are characteristic of tyrosinate ligation. Thus, the tyrosine ligand in mammalian and fungal catalases can be detected by RR spectroscopy and a similar structure is likely for bacterial catalase, as well.

CHAPTER I

METHODS FOR CHARACTERIZING METAL COORDINATION SITES IN PROTEINS

INTRODUCTION

Metalloproteins and enzymes containing transition metals such as copper, iron, manganese, cobalt, nickel and molybdenum are widespread in biological systems and have stimulated active research in many areas of biochemistry. Metal ions modify the structure of proteins by coordinating to specific binding sites in proteins. In biological systems the most commonly found ligands for metal ions are the thiolate group of cysteine, the imidazole group of histidine, the phenolate group of tyrosine, the carboxylate group of aspartic and glutamic acids, the tetrapyrrole macrocycle of porphyrins, and solvent-derived or exchangeable groups such as aquo, hydroxo, oxo, sulfide and peroxide. Various chemical and spectroscopic methods have been employed to study metalloproteins with the ultimate goal of understanding their mechanism of action, function, and structural details and to establish a correlation between them. Techniques including X-ray crystallography, Extended X-ray Absorption Fine Structure (EXAFS), and absorption, NMR, EPR, IR and resonance Raman spectroscopy have been widely used as probes to elucidate the metal binding sites in numerous metalloproteins and metalloenzymes.

Furthermore, chemical preparation of low molecular weight model compounds to mimic the active site structure of metalloproteins has made it possible to correlate structures with the functions and reactivity of metal binding sites.

In this chapter, we will review some of the applications of the above techniques to illustrate how they have been employed to deduce the structural details of the metal binding sites in various metalloproteins.

ABSORPTION SPECTROSCOPY

Proteins exhibit absorption bands due to the aromatic side chains of phenylalanine, tyrosine and tryptophan in the region of 270–290 nm. In addition to these absorption bands, metalloproteins may show extra peaks arising from the $d \rightarrow d$ electronic transitions of the metal and charge transfer (CT) transitions between the metal and the coordinated ligand. The band positions and the intensities depend on the nature of the metal, the ligand and the coordination geometry. The charge-transfer bands are more intense than those due to $d \rightarrow d$ transitions and usually appear in the UV region and sometimes in the visible region. The position of the CT band is diagnostic of the ligand for a constant metal ion. Hence the absorption spectrum provides useful information on the nature and the identity of coordinated ligands when compared with those of model complexes.

Some examples of characteristic metalloprotein absorption spectra are listed in Table I. Cysteinate ligation is indicated by

an intense absorption ($\epsilon \sim 4,500 \text{ M}^{-1} \text{ cm}^{-1}$) at $\sim 600 \text{ nm}$ for Cu(II) in azurin and in Cu(II)-substituted alcohol dehydrogenase and by peaks at ~ 420 and 460 nm ($\epsilon \sim 1,000 \text{ M}^{-1} \text{ cm}^{-1}$) for Fe(III) in ferredoxin. The presence of thiolate ligation from cysteine in amicyanin, a new blue copper protein, was suggested by its sharp absorption band at $\sim 595 \text{ nm}$ ($\epsilon = 4,610 \text{ M}^{-1} \text{ cm}^{-1}$) (see Chapter III). Metal phenolates as in lactoferrin show a characteristic CT band at $450\text{--}550 \text{ nm}$ ($\epsilon \sim 2,000 \text{ M}^{-1} \text{ cm}^{-1}$). Histidine ligands as in azurin make only a weak contribution to the visible absorption spectrum. Of the non-proteinaceous ligands, the most readily identified is the heme group with its $\sim 405 \text{ nm}$ Soret band ($\epsilon \sim 80,000 \text{ M}^{-1} \text{ cm}^{-1}$) as in catalase. Peroxide ligation also contributes significantly to the optical spectra of oxyhemocyanin and oxyhemerythrin. The bridging oxo group appears to be responsible for the intense near-UV transitions in oxyhemerythrin.

X-RAY CRYSTALLOGRAPHY

The use of X-ray crystallography to determine the structures of metalloproteins has made available a wealth of knowledge about their metal binding sites. Deduction of the three-dimensional structure of a protein requires steps such as preparation of good crystals, isomorphous replacements using heavy atoms, measurement of diffraction patterns of isomorphously replaced proteins, deduction of heavy atom positions followed by calculation of phases of reflections and finally obtaining an initial electron density map, accompanied by refinement of the data. In the beginning, low resolution structures

of proteins are obtained which give an overall shape of the molecule which is reconstructed using intensity data near the center of the diffraction pattern. The diffraction pattern near the origin corresponds to the farthest structural features whereas that near the edge corresponds to more detailed structures. The degree of accuracy and resolution attained depends upon the quality of the X-ray data, particularly towards the edges of the diffraction pattern. Some examples of electron-density maps at different resolutions are shown in Figure 1 (8). At 3.0 Å resolution the structural features of the main chain start to resolve, whereas at 2.0 Å the side-chains as well as the carbonyl groups of the peptide backbone are well resolved and the position of the atoms can be located with an accuracy of about ± 0.4 Å. Owing to the nature of the electron density map, its interpretation requires knowledge of the amino acid sequence of the metalloprotein under study. It is generally accepted that the structures do not vary from crystalline to solution state.

The crystal structures of a number of metalloprotein and metalloenzymes have been determined at 2-3 Å resolution. Typical examples are presented in Table II. For ferredoxin and azurin, the crystal structures verified the presence of cysteine ligands which were predicted on the basis of the absorption spectra (Table I). For catalase and myoglobin, the axial ligands which have a negligible effect on the absorption spectrum could be definitively identified. For superoxide dismutase, the observation of only histidine and aspartate ligands explains the faint color of this non-blue copper protein.

X-RAY ABSORPTION SPECTROSCOPY

This spectroscopy is one of the most powerful techniques used to probe the metal centers of metalloproteins and metalloenzymes. It is specific to the metal under study and hence allows the individual metal ion to be probed. It involves the measurement of the absorption of X-radiation by a metal, at and above the absorption edge of the metal, as a function of incident photon energy from a synchrotron source (13). A typical X-ray absorption spectrum has two regions, the X-ray absorption near edge structure (XANES) region and the extended X-ray absorption fine structure (EXAFS) region. The absorption edge region in the small energy range of ~30 eV involves excitation of the core electrons to unoccupied valence shells of the metal. The shape, position and intensities of the electronic transitions provide information about the oxidation state, geometry, and types of the surrounding ligands. The high energy region occurs at 100-1000 eV above the absorption edge. The photoelectron wave propagated from the X-ray absorbing metal atom is backscattered by its neighboring atoms. The resulting interference between the outgoing and back-scattered waves modulates the X-ray absorption of the metal atom. There is an increase or decrease in absorption depending upon whether the scattered wave returns to the origin in phase or out of phase with the outgoing photoelectron wave.

Interpretation of the phase, amplitude and frequency of the EXAFS oscillation can provide information about the type and number of atoms around the metal ion and their respective interatomic distances. Since each element has its own unique value of ionization

energy, one kind of atom in the presence of many others can be studied by tuning to the X-ray energy of the appropriate edge. For instance, the K edge energy for Cu is 8.9 KeV and that for Mo is ~20 KeV. Hence by tuning to the energy of 20 KeV, the Mo atom can be specifically studied in the presence of Cu atom. The interatomic distances of ~ 4 Å to the absorber can be determined to an accuracy of ± 0.02 Å.

EXAFS spectroscopy has been successfully used to establish the ligation of N from imidazole to Cu and to exclude any S ligation to Cu in hemocyanin from mollusc and arthropods (14). In order to get optimum results for the second shell atoms, a group fitting procedure is used; e.g., in the case of imidazole ligands, the EXAFS of the rigid multiatom ligand is fitted as a whole (15). Further, EXAFS studies on rubredoxin from Clostridium pasteurianum (16, 17) and from Peptococcus aerogenes (18) showed that all four Fe-S(Cys) bonds are equivalent, i.e., 2.26 ± 0.05 Å. Later the X-ray structure was refined (8) to get a value in agreement with EXAFS data. EXAFS studies were also carried out on oxidized and reduced superoxide dismutase (bovine erythrocyte) giving evidence that Cu(I) in reduced SOD has three coordinated nitrogen atoms from imidazoles (average Cu-N distance = 1.9 Å), but the oxidized form has four coordinated N(Im) (Cu-N = 1.99 Å) plus one oxygen atom from water at 2.24 Å (19).

The Mo environment of Mo-Fe protein of Clostridium pasteurianum nitrogenase and of Azotobacter vinelandii has been characterized by EXAFS (20). Detailed analysis of XANES and EXAFS provided the first

direct evidence of Mo being primarily coordinated to S and the existence of an Mo-Fe-S cluster.

Representative Cu EXAFS spectra of oxidized and reduced plastocyanin are shown in Figure 2. The marked shift in the phase and the amplitude of the spectrum between the Cu(I) and Cu(II) states indicates that some changes in copper-ligand bond distances have occurred. Two shell fits to Fourier filtered peaks of the plastocyanin EXAFS are shown in Table III. The EXAFS values are in good agreement with those determined by X-ray crystallography. Both techniques show an ~ 0.1 Å increase in copper-ligand bond distances upon reduction. The contributions of the two histidine ligands are averaged in the EXAFS calculations, and the Cu-methionine bond is too weak to be observed by EXAFS. Thus, it can be seen that EXAFS gives direct information about the nature, number and geometry of ligands along with the redox state of the metal ion, as well as the distance between the metal and the ligands or other metals.

NUCLEAR MAGNETIC RESONANCE SPECTROSCOPY

Magnetic resonance spectroscopy has become a powerful technique in a wide variety of biochemical studies. It is comprised of nuclear magnetic resonance and electron spin resonance both of which are founded on the same principle that the spin of an atomic nucleus or an electron is reoriented in the presence of an applied magnetic field. Nuclear magnetic resonance (NMR) has been extensively applied to characterize the metal center in numerous proteins such as

ferredoxin and rubredoxin (22), plastocyanin (23), cytochrome *c* peroxidase (24), uteroferrin (25), and ribonucleotide reductase (26). Because of good sensitivity for detection and high abundance in biological systems, protons are the most commonly studied nuclei in NMR spectroscopy. For greater selectivity ^{13}C or ^{19}F is sometimes inserted to act as a structural probe for a particular metal site. The presence of a paramagnetic metal center can cause significant changes in the chemical shifts of nearby residues, particularly ligating amino acids. Such contact-shifted resonances are generally well separated from other protein resonances and, thus, easy to identify.

The coordination chemistry of the active site iron in catechol dioxygenase was elucidated using NMR spectroscopy (27). The paramagnetically shifted resonances at 50–80 ppm and 20–40 ppm were assigned to the $\beta\text{-CH}_2$ protons of ligated tyrosine and histidines, respectively. The presence of these ligands was found to be consistent with Raman and EXAFS data. Proton NMR studies of plastocyanins (23) showed that two histidines residues are ligated directly to copper.

Uteroferrin, a binuclear non-heme iron protein, was also studied by ^1H NMR to elucidate the coordination chemistry of the Fe(III) and Fe(II) sites. It was found that tyrosine was ligated only to the ferric site whereas N–H resonances near 89 ppm and 44 ppm in pink uteroferrin corresponded to histidine ligation to both ferrous and ferric sites, respectively (25). The histidine N–H resonances were specifically identified by their decrease in intensity in D_2O (Fig.

3). Similarly, histidine ligation to iron was suggested by ^1H NMR studies of ribonucleotide reductase (26). Hence, NMR spectroscopy is particularly useful for identifying histidine, tyrosine, and cysteine ligands in paramagnetic metalloproteins.

ELECTRON PARAMAGNETIC RESONANCE SPECTROSCOPY

Electron paramagnetic resonance (EPR) spectroscopy measures the interaction of the electron magnetic moment with an applied magnetic field. It detects paramagnetic centers due to unpaired electrons. The reorientation of the electron spin in a strong magnetic field causes the absorption of incident microwave radiation. EPR measurement of metalloproteins tells us about the oxidation and spin state of the metal, and aids in the characterization of the ligands through the examination of ligand hyperfine splitting (28). There are four important parameters in an EPR spectrum: a) the g-value characteristic of the position of a resonance which measures the local magnetic field experienced by the electron, b) the intensity, which is proportional to the concentration of the unpaired electron spins giving rise to the spectrum, c) the linewidth, and d) the multiplet structure or splitting due to the interactions of the unpaired electron with its own and other nuclei. In cases where the metal studied does not have an unpaired electron, a 'spin-labeling' technique using a stable free radical such as nitroxide which binds to a metal site can be employed. It gives information on the spin state of the metal, geometry at the metal ion center, and the identity of neighboring nuclei (particularly nitrogen).

EPR spectroscopy has been applied extensively to the study of metalloproteins (Table IV). It has been used to elucidate the symmetry of the Cu(II) site in blue copper proteins, such as azurins and plastocyanins. Their spectra show an abnormally small copper hyperfine splitting (1) which is not consistent with the square planar coordination typically observed for Cu(II) complexes. On the basis of ligand-field analysis, the blue copper proteins were suggested to have metal binding sites with a geometry closer to tetrahedral (29). The EPR spectrum of plastocyanin has been well explained using a theoretical analysis based on lowered symmetry to C_s or C_1 (30).

Related measurements on blue copper proteins using electron nuclear double resonance (ENDOR) spectroscopy showed resonances due to strongly coupled methylene protons of a coordinated cysteinyl S^- as well as due to nitrogenous ligands (31). The change in the ligand hyperfine couplings of the blue copper sites in laccase compared to those of azurin, plastocyanin, and stellacyanin indicated a somewhat different coordination geometry in laccase. In addition to ENDOR, the electron spin echo method was applied to measure superhyperfine splittings due to coordinated imidazole nitrogens in stellacyanin (32).

Electron paramagnetic resonance studies on heme proteins have provided useful information about the identity of the axial ligands, the spin state of oxidized heme iron, and the symmetry of the heme iron site (33, 34). Heme proteins which occur naturally as high spin Fe(III) (e.g., catalase) typically have axial EPR spectra with the

principal g value near 6.0, while those with low-spin Fe(III) (e.g., cytochrome c) have their principal g value near 2.0 (Table IV). The spectrum of the fluoride complex of catalase (Fig. 4A) is typical of a high-spin Fe(III) in a rhombic environment. Broadening or splitting of the absorption line at $g = 6$ shows departure of symmetry from axial to rhombic. The appearance of new features at $g = 2.8$, 2.18, and 1.74 on coordination of azide in place of fluoride is indicative of the conversion of some of the Fe(III) to the $S = 1/2$ low spin state. The presence of N(imidazole) as an axial ligand to the heme group has been demonstrated for ferrous horseradish peroxidase (34a) and manganese peroxidase (34b) through the use of an NO spin label (Fig. 5). The nitrogen hyperfine interactions of ^{14}N ($I = 1$) or ^{15}N ($I = 1/2$) from the NO ligand alone result in the splitting of the free radical EPR signal into a triplet or a doublet, respectively. These signals show an additional narrower triplet splitting due to a trans-axial ^{14}N , presumably from an imidazole.

The symmetry and the oxidation states of iron in iron-sulfur proteins have also been determined using EPR measurements (35). Rubredoxin (oxidized) showed EPR signal characteristic of ferric high spin rhombic, with g values of 4.3 and ~ 9 at low temperature. Similarly the g values of reduced spinach ferredoxin showed that the environment of the metal ion has low symmetry. Both of these findings are consistent with the tetrahedral iron coordination geometry which is characteristic of iron-sulfur proteins.

RESONANCE RAMAN SPECTROSCOPY

Vibrational spectroscopy such as infrared (IR) and Raman provides information about the interatomic vibrations of a molecule (36). Although IR and Raman spectroscopy provide similar kinds of information, they differ in their origins. Infrared spectroscopy is an absorption process that requires a change in the dipole moment of the molecule during the vibration. On the other hand, Raman spectroscopy is a scattering phenomenon which demands a change in the polarizability of the molecule for activity. Both IR and Raman spectra show similar frequencies when the molecules studied possess little or no symmetry. However, the rule of mutual exclusion applies to molecules with a center of symmetry. According to this principle, for molecules with a center of symmetry, the vibrational transitions that are allowed in the Raman are forbidden in the IR and vice versa. The vibrations that are antisymmetric with respect to the center of symmetry are IR active whereas the ones that are symmetric are Raman active. Both techniques are used to study all phases of matter, however Raman spectroscopy is more useful for studying biomolecules since water absorbs strongly in IR, but its Raman scattering is minimal.

When incident light of frequency ν_0 collides with a molecule and is scattered elastically with no change in frequency, the process is known as Rayleigh scattering. However, when the incident light undergoes a change in frequency due to transfer of energy to or from a given vibrational state of the molecule, then it is Raman scattering. In cases where the energy of the incident radiation

falls within certain electronic absorption bands of the sample, vibrational transitions which are coupled to such electronic transitions may have enhanced intensities. This is known as the resonance Raman (RR) effect. Resonance Raman spectroscopy has become a highly selective and sensitive probe for exploring biological chromophores such as transition metal ions and heme groups in proteins. The electronic transitions which most readily give rise to resonance enhancement are ligand to metal charge transfer transitions in non-heme metalloproteins and porphyrin $\pi \rightarrow \pi^*$ transitions in heme proteins. The resonance Raman technique makes it possible to observe vibrations localized in the chromophore without interference from the rest of the protein molecule.

Heme Proteins. Heme containing proteins have three characteristic absorption bands: the Soret band ($\lambda_{\text{max}} \sim 400 \text{ nm}$, $\epsilon = 100,000 \text{ M}^{-1} \text{ cm}^{-1}$) and the lower energy α and β bands around 500–600 nm ($\epsilon = 10,000 \text{ M}^{-1} \text{ cm}^{-1}$). Excitation into the Soret and Q (α and β) region gives enhancement of peaks due to totally symmetric and asymmetric modes of the porphyrin moiety. In heme proteins the vibrational modes in the region of 1300–1700 cm^{-1} are indicative of the chemical environment around the central iron atom e.g., its oxidation and spin states (for details see catalase and cytochrome c chapters of this thesis). Some of the vibrational frequencies for heme iron with varying oxidation and spin states are shown in the Table V. The band assigned as ν_4 is particularly sensitive to the oxidation state of the iron, while ν_3 and ν_{19} are indicators of the spin state.

In heme proteins, the iron is always bound to the four pyrrole nitrogens of the porphyrin moiety and usually to one or more endogenous axial ligands. The most common axial ligands being N(Im) (in horseradish peroxidase, hemoglobin and myoglobin), $O^-(Tyr)$ (in catalase), and $S^-(Cys)$ (in cytochrome P-450 monooxygenase). The Fe-axial ligand vibrational modes occur in the low frequency region below 700 cm^{-1} .

For deoxyhemoglobin a band at $\sim 220\text{ cm}^{-1}$ has been assigned as $\nu[Fe-N(Im)]$ (37-41) based on comparative studies with model complexes. Further RR studies on ^{57}Fe and ^{15}N isotopically substituted myoglobin confirmed the assignment of this peak as $\nu[Fe-N(Im)]$ (42). Since oxyhemoglobin has its iron bonded to O_2 , RR studies showed the $\nu(Fe-O_2)$ to be around 567 cm^{-1} and this was confirmed by $^{18}O_2$ substitution (43).

One of the most interesting axial ligands is the cysteinyl thiolate ligand in cytochrome P-450. The presence of the thiolate ligand in the RR spectrum of cytochrome P-450 is even felt by its oxidation-state marker band at 1346 cm^{-1} which is lower than those of other Fe(II) heme proteins (44). This has been explained as being due to the π -donor character of the thiolate ligand. The $\nu[Fe-S(Cys)]$ was observed at 351 cm^{-1} and was assigned as such on the basis of its upshift of 2.5 and 4.9 cm^{-1} with ^{56}Fe and ^{34}S substitution, respectively (44). This frequency is comparable to the values of $333\text{--}345\text{ cm}^{-1}$ observed for $\nu(Fe-S)$ in the IR spectra of model heme thiolate complexes (45).

Type c cytochromes are heme proteins which play an important role in the mitochondrial electron transport chain. Recently, it was found that cytochrome c and c₁ form a complex in the presence of an essential mitochondrial protein called the "hinge protein". To address the effect of hinge protein on the structures of cytochromes c and c₁ and to investigate possible structure-function correlations, Raman studies were carried out on cytochromes c and c₁ with and without the hinge protein (see Appendix for details). The characteristic porphyrin marker bands ν_4 , ν_3 , ν_{10} , and ν_{19} indicate that both cytochromes have low-spin iron configurations. In isolation, cytochrome c has ferric iron whereas c₁ has ferrous iron. However, the Raman spectra of their mixture show the spectral features ν_{10} at 1625 cm^{-1} , ν_{19} at 1585 cm^{-1} , ν_{11} at 1545 cm^{-1} , ν_3 at 1494 cm^{-1} , and ν_4 at 1360 cm^{-1} that are characteristic of low-spin ferrous iron. This observation can be explained as a consequence of reduction of c by c₁ followed by photoreduction of oxidized c₁ on laser illumination. The redox processes are consistent with their respective redox potentials. No effect of hinge protein on the vibrational modes of the cytochromes is observed which implies that the protein-protein interactions are not transmitted to the heme chromophores and that Raman spectroscopy is, therefore, insensitive to the protein complex formation.

Iron Tyrosinate Proteins. Resonance Raman spectroscopy has been successful in identifying the presence of tyrosine ligands in iron containing proteins such as purple acid phosphatases (46-49), catechol dioxygenases (50-54), transferrins (55-58), mutant

hemoglobins (59), and their model complexes (60a). When excited into the Fe-O(Tyr) charge transfer region (~500 nm), these proteins exhibit four phenolate vibrational modes at approximately 1600, 1500, 1270 and 1170 cm^{-1} (Fig. 6). These resonance enhanced peaks are the characteristic fingerprints of iron tyrosinate proteins (60b). On the basis of the normal coordinate analysis of model complexes (55), the peaks at 1600 and 1500 cm^{-1} are assigned as phenolate $\nu(\text{C-C})$ and those at 1270 and 1170 cm^{-1} are assigned as phenolate $\nu(\text{C-O})$ and $\delta(\text{C-H})$, respectively. In the low frequency region a feature at ~570 cm^{-1} has also been observed for model complexes and has been assigned as a combination of ν_{12} (benzene ring) with $\nu(\text{Fe-O})(\text{phenolate})$ (60a). A similar peak at ~570 cm^{-1} has been observed for pink and purple uteroferrin as well as for purple acid phosphatase and has been assigned as having a partial $\nu(\text{Fe-O})$ character (46).

Binuclear Iron Proteins. Non-heme μ -oxo bridged iron proteins such as hemerythrin and ribonucleotide reductase are also amenable to study by RR spectroscopy (61a). For oxyhemerythrin, the symmetric stretch, $\nu_s(\text{Fe-O-Fe})$, the asymmetric stretch, $\nu_{as}(\text{Fe-O-Fe})$, $\nu(\text{O-O})$ and $\nu(\text{Fe-O}_2)$ have been observed at 486, 753, 844 and 503 cm^{-1} , respectively (61b). These features have been assigned based on shifts accompanying ^{18}O substitution from solvent oxygen or gaseous O_2 and by comparison with the behavior of model complexes. The $\nu_s(\text{Fe-O-Fe})$ and $\nu_{as}(\text{Fe-O-Fe})$ for ribonucleotide reductase were observed at 492 and 756 cm^{-1} , respectively (62). When oxyhemerythrin and ribonucleotide reductase were equilibrated with D_2O , both of

their $\nu_s(\text{Fe-O-Fe})$ peaks underwent a shift of $3\text{-}4\text{ cm}^{-1}$ to higher energy which is probably due to hydrogen-bonding interactions of the Fe-O-Fe moiety (61, 62).

Iron-Sulfur Proteins. Iron sulfur proteins include mononuclear Fe-4S(Cys), binuclear 2Fe-2S-4S(Cys), and tetranuclear 4Fe-4S-4S(Cys) clusters. They show strong absorptions in the visible and near UV regions due to $\text{S}^{2-} \rightarrow \text{Fe}$ charge transfer transitions. This property has been exploited to obtain RR spectra of rubredoxin (mononuclear), ferredoxins (binuclear and tetranuclear), adrenodoxin (binuclear), and high potential iron proteins (tetranuclear) (63). Oxidized rubredoxin, for example, showed four RR peaks at 312, 325, 359 and 371 cm^{-1} which were assigned as $\nu[\text{Fe-S(Cys)}]$ by comparison to model complexes (63). In binuclear and tetranuclear iron sulfur proteins, vibrational modes due to Fe-S (bridging ligands) and Fe-S(Cys) (terminal ligands) can be distinguished by the isotope shifts of the former upon substitution with ^{34}S -labelled sulfide. A representative spectrum of a binuclear iron-sulfur protein, spinach ferredoxin, is shown in Figure 7. This spectrum is readily distinguished from that of the tetranuclear clusters where the most intense spectral feature due to the totally symmetric stretch of the bridging sulfides occurs near 340 cm^{-1} (63).

As seen from their crystal structures, the sulfur ligands in the iron-sulfur proteins are found to be extensively H-bonded to the NH groups in the polypeptide backbone. This was confirmed by observation of deuterium dependent shifts in the RR spectra of binuclear ferredoxins and adrenodoxin (64). A deuterium shift of

0.3–2.0 cm^{-1} was observed for vibrations of the terminal as well as the bridging iron–sulfur groups.

Blue Copper Proteins. The x-ray crystal structures of plastocyanin (21b) and azurin (11) have shown that Cu(II) is found in a distorted tetrahedral or trigonal bipyramidal environment being coordinated to two histidines and one cysteine ligand. On excitation into the intense 600 nm absorption band, four to five resonance enhanced vibrational modes are seen between 350 and 420 cm^{-1} (65). Assignment of the peaks has been complicated because they do not represent pure vibrational modes but are due to coupling between $\nu(\text{Cu-S})$ and internal stretches of histidine and cysteine ligands. Deuterium substitution also showed shifts in the spectral region of 350–450 cm^{-1} which can be attributed to the hydrogen bonding of the ligands (particularly Cys) with the polypeptide backbone (64). Representative spectra are shown in Chapter III on amicyanin.

Binuclear Copper Proteins. The detailed nature of the binding site of an antiferromagnetically coupled binuclear Cu center is not yet clear. Along with other techniques such as X-ray crystallography and EXAFS, RR spectroscopy has been able to shed some light on the structural details of hemocyanin and tyrosinase. Based on the $^{18}\text{O}_2$ dependent isotopic shift of the peak at 750 cm^{-1} , the oxygen in oxyhemocyanin was shown to be bound as a peroxide ion in a $\mu-1,2$ fashion (2a). Another peak at 550 cm^{-1} was assigned as $\nu(\text{Cu-O}_2)$ on the basis of its loss of intensity with $^{18}\text{O}_2$ (66). Excitation of oxyhemocyanin within the near-UV absorption at 345 nm produces peaks in the region of 150–350 cm^{-1} . Based on shifts due to D_2O and ^{65}Cu

isotopic substitution, the peaks at 230, 269, and 313 cm^{-1} have been assigned to Cu(II)-N(His) vibrational modes (2c). In order to explore the nature of the bridging group and to investigate the possibility of H-bonding of the bound peroxide, we studied the RR spectrum of oxyhemocyanin in D_2O and H_2^{18}O . Results are presented in Chapter IV. No isotopic shifts of $\nu(\text{O}-\text{O}^{2-})$ at 750 cm^{-1} or $\nu(\text{Cu}-\text{O}_2)$ at 550 cm^{-1} were observed indicating that both of these vibrational modes are pure, uncoupled vibrational modes. Similarly, the lack of any shifts of the peaks at 230, 269 and 313 cm^{-1} implies that these are probably pure $\nu[\text{Cu}-\text{N}(\text{His})]$ in nature.

In conclusion, the usefulness of RR spectroscopy in the elucidation of the coordination and the structural details at the metal binding sites in various metalloproteins cannot be denied. In order to understand fully the roles of transition metal ions in metalloproteins and to characterize their structural details, X-ray crystallography, EXAFS, NMR, absorption spectroscopy, IR and RR spectroscopy act as complementary techniques. It is also necessary to understand the individual advantages and disadvantages of each of these techniques and, as in building a jig-saw puzzle, to appreciate the contributions of each piece to the emerging whole.

REFERENCES

1. Ainscough, E. W., Bingham, A. G., Brodie, A. M., Ellis, W. R., Gray, H. B., Loehr, T. M., Plowman, J. E., Norris, G. E., and Baker, E. N. (1987) Biochemistry 26, 71
2. (a) Freedman, T. B., Sanders-Loehr, J., and Loehr, T. M. (1976) J. Am. Chem. Soc. 98, 2809
(b) Eickman, N. C., Himmelwright, R. S., and Solomon, E. I. (1979) Proc. Natl. Acad. Sci. U.S.A. 76, 2094
(c) Larrabee, J. A., and Spiro, T. G. (1980) J. Am. Chem. Soc. 102, 4217
3. Meyer, J., Moulis, J.-M., and Lutz, M. (1986) Biochim. Biophys. Acta 871, 243
4. Aisen, P., and Leibman, A. (1972) Biochim. Biophys. Acta 257, 314
5. Samejima, T., and Yang, J. T. (1963) J. Biol. Chem. 238, 3256
6. (a) Garbett, K., Darnall, D. W., Klotz, I. M., and Williams, R. J. P. (1969) Arch. Biochem. Biophys. 135, 419
(b) Dunn, J. B. R., Addison, A. W., Bruce, R. E., Sanders-Loehr, J., and Loehr, T. M. (1977) Biochemistry 16, 1743
7. Maret, W., Shiemke, A. K., Wheeler, W. D., Loehr, T. M., and Sanders-Loehr, J. (1986) J. Am. Chem. Soc. 108, 6351
8. (a) Watenpaugh, K. D., Sieker, L. C., Herriott, J. R., and Jensen, L. H. (1973) Acta Cryst. B29, 943
(b) Watenpaugh, K. D., Sieker, L. C., and Jensen, L. H. (1980) J. Mol. Biol. 138, 615

9. (a) Richardson, J. S. M., Thomas, K. A., Rubin, B. H., and Richardson, D. C. (1975) Proc. Natl. Acad. Sci. U.S.A. **72**, 1349
(b) Tainer, J. A., Getzoff, E.D., Beem, K. M., Richardson, J. S., and Richardson, D. C. (1982) J. Mol. Biol. **160**, 181
10. (a) Tsukihara, T., Fukuyama, K., Nakamura, M., Katsube, Y., Tanaka, N., Kakudo, M., Wada, K., Hase, T., and Matsubara, H. (1981) J. Biochem. (Tokyo) **90**, 1763
(b) Vainshtein, B. K., Melik-Adamyanyan, W. R., Barynin, V. V., Vagin, A. A., Grebenko, A. I., Borisov, V. V., Bartels, K. S., Fita, I., and Rossmann, M. G. (1986) J. Mol. Biol. **188**, 49
11. (a) Norris, G. E., Anderson, B. F., and Baker, E. N. (1983) J. Mol. Biol. **165**, 501; (b) Ibid (1986) J. Am. Chem. Soc. **108**, 2784
12. Kendrew, J. C., Dickerson, R. E., Strandberg, B. E., Hart, R. G., Davies, D. R., Phillips, D. C., and Shore, V. C. (1960) Nature **185**, 422
13. Co, M. S., and Hodgson, K. O. (1984) in Copper Proteins and Copper Enzymes (Lontie, R., Ed.) CRC Press, Boca Raton, pp. 93-113
14. (a) Brown, J. M., Powers, L., Kincaid, B., Larrabee, J. A., and Spiro, T. G. (1980) J. Am. Chem. Soc. **102**, 4210
(b) Woolery, G. L., Powers, L., Winkler, M., Solomon, E. I., and Spiro, T. G. (1984) J. Am. Chem. Soc. **106**, 86
15. Co, M. S., Scott, R. A., and Hodgson, K. O. (1981) J. Am. Chem. Soc. **103**, 986

16. Sayers, D. E., Stern, E. A., and Herriott, J. R. (1976)
J. Chem. Phys. 64, 427
17. Bunker, B., and Stern, E. (1977) Biophys. J. 19, 253
18. Shulman, R. G., Eisenberger, P., Teo, B. K., Kincaid, B. M., and
Brown G. S. (1978) J. Mol. Biol. 124, 305
19. Blackburn, N. J., Hasnain, S. S., Binsted, N., Diakum, G. P.,
Garner, C. D., and Knowles, P. F. (1984) Biochem. J. 219, 985
20. (a) Cramer, S. P., Hodgson, K. O., Gillum, W. O., and Mortenson,
L. E. (1978) J. Am. Chem. Soc. 100, 3398
(b) Conradson, S. D., Burgess, B. K., Newton, W. E.,
Mortenson, L. E., and Hodgson, K. O. (1987) J. Am. Chem.
Soc. 109, 7507
21. a) Freeman, H. C. (1981) in Coordination Chemistry (Laurent, J.
P., ed.) Pergamon, New York, pp. 29-51
(b) Guss, J. M., and Freeman, H. C. (1983) J. Mol. Biol. 169,
521
22. a) Phillips, W. D., and Poe, M. (1973) in Iron-Sulfur Proteins
(Lovenberg, W., ed.), Academic Press, N.Y., Vol.2, pp 255-
284; b) Palmer, G. in Ibid, pp 285-325
23. Markley, J. L., Ulrich, E. L., Berg, S. P., and Krogmann, D. W.
(1975) Biochemistry 14, 4428
24. Satterlee, J. D., Erman, J. E., La Mar, G. N., Smith, K. M., and
Langry, K. C. (1983) J. Am. Chem. Soc. 105, 2099
25. Lauffer, R. B., Antanaitis, B. C., Aisen, P., and Que, L. Jr.
(1983) J. Biol. Chem. 258, 14212

26. Sahlin, M., Ehrenberg, A., Gråslund, A., and Sjöberg, B. M.
(1986) J. Biol. Chem. 261, 2778
27. Que, L., Jr., Lauffer, R. B., Murch, B. P., and Pyrz, J. W.
(1987) J. Am. Chem. Soc. 109, 5381
28. Palmer, G. (1980) in Advances in Inorganic Biochemistry
(Darnell, D. W., and Wilkins, R. G., eds.) Elsevier Press,
N.Y., Vol.2, pp 153-182
29. (a) Solomon, E. I., Hare, J. W., and Gray, H. B. (1976) Proc.
Natl. Acad. Sci. U.S.A. 73, 1389; b) Solomon, E.I., Hare, J.
W., Dooley, D. M., Dawson, J. H., Stephens, P. J., and
Gray, H. B. (1980) J. Am. Chem. Soc. 102, 168
30. Penfield, K. W., Gewirth, A. A., and Solomon, E. I. (1985)
J. Am. Chem. Soc. 107, 4519
31. Roberts, J. E., Cline, J. F., Lum, V., Freeman, H., Gray, H. B.,
Peisach, J., Reinhammar, B., and Hoffman, B. M. (1984) J. Am.
Chem. Soc. 106, 5324
32. (a) Mims, W. B., and Peisach, J. (1979) J. Biol. Chem. 254,
4321; (b) Ibid (1976) Biochemistry 15, 3863
33. (a) Palmer G. (1979) in The Porphyrins (Dolphin. D., ed.)
Academic Press, N.Y., Vol.4, pp 313-353
(b) Torii, K., and Ogura, Y. (1968) J. Biochem. (Tokyo) 64, 171
34. (a) Yonetani, T., Yamamoto, H., Erman, J. E., Leigh, J. S., Jr.,
and Reed, G. H. (1972) J. Biol. Chem. 247 , 2247
(b) Mino, Y., Wariishi, H., Blackburn, N. J., Loehr, T. M.,
and Gold, M. H. (1988) J. Biol. Chem. 263, 7029

35. Orme-Johnson (1973) in Iron-Sulfur Proteins (Lovenberg, W., Ed.) Academic Press N.Y., Vol. 2, pp 195-238
36. Nakamoto, K. (1986) in Infrared and Raman Spectra of Inorganic and Coordination Compounds, 4th ed., Wiley-Interscience, New York
37. Nagai, K., Kitagawa, T., and Morimoto, H. (1980) J. Mol. Biol. **136**, 271
38. Kincaid, J., Stein, P., and Spiro, T. G. (1979) Proc. Natl. Acad. Sci. U.S.A. **76**, 549
39. Kitagawa, T., Nagai, K., and Tsubaki, M. (1979) FEBS Letters **104**, 376
40. Hori, H., and Kitagawa, T. (1980) J. Am. Chem. Soc. **102**, 3608
41. Teroaka, J., and Kitagawa, T. (1980) Biochem. Biophys. Res. Commun **93**, 694
42. Argade, P. V., Sassaroli, M., Rousseau, D. L., Inubushi, T., Ikeda-Saito, M., and Lapidor, A. (1984) J. Am. Chem. Soc. **106**, 6593
43. Brunner, H. (1974) Naturwissenschaften **61**, 129
44. Champion, P. M., Stallard, B. R., Wagner, G. C., and Gunsalus, I. C. (1982) J. Am. Chem. Soc. **104**, 5469
45. Oshio, H., Ama, T., Watanabe, T., and Nakamoto, K. (1985) Inorg. Chim. Acta. **96**, 61
46. Averill, B. A., Davis, J. C., Burman, S., Zirino, T., Sanders-Loehr, J., Loehr, T. M., Sage, T., and Debrunner, P. G. (1987) J. Am. Chem. Soc. **109**, 3760

47. Gaber, B. P., Sheridan, J. P., Bazer, F. W., and Roberts, R. M. (1979) J. Biol. Chem. 254, 8340
48. Davis, J. C., and Averill, B. A. (1982) Proc. Natl. Acad. Sci. U.S.A. 79, 4623
49. Antanaitis, B. C., Strekas, T., and Aisen, P. (1982) J. Biol. Chem. 257, 3766
50. Bull, C., Ballou, D. P., and Salmeen, I. (1979) Biochem. Biophys. Res. Commun. 87, 836
51. Tatsuno, Y., Saeki, Y., Iwaki, M., Yagi, T., Nozaki, M., Kitagawa, T., and Otsuka, S. (1978) J. Am. Chem. Soc. 100, 4614
52. Que, L., Jr., and Heistand, R. H. II (1979) J. Am. Chem. Soc. 101, 2219
53. Keyes, W. E., Loehr, T. M., and Taylor, M. L. (1978) Biochem. Biophys. Res. Commun. 83, 941
54. Felton, R. H., Chung, L. D., Phillips, R. S., and May, S. W. (1978) Biochem. Biophys. Res. Commun. 85, 844
55. Tomimatsu, Y., Kint, S., and Scherer, J. R. (1976) Biochemistry 15, 4918
56. Carey, P. R., and Young, N. M. (1974) Biochemistry 52, 273
57. Ainscough, E. W., Brodie, A. M., Plowman, J. E., Bloor, S. J., Sanders-Loehr, J., and Loehr, T. M. (1980) Biochemistry 19, 4072
58. Gaber, B. P., Miskowski, V., and Spiro, T. G. (1974) J. Am. Chem. Soc. 96, 6868

59. Nagai, K., Kagimoto, T., Hayashi, A., Taketa, F., and Kitagawa, T. (1983) Biochemistry 22, 1305
60. (a) Pyrz, J. W., Roe, L. A., Stern, L. J., and Que, L., Jr. (1985) J. Am. Chem. Soc. 107, 614
(b) Que, L., Jr. (1988) in Biological Applications of Raman Spectroscopy (Spiro, T. G., ed., Wiley) Vol. 3, pp 491-522
61. (a) Loehr, T. M., and Shiemke, A. K. (1988) in Biological Applications of Raman Spectroscopy (Spiro, T. G., ed., Wiley) Vol. 3, pp 439-490
(b) Shiemke, A. K., Loehr, T. M., and Sanders-Loehr, J. (1986) J. Am. Chem. Soc. 108, 2437
62. Sjöberg, B.-M., Sanders-Loehr, J., and Loehr, T. M. (1987) Biochemistry 26, 4242
63. Spiro, T. G., and Li, X.-Y. (1988) in Biological Applications of Raman Spectroscopy (Spiro, T. G., ed., Wiley) Vol. 3, pp. 1-38
64. Mino, Y., Loehr, T. M., Wada, K., Matsubara, H., and Sanders-Loehr, J. (1987) Biochemistry 26, 8059
65. Woodruff, W. H., Dyer, R. B., and Schoonover, J. R. (1988) in Biological Applications of Raman Spectroscopy (Spiro, T. G., ed., Wiley) Vol. 3, pp. 413-438
66. Nestor, L. M., and Spiro, T. G., personal communication.

TABLE I
Electronic Absorption Spectra of Metalloproteins

Proteins	λ_{\max} [ϵ] ^a	Assignment ^b
Azurin	~1,000 [n.r.]	d → d
	780 [1,040]	S(Cys) π → Cu($d_{x^2-d_y^2}$) CT
	619 [5,100]	S(Cys) σ → Cu($d_{x^2-d_y^2}$) CT
	460 [580]	N(His) π → Cu($d_{x^2-d_y^2}$) CT
Hemocyanin	570 [1,000]	O ₂ ²⁻ → Cu(II) CT
	345 [10,000]	O ₂ ²⁻ → Cu(II) CT
Ferredoxin	422 [950]	S(Cys) & S ²⁻ → Fe(III) CT
	464 [880]	S(Cys) & S ²⁻ → Fe(III) CT
Lactoferrin	~465 [2,070]	O (Tyr) → Fe(III) CT
Catalase	405 [324,000]	π → π^* (porphyrin ring)
Hemerythrin	330 [3,500]	O(oxo) → Fe(III) CT
	360 [2,700]	O(oxo) → Fe(III) CT
	500 [1,200]	O ₂ ²⁻ → Fe(III) CT
Cu(II)-LADH	620 [4,000]	S ⁻ (Cys) → Cu(II) CT

^a λ_{\max} in nm, ϵ in M⁻¹ cm⁻¹ per metal ion, n.r. = not resolved.

^bAzurin (1), hemocyanin (2), spinach ferredoxin (ϵ per 4 S) (3), lactoferrin (ϵ per 2 tyrosines) (4), catalase (ϵ per 4 hemes) (5), hemerythrin (6), LADH, liver alcohol dehydrogenase (7).

TABLE II
Metal-Binding Sites Identified by X-ray Crystallography^a

Metalloprotein	Metal ions	Ligating residues
Superoxide dismutase	Zn	His 61, His 69, His 78, Asp 81
	Cu	His 44, His 46, His 61, His 118
Ferredoxin	Fe _A	Cys 41, Cys 46
	Fe _B	Cys 49, Cys 79
Catalase	Fe	Tyr 345, and porphyrin
Azurin	Cu	His 46, Cys 112, His 117
Oxymyoglobin	Fe	F8 His, porphyrin, O ₂

^aBovine superoxide dismutase (9), ferredoxin from Spirulina platensis (10a), catalase from Penicillium vitale (10b), azurin from Alcaligenes denitrificans (11), sperm whale myoglobin (12).

TABLE III
Comparison of Plastocyanin Copper-ligand Distances
Obtained by X-ray Crystallography and EXAFS

Sample	X-ray Crystallography ^a		EXAFS ^b	
	R in Å		R in Å (N)	
Oxidized				
Cu-N(His)	2.04	}	1.97	(2.3)
Cu-N(His)	2.10			
Cu-S(Cys)	2.13		2.11	(1.1)
Cu-S(Met)	2.90			
Reduced				
Cu-N(His)	2.3	}	2.05	(2.2)
Cu-N(His)	2.1			
Cu-S(Cys)	2.2		2.22	(0.8)
Cu-S(Met)	2.9			

^aValues from reference 21. ^bValues for two-shell fit to Fourier-filtered peaks from reference 13. N = number of ligands.

TABLE IV

EPR Properties of Metal Ions Found in Biochemical Systems^a

Metal Ion	Electronic Configuration	Spin-State		g-Values	Nuclear Spin
Fe ³⁺	3d ⁵	1/2	Cytochrome	3.8-0.5	0
Fe ³⁺	3d ⁵	5/2	Hemoproteins	8-1.8	0
Fe ³⁺	3d ⁵	5/2	Non-heme Iron	10-0.5	0
Fe ³⁺ , Fe ²⁺ pair	3d ⁵ , 3d ⁶	1/2	Spinach Ferredoxin	1.7-2.1	0
3Fe ³⁺ , Fe ²⁺ tetrad	(3d ⁵), 3d ⁶	1/2	HiPIP	2-2.2	0
Fe ³⁺ , 3Fe ²⁺ tetrad	3d ⁵ (3d ⁶)	1/2	Bacterial Ferredoxin	1.7-2.1	0
Mn ²⁺	3d ⁵	5/2	Concanavalin A	2-6	5/2
Co ²⁺	3d ⁷	1/2	Cobalamin (B ₁₂ r)	2.0-2.3	7/2
Co ²⁺	3d ⁷	3/2	Cobalt-substituted Proteins	1.8-6	7/2
Cu ²⁺	3d ⁹	1/2	Plastocyanin	2-2.4	3/2
Mo ⁵⁺	4d ¹	1/2	Xanthine Oxidase	1.95-2.0	5/2

^aTable reproduced from reference 28.

TABLE V

Structure Sensitive Vibrational Modes of Heme Proteins^a

Heme protein	Ox. State	Spin State	ν_4	ν_3	ν_{11}	ν_{19}	ν_{10}
Cytochrome <u>c</u>	Fe(III)	l.s.	1374	1502	1562	1582	1636
Catalase	Fe(III)	h.s.	1370	1484	1549	1563	1622
DeoxyHb	Fe(II)	h.s.	1358	1473	b	1552	1607
Cytchrome <u>c</u>	Fe(II)	l.s.	1362	1492	1548	1584	1620
CN ⁻ Ferro-HRP	Fe(II)	l.s.	1362	1498	1545	1587	1620
CN ⁻ Ferri-HRP	Fe(III)	l.s.	1375	1497	1562	1590	1642

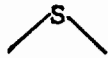
^aFrequencies in cm^{-1} , h.s. = high spin, l.s. = low spin, b = not observed, Hb = hemoglobin, HRP = horseradish peroxidase.

FIGURE LEGENDS

- Figure 1. Electron density maps of a tyrosine residue of rubredoxin showing the dependence of structural details on the resolution and phase refinement. (A) Resolution 2.0 Å, phases determined by isomorphous replacement. (B) Resolution 2.0 Å, phases calculated using a model. (C) Resolution 1.5 Å and phases calculated. (D) Fully refined map at 1.2 Å resolution with optimum positions of the atoms indicated. Figure reproduced from reference 8.
- Figure 2. EXAFS of reduced and oxidized copper in plastocyanin. Figure reproduced from reference 13.
- Figure 3. 300-MHz ^1H NMR spectra of pink and purple uteroferrin (1 mM) in 100 mM sodium acetate buffer, pH 4.9, at 30°C. Figure reproduced from reference 25.
- Figure 4. EPR spectra of the fluoride (A) and azide (B) complexes of horse erythrocyte catalase. Figure reproduced from reference 33b.
- Figure 5. EPR spectra of ferrous manganese peroxidase with ^{14}NO (A) and ^{15}NO (C) and of ferrous horseradish peroxidase with

^{14}NO (B) and ^{15}NO (D). Figure reproduced from reference 34b.

Figure 6. Resonance Raman spectrum of purple acid phosphatase. Excitation used was 514.5 nm, at 5°C and protein concentration was 5 mM. Reproduced from reference 46.

Figure 7. Resonance Raman spectrum of spinach ferredoxin. Excitation used was 488.0 nm, at 15K with a protein concentration of 2 mM.  = bridging mode, Cys = terminal mode. Reproduced from reference 64.

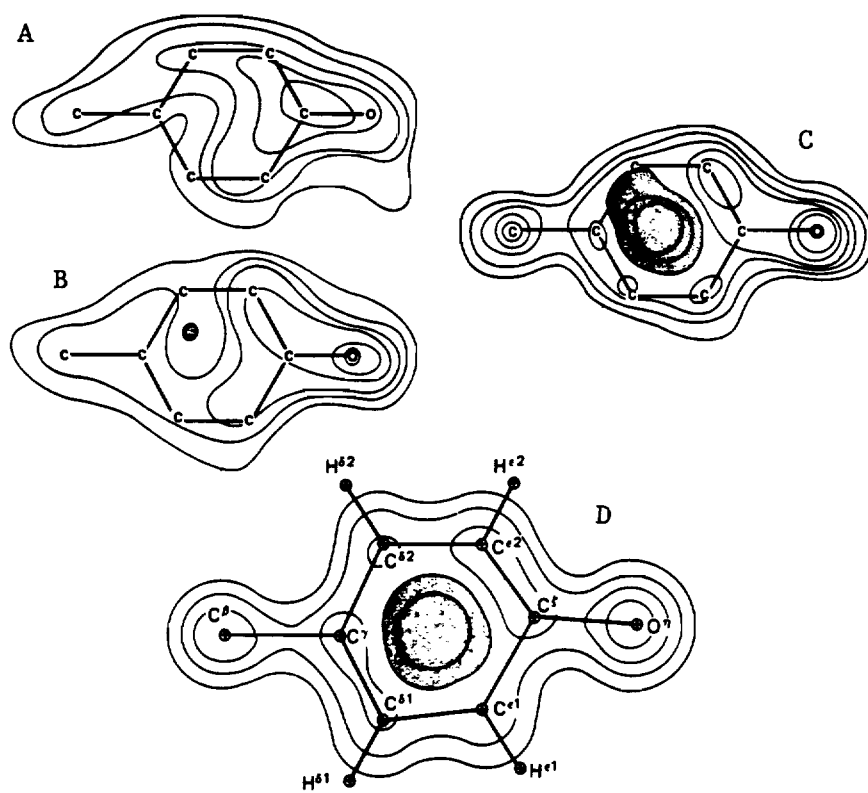


FIGURE 1

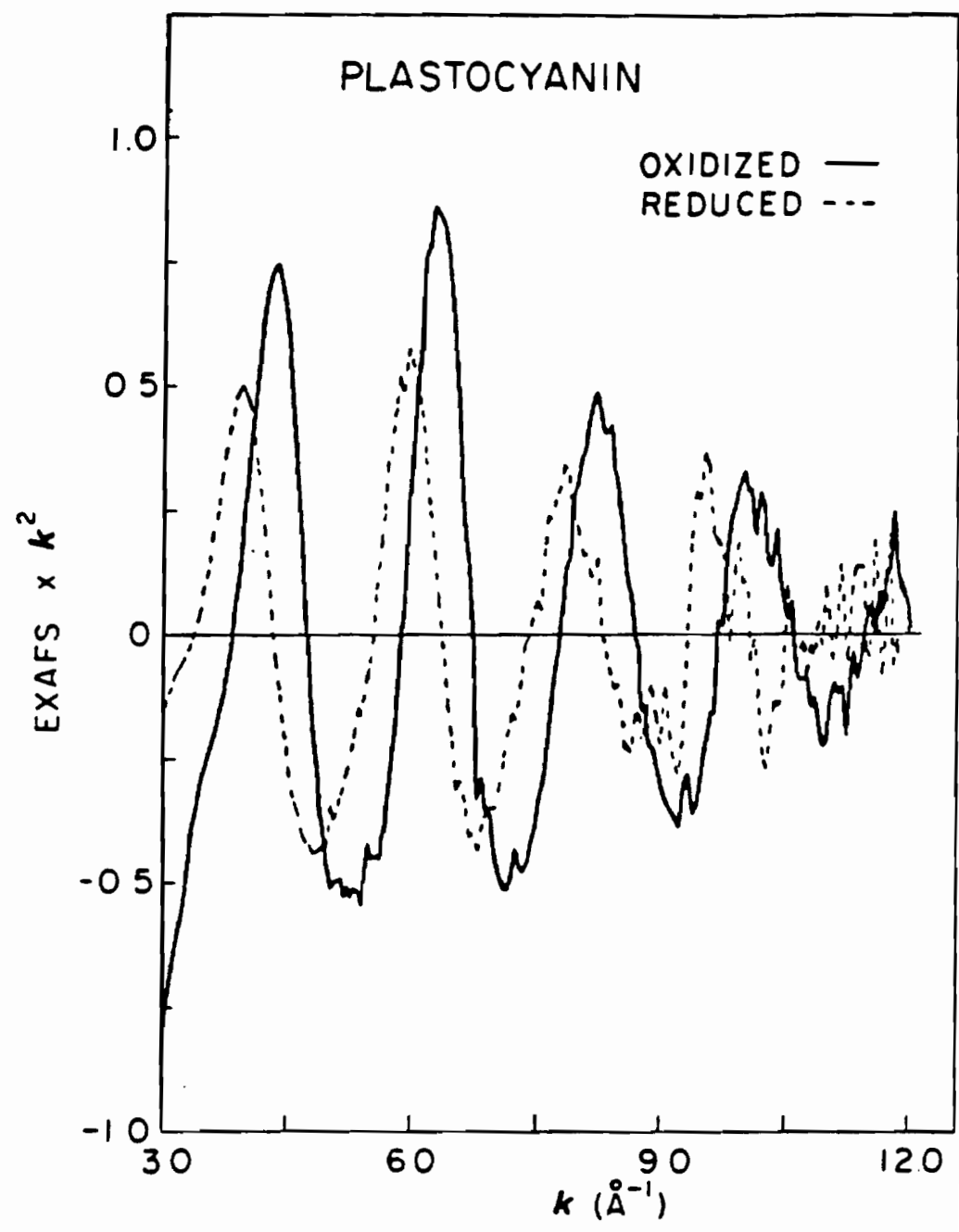


FIGURE 2

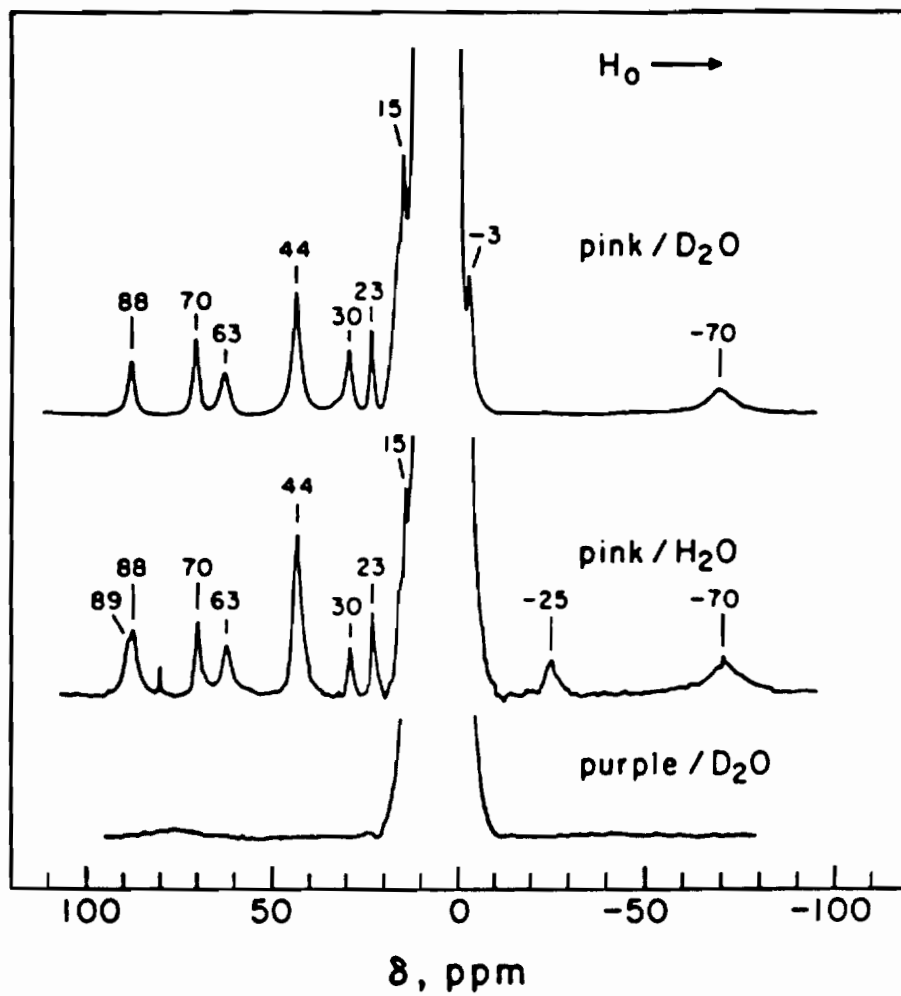


FIGURE 3

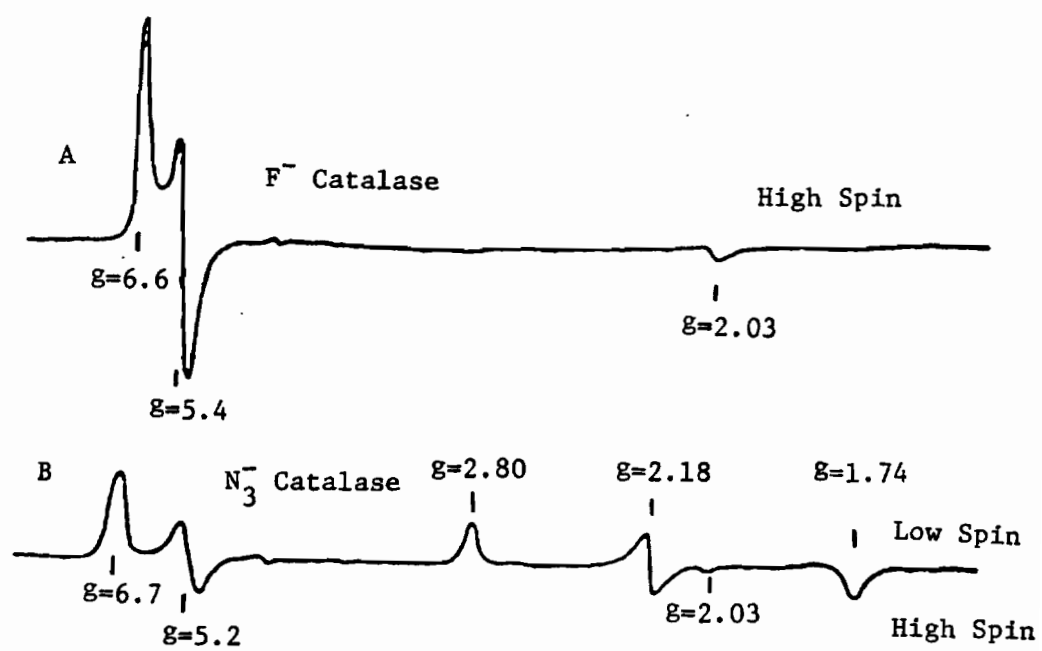


FIGURE 4

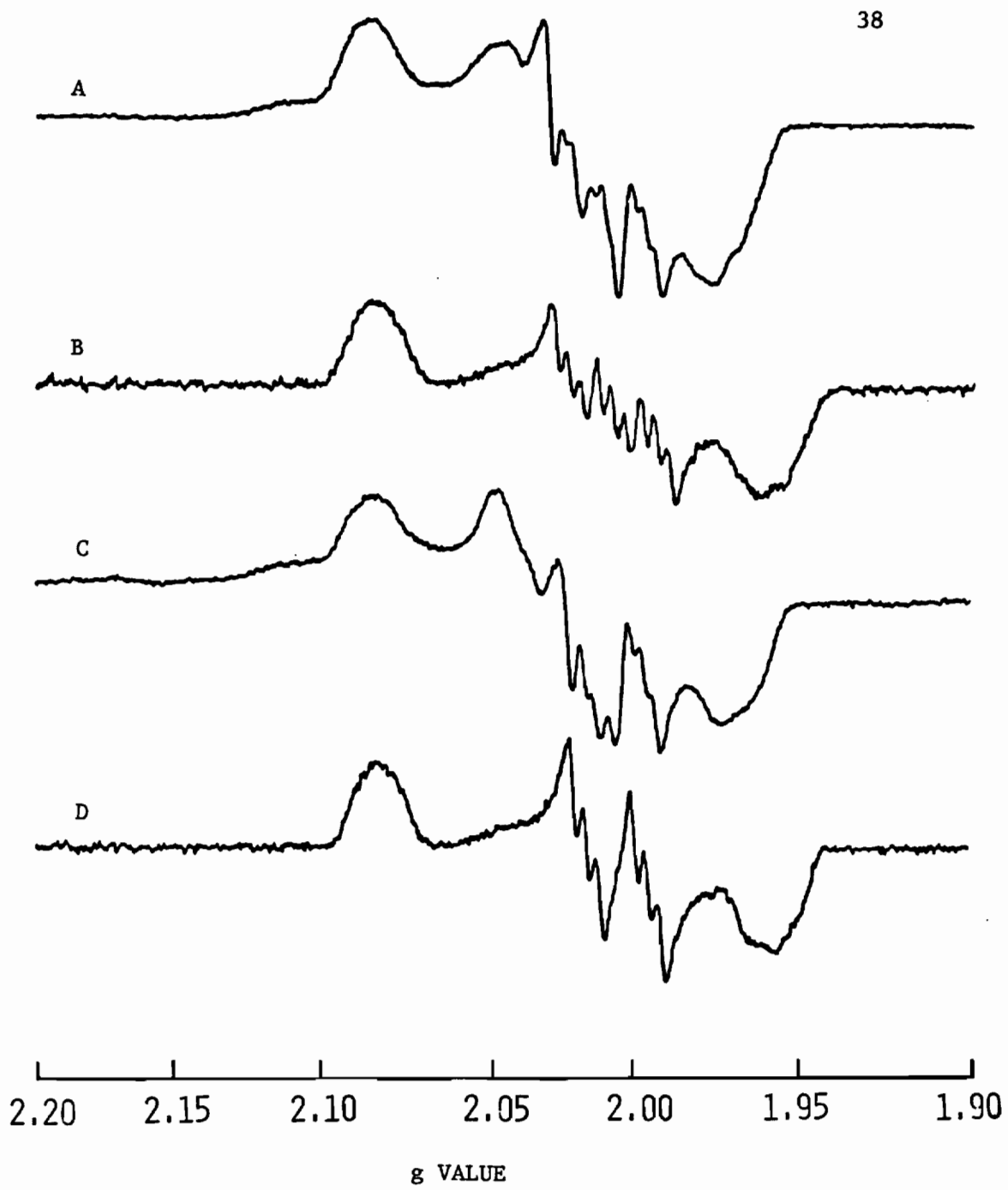


FIGURE 5

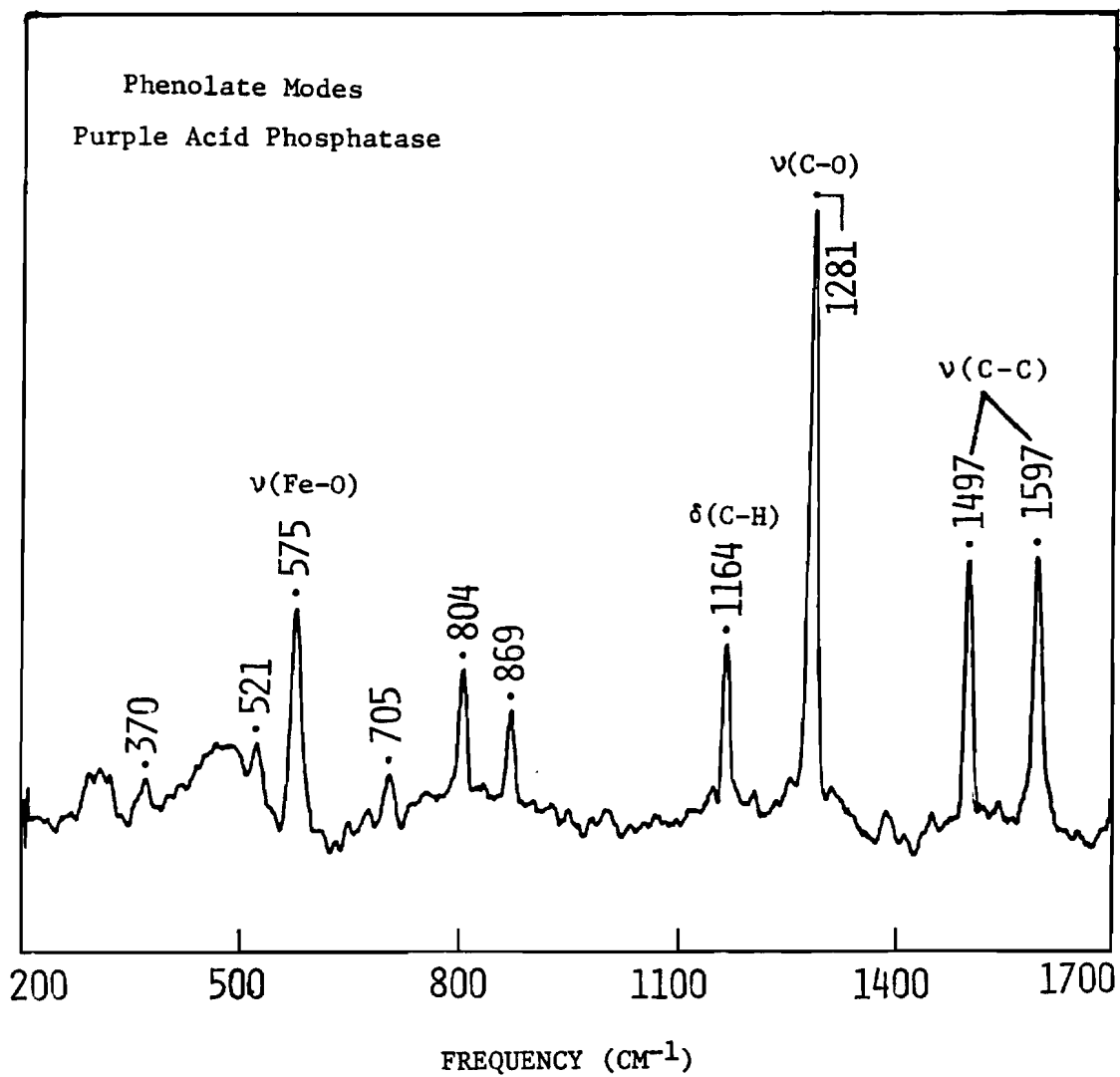


FIGURE 6

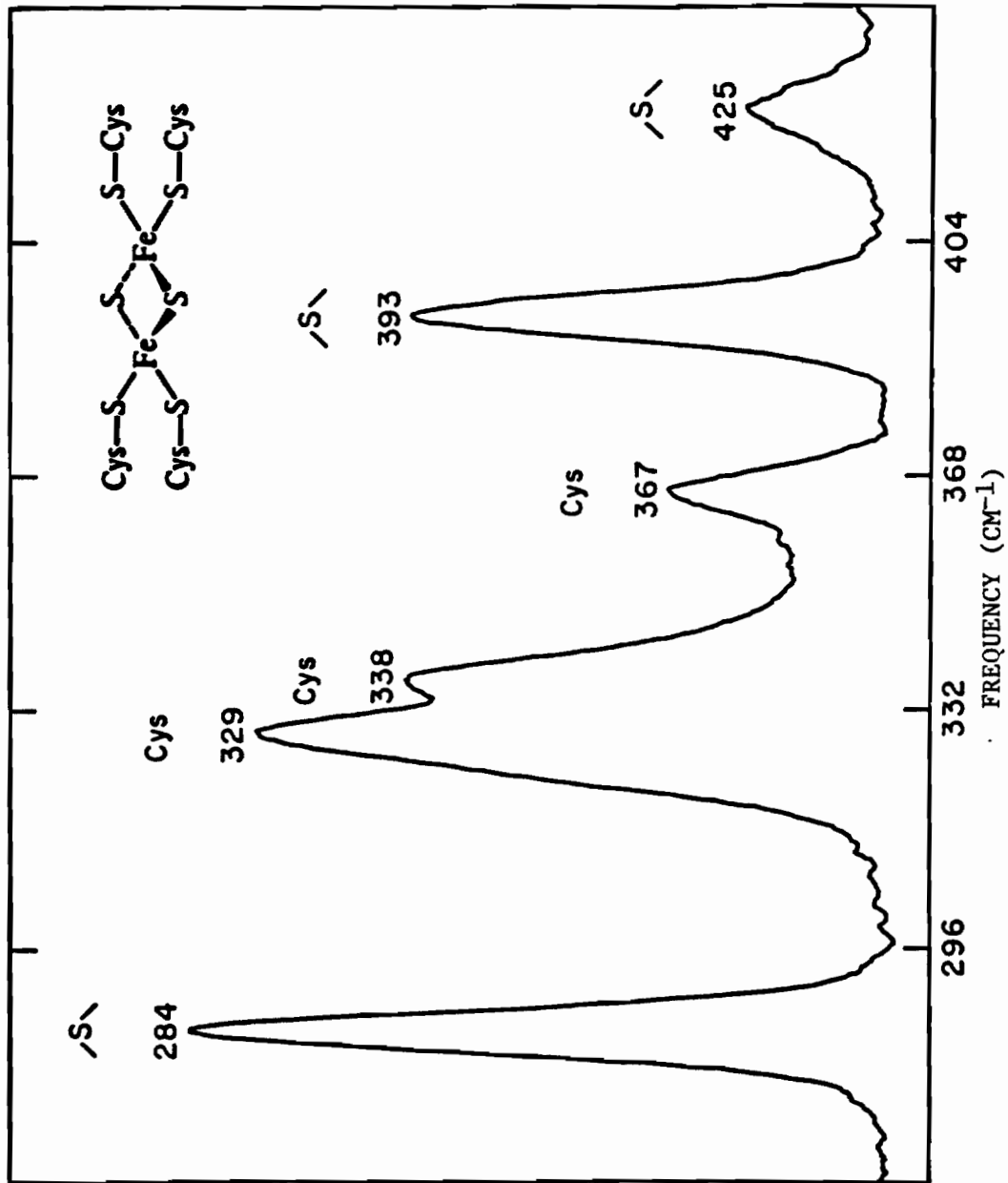


FIGURE 7

CHAPTER II

EXPERIMENTAL METHODS

The purpose of this chapter is to provide greater experimental detail than in the individual chapters on each topic. This section includes Raman instrumentation and spectral conditions such as temperature, scattering geometry, state of the samples and quantitation of peaks. Further, it discusses the effect of various factors like grinding on the intensities of the sulfate and the nitrate peaks used as frequent internal standards of intensity for resonance Raman enhancement profiles. Furthermore, the effect of devices such as the polarization analyzer, scrambler and rotator on the intensity of Raman peaks in solution is discussed.

RAMAN INSTRUMENTATION

The Raman spectra were obtained with a computer-interfaced Jarrell-Ash spectrophotometer as has been previously described in a publication from this laboratory (1). The source of incident radiation was provided by Spectra Physics 164-05 (Ar) or 164-01 (Kr) or 2025-11 (Kr) ion lasers. An RCA C31034A photomultiplier tube at -25°C was the detector with an ORTEC model 9302 amplifier/discriminator. The Raman spectra of the cytochromes and some of the catalase samples were obtained using a Computer

Automation computer system and graphics terminal as described in detail in reference 1. However, an upgraded system using an Intel 310 computer and a Tektronix 4054 A graphics terminal was used to collect Raman spectra of amicyanin, hemocyanin and many of the catalase samples. Absorption spectra of Raman samples were obtained on a Perkin Elmer Lambda 9 spectrophotometer.

CATALASE PREPARATIONS

Bovine liver catalase was purchased as a crystalline suspension in alkylbenzyltrimethylammonium chloride from Boehringer Mannheim. Further purification was done by the method of Eglinton et al. (2). The suspension of catalase was subjected to exhaustive dialysis against de-ionized water and then against 0.02 M phosphate buffer, pH 7.0 to remove the ammonium chloride and other impurities. The dialyzed sample was centrifuged at 10,000 r.p.m. (12,000 x g in an Sorvall SS-34 rotor) and the pellet was dissolved overnight in 1.0 mL of HEPES buffer (0.05 M, pH 7.0) at 4°C. This yielded a concentrated solution containing 0.55 mg protein/mL (~220 μ M in catalase based on a molecular weight of 240,000). Further concentration was not possible. Catalase samples at pH 9.0 were prepared by dialysis of the 220 μ M solution against Tris/HCl buffer (0.05 M, pH 9.0).

Another method of preparation following Browett and Stillman (3) involved heating the dialyzed sample for ~15 minutes at 37°C in a water bath/shaker (New Brunswick Scientific, Gyrotory water bath/shaker) to dissolve the protein. The solution of catalase was then

concentrated using a Centricon 10 (Amicon) or Sartorius 10 (Sartorius) ultrafiltration membrane along with centrifugation. The resulting concentrated solution ($\sim 200 \mu\text{M}$) was used for Raman experiments. Concentration of catalase using immersible Millipore filters (CX NMWL 10 K Dalton) was also attempted but was hindered by excessive conglomeration of catalase at the membrane due to concentration polarization. The catalase sample obtained from the first method, especially at pH 9.0, gave the best Raman data.

Aspergillus niger catalase was bought as a lyophilized solid from Calbiochem Laboratories. The solid protein was dissolved in either 0.05 M, pH 7.0 phosphate or HEPES buffer to give a protein concentration of $\sim 340 \mu\text{M}$. This solution was used for Raman experiments without further purification. A purified frozen sample of Aspergillus niger catalase ($\sim 240 \mu\text{M}$ in phosphate buffer, pH 7.0) received from Dr. James Turner (Virginia Commonwealth University) was also used for Raman experiments. Both the samples gave equally good data with Soret excitation but both had a high fluorescence background with visible excitations. A purified, frozen sample of Micrococcus luteus catalase in phosphate buffer (pH 7.0) was also obtained from Dr. Turner. The concentration of the stock solution was $110 \mu\text{M}$ in protein which was diluted to $\sim 55 \mu\text{M}$ for Raman studies using a 90° scattering geometry.

Raman spectra of catalases were generally collected using a 150° back-scattering geometry in melting point capillaries in a Dewar fitted with a copper cold finger in ice (4). We tried to collect spectra at low temperature ($\sim 15 \text{ K}$) using a closed-cycle helium

Displex (Air Products), but the quality of the data was surprisingly poor.

To assist in the assignments of various vibrational peaks, polarization measurements were carried out on catalases in capillaries at room temperature with 90° scattering geometry. The incident beam was allowed to pass through a polarization rotator and the scattered beam was collected at 90° to the incident beam after passing it through a polarization analyzer and a scrambler. The analyzer was rotated by 90° to collect scattered light polarized parallel and perpendicular to the polarization of the incident beam. For scattering at 90° geometry, the laser light was loosely focussed on the samples and the power of the incident beam was kept low for fear of degrading the samples.

All the catalase samples (mammalian, fungal as well as bacterial) fluoresced considerably, especially with visible excitation (488.0 and 514.5 nm) and back-scattering geometry. This gave rise to very high backgrounds and increased the noise level of the spectrum. Addition of 45 mM pyruvate, a potential fluorescence quencher (5) had no significant effect. Although KI has also been used as a fluorescence quencher for numerous proteins (6-8) we decided not to use it because of its tendency to disrupt protein structures (9, 10). Unfortunately, hydrogen peroxide (the substrate for catalase) reacts with KI making it impossible to test the disruptive effect of KI on catalase activity.

Further purification did not seem to reduce the fluorescence of the different catalases. The extensively purified A. niger catalase

of Dr. Terner did not give significantly better data than that from Calbiochem Laboratory which was used without further purification. To overcome this problem, multiple scans were added and the resultant spectrum was subjected to a computer generated background correction. Overall, the quality of the data obtained at 90° and 150° scattering geometry were comparable.

A sample of M. luteus catalase purified through DEAE, Sephacryl and hydroxylapatite columns following the method of purification from reference (11) was also obtained from Dr. J. Terner. This catalase also did not give good Raman spectra in the visible region. However, later it was found that catalase is denatured by freezing and the samples of A. niger and M. luteus catalases received from Dr. Terner were in frozen state. It is possible that the increased noise level in their Raman spectra were due to partially denaturation of catalase. Finally, yet another set of purified samples of M. luteus catalase (fractions A, B and C with respective heme concentrations of ~125 μM , ~55 μM and ~45 μM , $\epsilon = 100,000 \text{ M}^{-1} \text{ cm}^{-1}$ per heme) packed in ice was obtained from Dr. Terner. The A fraction was used for Raman studies. It showed a good signal-to-noise ratio, gave much better Raman signals and fluoresced less than any other catalase studied so far. Polarization studies were also carried out on this sample.

In order to find out the cause of the high fluorescence of catalases upon excitation in the visible region (>450 nm), we undertook some fluorescence measurements. It is well known that tryptophans present in proteins usually fluoresce near 350 nm when excited at 280 nm (12). When they are photooxidized, they are seen to

fluoresce at ~460 nm with an excitation of 360 nm. This has been observed for both Fe and Cu proteins (13).

On excitation of a bovine liver catalase solution (1.2 μ M in 0.05 M, pH 7.05 phosphate buffer) at 280 nm, three fluorescence emission features were observed at ~325, ~450, and 610 nm (Fig. 1A). The peaks at 560 nm and 840 nm are due to overtones of the 280 nm excitation. The broad fluorescent feature at 325 nm with a shoulder at lower energy must be due to tryptophan residues in catalases. The feature at ~450 nm which has its excitation maximum at 360 nm (Fig. 1B) must be due to the presence of photooxidized tryptophan residues. However, the fluorescence excitation profile has negligible intensity below 420 nm, indicating that this cannot be the species responsible for the fluorescence of catalases with 457.9 - 514.5 nm laser Raman excitation. Excitation of metal-free porphyrins in the Soret region (~410 nm) produces fluorescence near 600 nm (14); excitation within the β band (~530 nm) is also expected to yield fluorescence maxima in the 600-700 nm region (15). No such fluorescent maxima were observed using visible excitation (450 nm, 500 nm, 550 nm, or 620nm) with either 1.2 μ M catalase (as in Figure 1) or with 36 μ M catalase. Nevertheless, at the 10-fold higher concentrations used for Raman experiments a fluorescent component is definitely appearing in the Raman data. It is likely to be due to the presence of some partially-degraded porphyrin or to some zinc-porphyrin (14) in the catalase sample, despite the fact that the expected fluorescence spectrum was not detected at lower concentrations.

In hopes of being able to better identify the tyrosinate Raman peaks, catalase from M. luteus was converted to its low-spin cyanide derivative. Fraction B of Dr. Terner's M. luteus catalase (3 mL, ~55 μ M) was subjected to dialysis with Tris/HCl 0.05 M, pH 9.0 to increase the pH of the catalase solution. This was necessary to avoid the formation of hydrogen cyanide gas at lower pH on addition of NaCN to catalase at pH 7.0. The dialyzed solution was then concentrated to ~200 μ M using a Sartorius 10 ultrafilter with centrifugation. To 45 μ L of this M. luteus catalase solution, 5 μ L of 0.5 M NaCN solution (in Tris/HCl 0.05 M, pH 9.0) was added to give a final concentration of 180 μ M in catalase and 0.05 M in CN^- . The Raman spectrum of the cyanide derivative was obtained with 90° geometry at room temperature; sample stability against thermal decomposition was aided with air cooling from a 4" muffin fan. The presence of interfering porphyrin modes made it difficult to identify tyrosinate ligand vibrations in this sample.

CYTOCHROMES \underline{c}_1 AND \underline{c}

Samples of cytochromes \underline{c}_1 , \underline{c} , their mixture with and without hinge protein, and \underline{c}_1 with hinge protein were obtained from Dr. Tsou King and Dr. Chong H. Kim (State University of New York at Albany). The samples arrived in a frozen state in capillaries and were stored at -40°C. Raman experiments were performed at liquid N₂ temperature (~90 K) in the original capillaries. Care was taken not to thaw them during transfer. This was done by taking one capillary at a time

from the storage at -40°C and putting it in a liquid nitrogen Dewar until ready for use. For Raman studies the frozen capillary was wiped quickly and put in a Dewar with a copper cold finger immersed in liquid nitrogen. The scattering geometry used was 150° back-scattering. Multiple scans were added together to improve the signal-to-noise ratio.

COPPER COMPLEXES

The potential model complexes for blue copper proteins were studied using electronic absorption and Raman spectroscopy. These samples were received as crystalline materials from Dr. Hans Toftlund (Odense University, Denmark). For Raman studies, the solids were mixed with sodium sulfate as an internal standard. The ratio of sulfate to sample varied, depending on the resonance enhancement of the sample. Typical values were 1 mg of sample and 10 mg of sodium sulfate.

First a weighed amount of anhydrous sodium sulfate crystals were ground by hand for ~5 minutes in a mortar with pestle. Then the weighed amount of sample was added to it and mixed. The mixture was again ground to ~3 minutes by hand. The resultant powdered sample was firmly packed into the circular groove of a stainless steel sample holder (Fig. 2) by pressing with a tamper. The stainless steel tamper has a raised ring corresponding to the circular groove in the sample holder. The sample holder was then gently tapped to check if the sample was packed firmly and that the sample would not

fall off during the rotation of the spinning cell. The sample holder was then attached to the shaft of a rotating spindle on a motor from Harrison Laboratories (model 6347A) (Fig. 2). Typical rates of rotation are 500-1000 revolutions/min.

The Raman spectra of the solid samples were obtained with a 150° back-scattering geometry at room temperature. For isotopic samples, the Raman data were collected consecutively. The peak areas of the major peaks were compared with those of sulfate at $\sim 990\text{ cm}^{-1}$ by cutting the peaks out of the plotted spectrum and weighing them. Their molar scattering intensities were calculated as the ratio of weight of the sample peak to that of sulfate peak multiplied by the ratio of moles of sulfate to that of the sample.

The Raman spectra of some of the samples were also obtained in solution so as to check the similarity of the solution and solid state spectra. In order to correlate the vibrational peaks to the absorption spectra, Raman spectra were obtained at various wavelengths. Electronic spectra were obtained on samples in the solution state. The best solvents for these complexes were methylene chloride, methoxyethanol and 1:1 v/v of MeOH:EtOH.

IRON COMPLEXES

Two iron complexes received from Dr. Harold Goff (University of Iowa) were studied by Raman spectroscopy. The complexes are the monomer and dimer of 5-(2-hydroxyphenyl)-10,15,20-(tritolyl)Fe(III) porphyrin (16). The Raman spectra of both the monomer and the dimer

were collected on solids. About 5 mg of monomer and 10 mg of dimer were ground separately with 100 mg of KBr. The samples were then packed firmly in a circular groove of a spinning sample holder and the data were collected with a 150° back-scattering geometry.

For polarization measurements, solutions of monomer and dimer were made either with methylene chloride or carbon disulfide (0.5-1 mg/mL). The incident beam was passed through a polarization rotator whereas the scattered beam was passed through an analyzer and a scrambler. The analyzer was rotated by 90° to get data parallel and perpendicular to incident beam polarization. The scattering geometry used for these measurements was 90° and the data were collected both at room temperature and from -15° to -35°C. For room temperature studies, the laser beam was not focussed at the sample and the power was kept low so as not to decompose the samples. Lower temperatures were obtained by using a Varian E-4540 variable temperature controller. Samples were loaded in a melting point capillary and were held in a jacketed glass tube through which cooled N₂ gas was flowed. The nitrogen gas was cooled by passing through a bath of methanol in dry ice. A flow rate of 10-20 SCFH was used.

FACTORS AFFECTING RESONANCE RAMAN SCATTERING INTENSITY

One of the main purposes in obtaining Raman spectra of the models for the blue copper proteins was to calculate the molar scattering intensity of the spectral peaks. Sodium sulfate was selected as an internal standard. The sample and the sodium sulfate

were ground to obtain a homogeneous mixture. However, some difficulties were encountered. Based on repeated experiments with Na_2SO_4 and K_2SO_4 by timed grinding in a steel mill (Wig-L-Bug), it was found that as the grinding time increased, the intensity of the ν_1 Raman peak of sulfate ion at 991 and 983 cm^{-1} , respectively, decreased (Fig. 3A). The absolute Raman intensities were measured as the peak heights above the same background using the same plot gain. In each case, very little decrease in intensity occurred when the steel mill grinding time was between 30 seconds to one minute, but a ~50% decrease in intensity occurred after 8-10 minutes of grinding.

When sulfate salts were ground by hand using a mortar and pestle, there was significantly lower loss of intensity with grinding time (Fig. 3B). However, considerable scatter was observed in the peak intensities, the readings being accurate to only $\pm 20\%$. These were the conditions used for the studies of the model compounds. A similar degree of uncertainty appears to apply to the intensity of the copper complex itself such that the resultant intensity ratios for the sample relative to sulfate are only accurate to $\pm 40\%$.

A plausible explanation for the effect of grinding on the intensity of the sulfate Raman peak could be the change in grain size which is an important factor in determining the extent of light dispersion and this, in turn, affects the intensity of the Raman peak (17). Further, as the grain size gets reduced, more incident light is reflected back from the surface of the medium and thereby reduces the relative proportion of Raman scattered light. Interestingly, when potassium nitrate was subjected to grinding in a steel mill,

there was no such drastic effect of grinding time on the peak intensity of the $\nu_1 \text{NO}_3^-$ peak at $\sim 1050 \text{ cm}^{-1}$ (Fig. 3C). These experiments indicate that KNO_3 may be a better internal standard for solid samples. In either case, it is advisable to keep grinding to a minimum, just sufficient to mix the sample.

Further experiments were carried out to see the effect of the physical state of the sample on the Raman intensities of sulfate and nitrate internal standards. It was found that the two ions in solution at room temperature exhibited similar molar scattering intensities (Table I). However, when the same solutions are frozen at 90 K, there is 2.8 fold decrease in the intensity of sulfate peak relative to that of nitrate. Also, the intensity of the sulfate peak appears to be more greatly affected by the change from the solution state to the solid state at room temperature. This results in a 1.3 fold decrease of the sulfate peak relative to the nitrate peak. These results suggest that nitrate may be preferable to sulfate as an internal standard in frozen solutions as well as in solids. The lack of reliability of sulfate was initially observed in determining the molar scattering intensity of the 430 cm^{-1} mode of amicyanin. The ratio of amicyanin to sulfate at room temperature was 3.3-fold greater than at 90 K (Table I), similar to the 2.8-fold change seen for the nitrate to sulfate ratio in frozen solution. Although differential freezing of solutes could be a factor in a protein solution, it is less likely to explain the discrepancy in the nitrate and sulfate mixture.

Another set of experimental variables which can affect Raman scattering intensity relates to the polarization of the incident laser light at the sample and the scattered light reaching the monochromator. For a 90° scattering geometry (Fig. 4A), the incident beam is passed through a polarization rotator to optimize the Raman scattering at 90°. The scattered light is then passed through a polarization scrambler to correct for the polarization sensitivity of the gratings. To enhance sample stability, solutions often need to be cooled and, hence, are most conveniently placed in a Dewar (4) which requires a 150° back-scattering geometry (Fig. 4B). Although one might expect this to be close to optimal conditions for Raman scattering, we find that the 150° orientation significantly reduces the Raman scattered intensity. This can be seen in Table II which compares the intensities of the ν_1 (polarized) and ν_4 (depolarized) lines of CCl_4 at 459 and 314 cm^{-1} , respectively. With backscattering and the use of the rotator, the intensity ratio of I_{459}/I_{314} is comparable to that for the 90° geometry, but the total intensity in both lines is reduced approximately two fold relative to 90° scattering. If the rotator is omitted altogether, the 459 cm^{-1} line is further reduced in intensity because of the high sensitivity of the totally symmetric ν_1 mode on the incident polarization direction. Hence a marked drop in the I_{459}/I_{314} ratio is observed. The decreased absolute intensities with 150° scattering are due to poorer optical efficiency since the light beam only grazes the surface of the sample rather than passing through a significant scattering volume as occurs with 90° scattering. The added glass surfaces of

the Dewar vessel further decrease the efficiency at comparable laser power.

A contrasting behavior is observed for 150° back-scattering from microcrystalline solid samples such as Na_2SO_4 . Rotation of the input plane of polarization has no effect on the intensity of Raman scattering. The reason for this is that solid samples tend to reflect and refract the input radiation such that it becomes scrambled with respect to polarization. This means that the intensity of polarized Raman lines relative to depolarized Raman lines would be lower in solid than in liquid samples. However, if both sample and reference modes are polarized lines, then the intensity ratios should be similar in solid and in liquid samples.

Quantitation of Depolarization Ratio

Valuable insight into the nature of the symmetry of a vibrational mode can be attained by analyzing the polarization of the scattered light. This is done by measuring the depolarization ratio ρ which is given by $\rho = I_{\perp} / I_{\parallel}$ where I_{\perp} and I_{\parallel} are the respective intensities of the scattered light polarized perpendicular and parallel to the plane of the incident light. The intensity of a Raman band is measured either by integration of the peak or by measuring its peak height. Accurate measurement of depolarization ratios requires additional optics such as a polarization analyzer and a scrambler (Fig. 4A). By measuring the depolarization ratio, the symmetry of a vibrational mode can be determined. For a solution

sample, when $0 \leq \rho \leq 0.75$, the band is said to be polarized and is indicative of the vibration being totally symmetric. When the band exhibits $\rho = 0.75$, it is said to be depolarized and this implies that the vibrational mode is nontotally symmetric. For example, the Raman spectrum of CCl_4 (Fig. 5) provides an excellent example of both totally and nontotally symmetric modes of vibrations. The depolarization ratios of the peaks at 459, 314, and 217 cm^{-1} are 0.025, 0.77, and 0.76 respectively (based on integration of the peaks) and are close to the literature values (18). Hence the peak at 459 cm^{-1} is the totally symmetric and those at 314 and 218 cm^{-1} are asymmetric vibrational modes. In case of resonance Raman scattering, certain modes may give $\rho > 0.75$ and are called anomalously polarized. This is specially true for heme proteins (19) whose porphyrin chromophores have a high effective symmetry (D_{4h}). Assignments of the huge number of resonance Raman bands of heme proteins have only been possible due to the measurement of their depolarization ratios.

REFERENCES

1. Loehr, T. M., Keyes, W. E., Pincus, P. A. (1979) Anal. Biochem. **96**, 456-463.
2. Eglinton, D. G., Gadsby, P. M. A., Sievers, G., Peterson, J., and Thomson, A. J. (1983) Biochim. Biophys. Acta. **742**, 648-658.
3. Browett, W. R., and Stillman M. J. (1979) Biochim. Biophys. Acta. **577**, 291-306.
4. Sjöberg, B.-M., Loehr, T. M., and Sanders-Loehr, J. (1982) Biochemistry **21**, 96-102.
5. Ando, T., and Miyata, H. (1983) Anal. Biochem. **129**, 170-175.
6. Weber, G. (1950) Biochem. J. **47**, 114.
7. Friedman, J. M., and Hochstrasser, R. M. (1975) Chem. Phys. Lett. **33**, 225.
8. Benecky, M., Li, T. Y., Schmidt, J., Frerman, F., Watters, K. L., and McFarland, J. (1979) Biochemistry **18**, 3471-3476.
9. Warren, J. C., Stowring, L., and Morales, M. F. (1966) J. Biol. Chem. **241**, 309-316.
10. Von Hippel, P. H., and Wong, K. Y. (1964) Science **145**, 577-580.
11. a) Jones, P., Pain, R. H. and Suggett, A. (1970) Biochem. J. **118**, 319-323.
b) Herbert, D. and Pinsent, J. (1948) Biochem. J. **43**, 193-202.
12. Finazzi-Agró, A., and Avigliano, L. (1984) Life Chem. Rep. **2**, 97-140.

13. Avigliano, L., Sirianni, P., Morpurgo, L. and Finazzi-Agrò, A. (1983) FEBS Letters **168**, 274-276.
14. Camadro, J.-M., Ibrahim, N. G., and Levere, R. D. (1984) J. Biol. Chem., **259**, 5678-5682.
15. Gouterman, M., Hanson, L. K., Khalil, G.-E., Buchler, J. W., Rohbock, K., and Dolphin, D. (1975) J. Am. Chem. Soc. **97**, 3142-3149.
16. Goff, H. G., Shimomura, E. T., Lee, Y. J., and Scheidt, W. R. (1984) Inorg. Chem. **23**, 315-321.
17. Sushchinskii, M. M. (1972) Raman Spectra of Molecules and Crystals (Israel Program for Scientific Translations Ltd; New York) Chapter III, 352-363.
18. Nakamoto, K. (1986) in Infrared and Raman Spectra of Inorganic and Coordination Compounds, 4th Ed., Wiley-Interscience, New York, Part I, pp 3-97.
19. Spiro, T. G., and Strekas, T. C. (1972) Proc. Natl. Acad. Sci. U. S. A., **69**, 2622-2626.

TABLE I

Comparison of Raman Peak Heights of $\nu_1(\text{NO}_3^-)$, $\nu_1(\text{SO}_4^{2-})$, and $\nu(\text{Cu-S})$ of Amicyanin at a Constant Excitation Power and Constant Plot Gain^a.

Peak Heights (cm)	Solution ^b	Solid ^c	Frozen solution ^d
<u>Experiment 1</u>			
Nitrate	9.6	198	5.6
Sulfate	9.6	158	2.0
Nitrate : Sulfate	1.0	1.3	2.8
<u>Experiment 2</u>			
Amicyanin	7.7	-	11.0
Sulfate	10.8	-	4.9
Amicyanin : Sulfate	0.71	-	2.2

^aNitrate/Sulfate data collected with 42 mW at 488.0 nm excitation and normalized to a plot gain of 0.27. Amicyanin/Sulfate data collected with 80 mW at 647.1 nm excitation and normalized to a plot gain of 0.145. ^bSpectra obtained at room temperature, 90° scattering geometry. Solution for first set contained 0.2 M K_2SO_4 and 0.2 M KNO_3 ; $\nu_1(\text{NO}_3^-)$ at 1047 cm^{-1} , $\nu_1(\text{SO}_4^{2-})$ at $\sim 980 \text{ cm}^{-1}$. Solution for second set contained 0.34 mM amicyanin and 0.3M K_2SO_4 ; $\nu(\text{Cu-S})$ at 430 cm^{-1} . ^cSolid contained equimolar amounts of K_2SO_4 and KNO_3 ground for 10 seconds in a steel mill (Wig-L-Bug), spectrum obtained at room temperature, 150° back-scattering geometry.

^d Solution samples from (b) run at 90 K, 150° back-scattering geometry.

TABLE II

Effect of Sampling Geometry and Light Polarization of the
Intensity of CCl_4 Modes^a

Geometry	Polarization Rotator ^b	Scrambler	Peak ht., cm		$I_{459} : I_{314}$
			I_{314}	I_{459}	
90°	Yes ^b	No	4.7	10.1	2.1
90°	Yes	Yes	4.0	8.0	2.0
150°	No	No	2.1	2.4	1.1
150°	Yes ^b	No	2.1	4.4	2.1
150°	Yes	Yes	1.9	4.0	2.1

^aAll spectra plotted at the same gain. ^bThe half-wave plate retarder is positioned so that the polarization is perpendicular to both the incident and scattered rays (Fig. 4).

FIGURE LEGENDS

- Figure 1. Fluorescence spectra of bovine liver catalase, $1.2 \mu\text{M}$ in 0.05 M phosphate buffer (pH 7.05). (A) Excitation of 280 nm, maximum intensity at 325 nm is 295 units. (B) excitation of 360 nm, maximum intensity at 451 nm is 16 units; * refers to overtones of the excitation wavelength.
- Figure 2. Use of spinning sample holder for solid samples at room temperature. The sample holder is a stainless steel disc with a hole in its center and an extended base on its outer surface. A set screw in the base is used to secure it to the shaft of the motor. The disc has a machined groove into which a sample can be packed, using a tamper with a matching machined bead.
- Figure 3. Effect of grinding time on the intensity of the ν_1 mode of sulfate and nitrate salts. The salts used were anhydrous K_2SO_4 (Mallinckrodt analytical reagent), K_2SO_4 (Morton Thiokol, Alpha, Ultra Pure), anhydrous Na_2SO_4 (Baker, Analyzed Reagent), and KNO_3 (Sigma). (A) Samples ground in a motor-driven steel mill. K_2SO_4 , Mallinckrodt (Δ), K_2SO_4 , Alpha (\square), Na_2SO_4 , Baker (\circ). (B) Samples ground by hand with a mortar and pestle. K_2SO_4 , Alpha (\square), Na_2SO_4 , Baker (\circ). (C) KNO_3 , Sigma sample (\bullet) ground in a

motor-driven steel mill. Raman spectra were obtained at room temperature, 514.5 nm excitation, 150° back-scattering from a spinning sample holder, and a scan rate of $1 \text{ cm}^{-1} \text{ s}^{-1}$. The laser power for (A) and (B) was 20 mW at the sample with a slit-width of 4 cm^{-1} whereas for (C) it was 30 mW with a slit-width of 5 cm^{-1} . The Raman data in (C) were collected by Dr. Gabriele Backes. The data were plotted using a constant plot gain for each sample set, with a shortest grinding time being given the maximum plot gain.

- Figure 4. (A) Instrumental setup for the measurement of depolarization ratio of a liquid sample using 90° geometry.
- (B) Arrangement showing 150° back-scattering geometry from a liquid sample.

- Figure 5. Raman spectra of CCl_4 at room temperature obtained with the broad band polarizer (analyzer) in the "Not Cut Down" (NCD) or parallel and "Cut Down" (CD) or perpendicular orientations. Conditions used are 514.5 nm excitation, laser power of 72 mW, slit-width of 5 cm^{-1} , scan rate of $1 \text{ cm}^{-1} \text{ s}^{-1}$, at room temperature with 90° scattering and one scan.

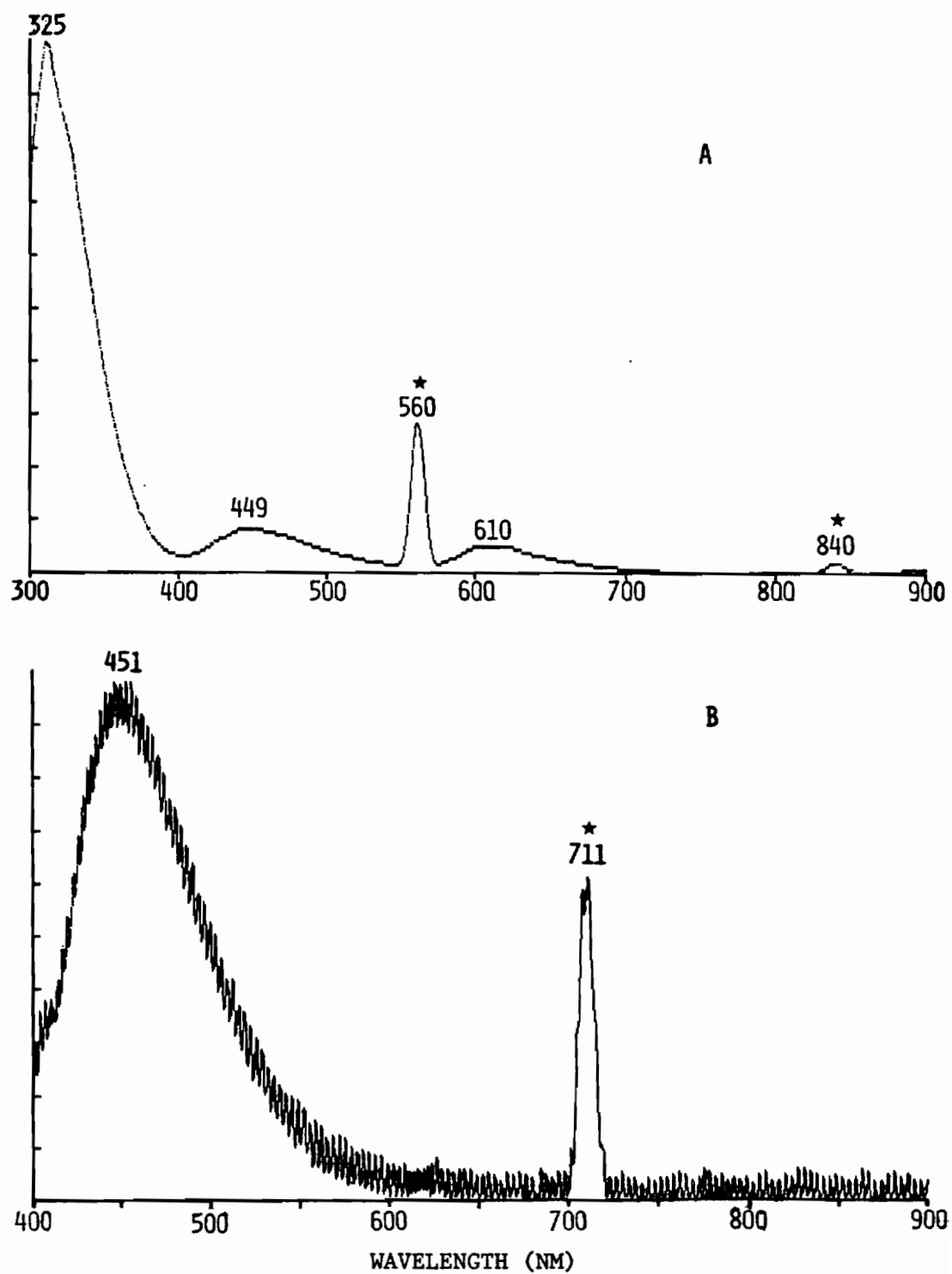


FIGURE 1

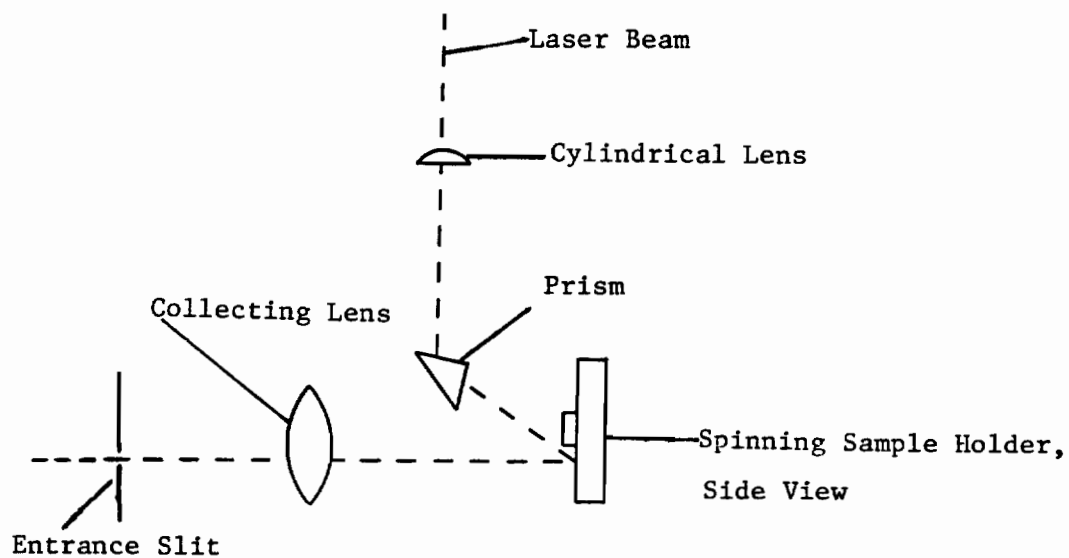
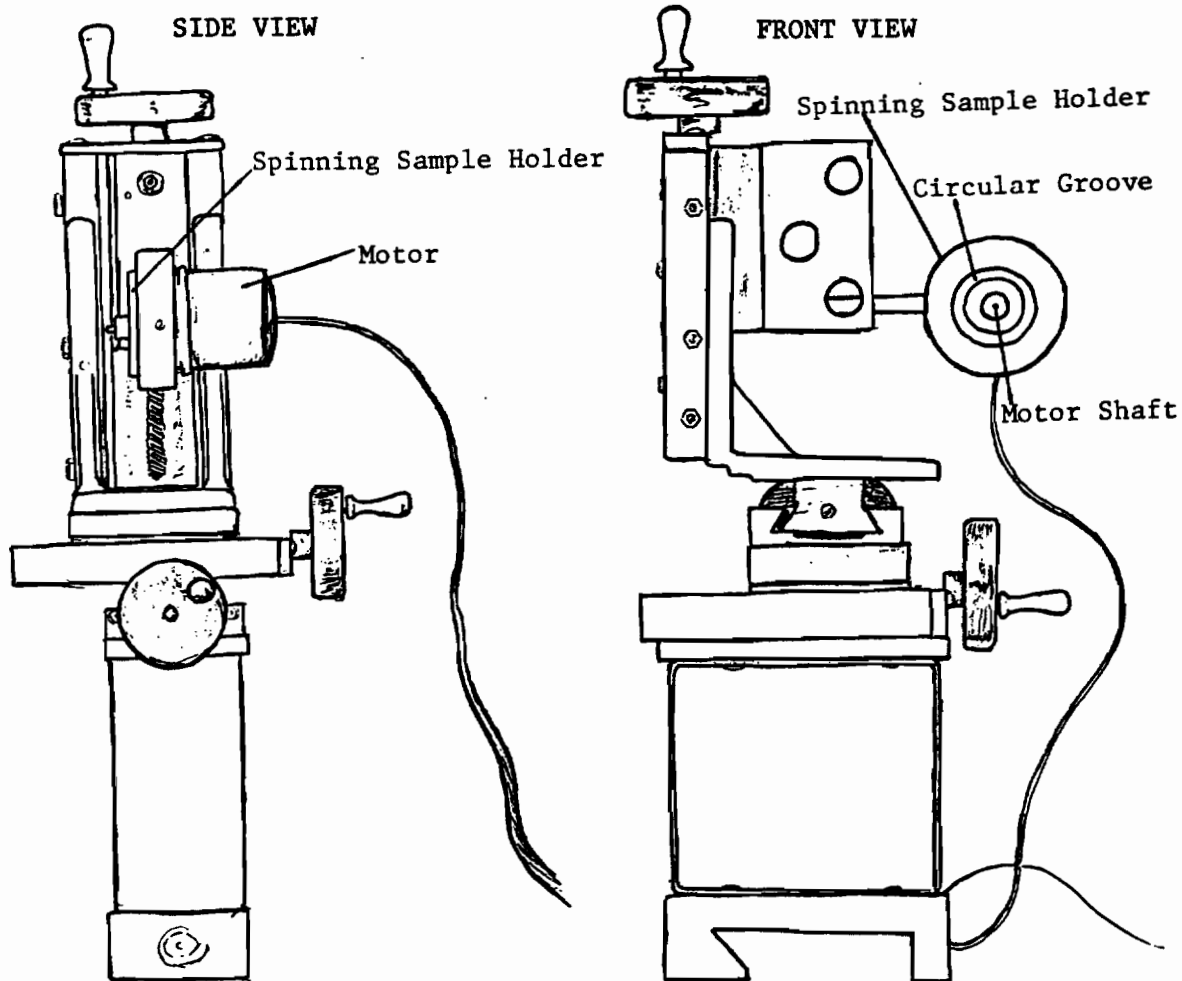


FIGURE 2.

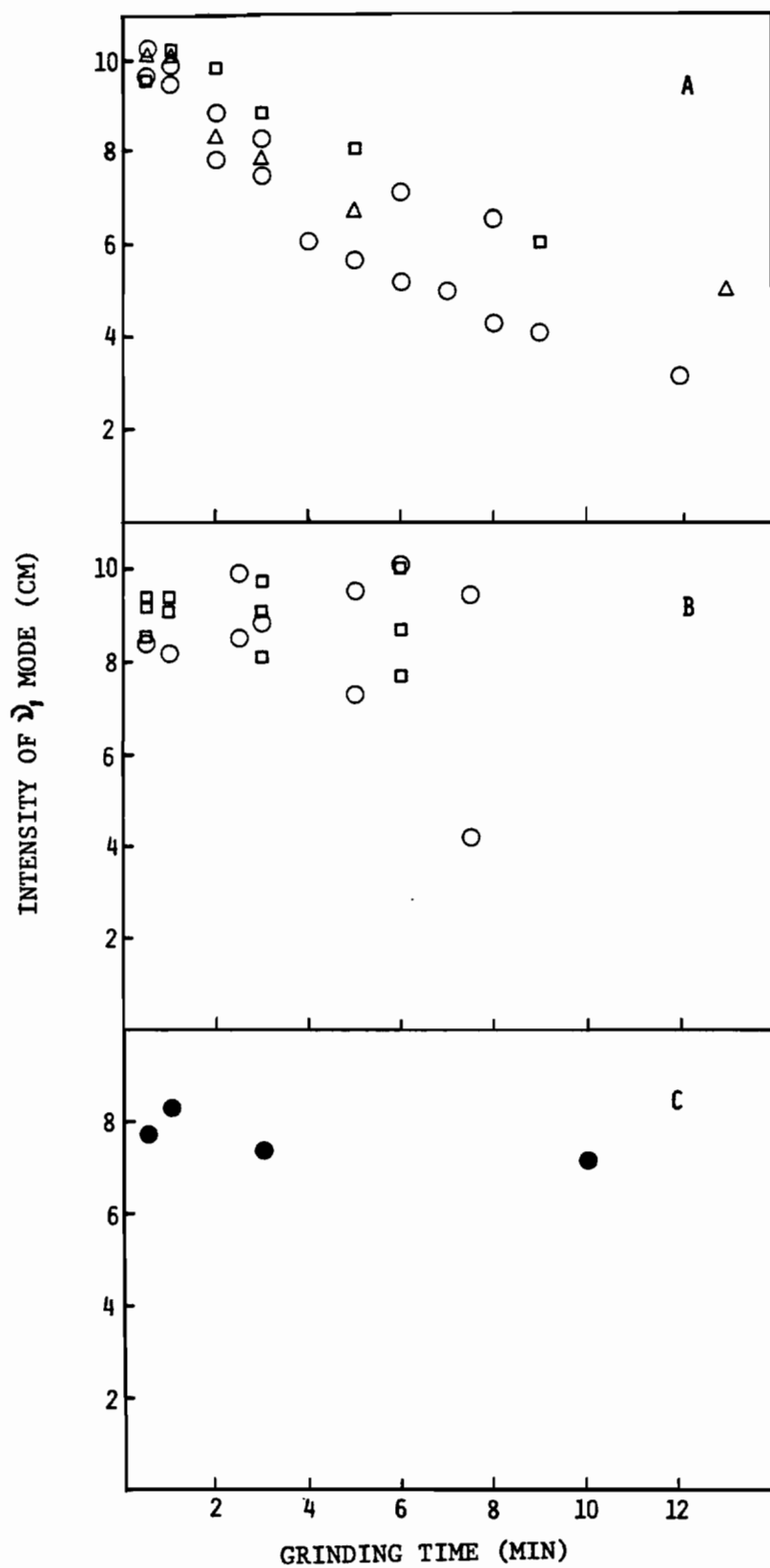


FIGURE 3.

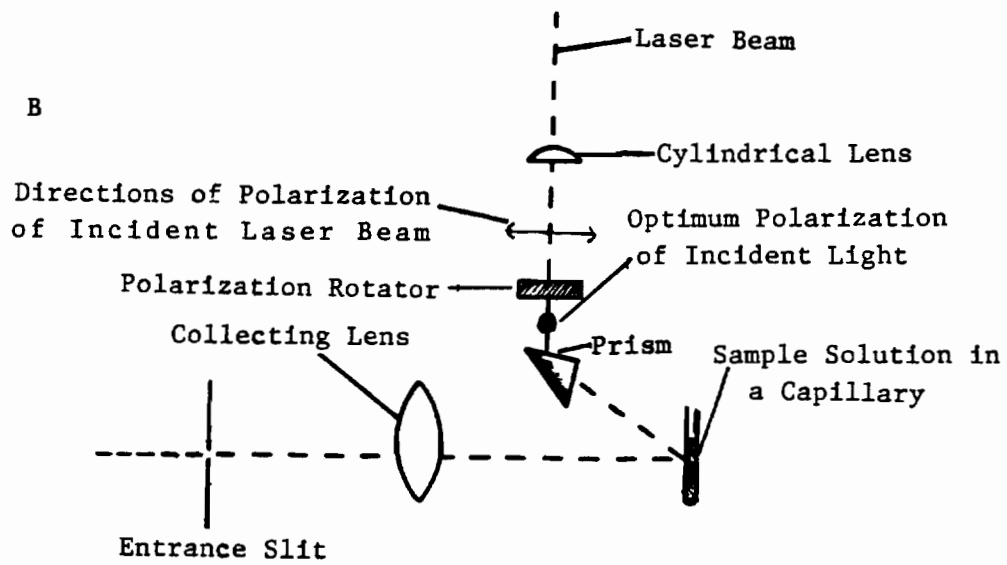
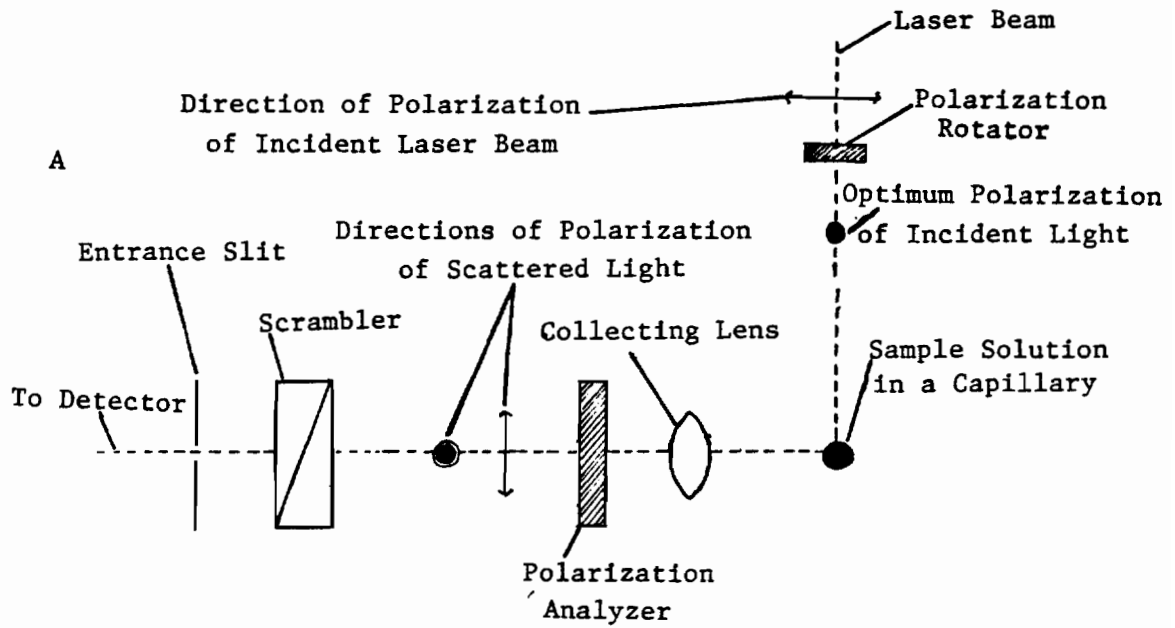


FIGURE 4

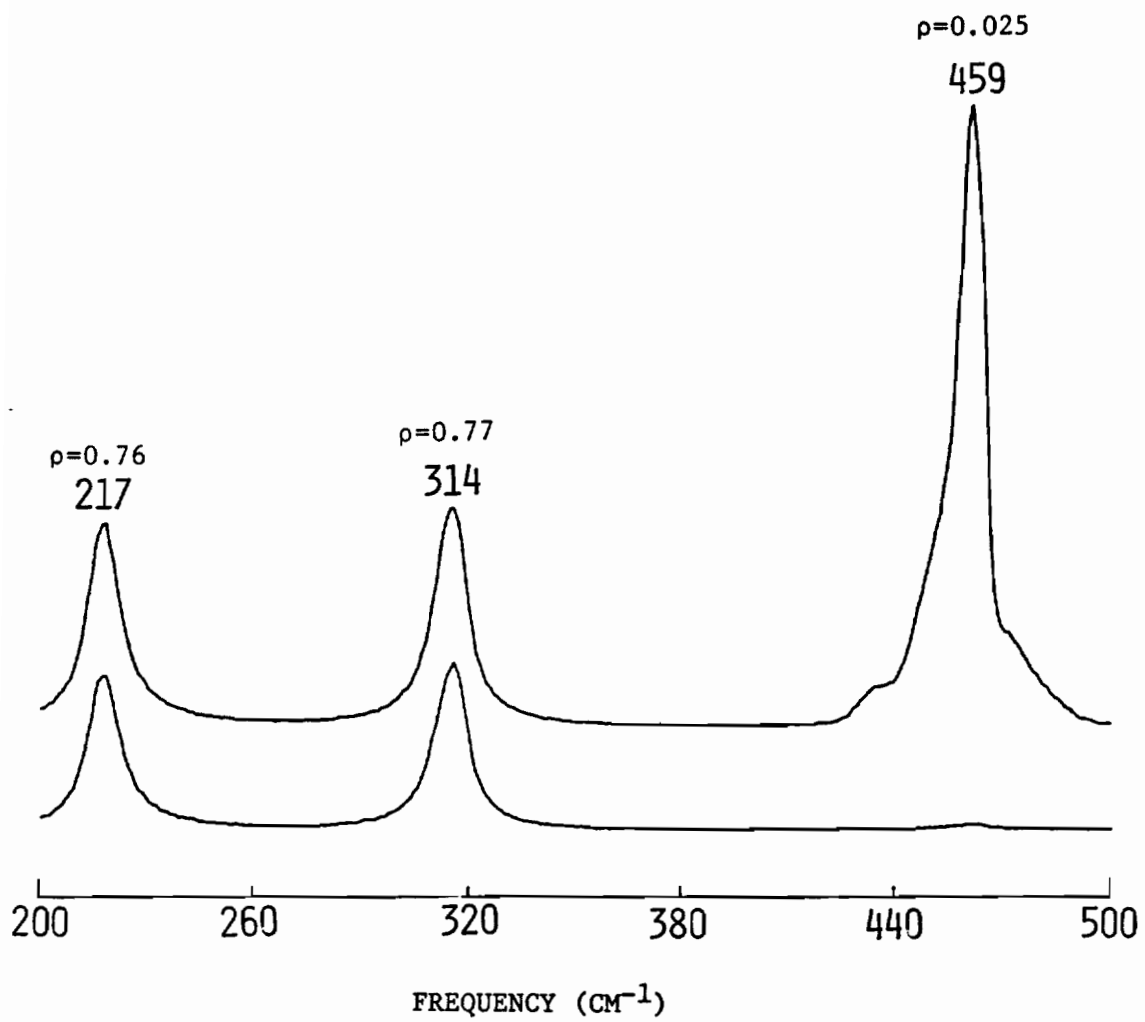


FIGURE 5

CHAPTER III

RESONANCE RAMAN SPECTROSCOPY OF AMICYANIN, A BLUE COPPER PROTEIN FROM Paracoccus denitrificans*

INTRODUCTION

The copper binding sites in a variety of copper-containing metalloproteins have unusual spectroscopic and chemical properties which has led to their description as blue copper proteins (1-3). This class of proteins exhibits intense visible absorption near 600 nm ($\epsilon = 3,000- 5,000 \text{ M}^{-1} \text{ cm}^{-1}$), paramagnetism in the oxidized state, abnormally small Cu hyperfine splitting in their EPR spectra, and relatively high redox potentials of 300 to 800 mV (compared to 170 mV for Cu(II) in aqueous solution). Proteins included in the blue copper category are azurin, plastocyanin, stellacyanin, plantacyanin, umecyanin, and rusticyanin. Most appear to function as redox catalysts in electron transfer pathways (3, 4).

Structural details of azurins from Alcaligenes denitrificans (5, 6) and from Pseudomonas aeruginosa (3, 7, 8) and of poplar

*The contents of this chapter have been published as an article by K. D. Sharma, T. M. Loehr, J. Sanders-Loehr, M. Husain and V. L. Davidson (1988) J. Biol. Chem., 263, 3303-3308.

plastocyanin (9, 10) have been obtained from X-ray crystallographic measurements. All three proteins have a similar eight-stranded β -barrel configuration in the polypeptide backbone, indicating that they are evolutionarily related. The copper-binding site in each case can be described as tri-coordinated Cu(II) in a distorted trigonal-planar environment with one cysteine thiolate and two histidine nitrogens as ligands. In addition, a weakly ligated methionine residue is present on the axial position making the structure distorted tetrahedral in plastocyanin and trigonal bipyramidal in the two azurins where there is a weakly interacting peptide carbonyl group serving as a second axial ligand. The copper ligands are held by the protein in a constrained framework, which in the case of plastocyanin is independent of the presence or absence or type of metal (10, 11). The intense absorption near 600 nm is attributed to a $S(\text{Cys})\sigma \rightarrow \text{Cu(II)} (d_{x^2-y^2})$ charge transfer transition of copper in a distorted tetrahedral or trigonal bipyramidal environment (12). Similarly, the axial type EPR signal ($g_{||} > g_{\perp} > 2$) and the small copper hyperfine splitting ($A_{||} < 65 \times 10^{-4} \text{ cm}^{-1}$) can be explained by a trigonal set of ligands with a symmetry lower than C_{3v} (12, 13).

A new low molecular weight blue copper protein named amicyanin has recently been isolated from several strains of methylotrophic bacteria, e.g. Methylobacterium strain AM1 (formerly Pseudomonas strain AM1) (14, 15), organism 4025 (16) and Paracoccus denitrificans (17). The amicyanins are similar to other blue copper proteins in their absorption and EPR spectra, but differ from them in their

primary structure and in their physiological role. The available amino acid sequence data on amicyanins (18-20) show considerably greater homology with the plastocyanin family than with the azurin family (21). Although the complete sequence of Methylobacterium AM1 amicyanin (18) is only about 25% homologous with poplar plastocyanin, the concordance is greater than 50% with the residues which are totally conserved in plastocyanins (21). In contrast, there is only a 7% sequence homology between azurins and plastocyanins, indicating a much greater evolutionary divergence (21). All of the copper ligands in poplar plastocyanin are correctly located in Methylobacterium AM1 amicyanin with the expected Pro and Asn residues flanking His 47 and the expected COOH-terminal ligand set of Cys 86-X₂-His 89-Y₂-Met 92 (the corresponding ligand spacings in poplar plastocyanin are X₂ and Y₄). The NH₂-terminal sequence of P. denitrificans amicyanin through residue 54 shows a 45% homology with Methylobacterium AM1 amicyanin, and the Pro-His-Asn sequence is again preserved (20).

Although amicyanins and plastocyanins appear to have similar active site structures and similar redox potentials of 280-295 mV (15, 22) and 340-370 mV (3), respectively, they differ markedly in their physiological functions. The amicyanins of methylotrophs are periplasmic proteins that act as electron transfer mediators between methylamine dehydrogenase (an inducible enzyme) and c-type cytochromes. In contrast, the plastocyanins are chloroplast-associated proteins that are involved in electron transfer to the reaction center of photosystem I. Each of these proteins has very

low redox activity when substituted into the other system in vitro (23). Thus, the low overall sequence homology between amicyanin and plastocyanin must relate to the fact that they each interact with a different set of electron donor and acceptor proteins.

In order to verify the similarity of the active site structures of amicyanin and plastocyanin, we have undertaken a Raman spectroscopic investigation of amicyanin from P. denitrificans. Resonance Raman (RR) studies of a number of blue copper proteins have shown that excitation into the intense S \rightarrow Cu charge transfer band at ~600 nm produces strong enhancement of four to five fundamental vibrational modes in the 350- to 450- cm^{-1} region (24). The multiplicity of bands has been attributed to coupling between the Cu-S stretch and internal modes of the cysteine ligand (25, 26). The short Cu-S bond distance (<2.2 Å) present in blue copper proteins accounts for the high energies of these Cu-S-related modes (26). Furthermore, the small isotopic shift of these vibrational modes on deuterium substitution of the proteins appears to correlate with the hydrogen bonding of the cysteinate sulfur to the protein backbone (13, 27). In the high frequency range >700 cm^{-1} , the RR spectra of blue copper proteins have a rich assortment of overtones and combination bands involving the intense fundamentals in addition to a C-S stretch near 750 cm^{-1} . All of these characteristic properties have been observed in the RR spectra of P. denitrificans amicyanin, strongly supporting its classification as a novel blue copper protein.

EXPERIMENTAL PROCEDURES

Amicyanin from the facultative methylotroph Paracoccus denitrificans (ATCC 13543) was isolated and purified as described previously (17). The freeze-dried samples were dissolved in 0.01 M potassium phosphate in H₂O (pH 7.0) or in D₂O (pH meter reading 7.2). Azurin was isolated from Alcaligenes denitrificans NCTC 8582 as described previously (13). Ultrafiltration was used for concentration of the sample and its deuterium isotope exchange.

Resonance Raman spectra were obtained with a computer-interfaced Jarrell-Ash spectrophotometer (28) using a Spectra Physics 2025-11 (Kr) laser as the source of incident radiation. The detector was an RCA C31034A photomultiplier tube with an ORTEC model 9302 amplifier/discriminator. Room temperature spectra for obtaining scattering intensities relative to 0.3 M sulfate were measured on samples in capillaries using 90° scattering. For spectra at 90 K, samples in capillaries were frozen in a liquid N₂ Dewar fitted with a copper cold finger. For spectra at 15 K, 20 μl samples were pipetted directly onto the gold-plated cold finger of a closed-cycle helium Displex (Air Products). All low temperature spectra were collected in a -150° backscattering geometry. Spectra obtained at all three temperatures were qualitatively similar, but those at 15 K had the best signal-to-noise ratio and the least interference from glass (in the 400-500 cm⁻¹ region).

Samples of different isotopic composition were run consecutively under identical spectral conditions. Peak positions were determined

by abscissa expansion and curve fitting (typical values: 60% Gaussian, 40% Lorentzian, full width at half height of 7-9 cm^{-1}). Although absolute isotope shifts are accurate to only $\pm 1 \text{ cm}^{-1}$, isotope shifts are reproducible to within $\pm 0.2 \text{ cm}^{-1}$.

RESULTS AND DISCUSSION

Amicyanin from P. denitrificans has an intense absorption at 595 nm with an ϵ of $4,610 \text{ M}^{-1} \text{ cm}^{-1}$ (17), which appears to be analogous to the $\text{S}(\text{Cys})\sigma \rightarrow \text{Cu}(\text{II})$ charge transfer transition observed for other blue copper proteins (1). This assignment is confirmed by the appearance of a typical blue copper resonance Raman spectrum upon excitation within this absorption band (Fig. 1). The spectrum shows three prominent and well-resolved Raman peaks at 377, 392, and 430 cm^{-1} (peaks L, M, and O in Table I) as well as numerous weaker features. Quantitation of the intensity of the 430 cm^{-1} peak relative to ν_1 of a sulfate internal standard gives a molar scattering intensity of ~ 500 , indicating strong resonance enhancement. With the exception of the lowered intensity at 412 cm^{-1} (peak N), the spectrum of amicyanin is remarkably similar to that of azurin from A. denitrificans which has four strong peaks (L, M, N, and O) between 375 and 430 cm^{-1} (Fig. 1, inset). The RR spectrum of spinach plastocyanin actually exhibits five intense features (L, M, N, O, and P) in the 377- to 442- cm^{-1} region (Table I). However, plastocyanin resembles amicyanin in that the most intense RR feature occurs at $\sim 425 \text{ cm}^{-1}$ (peak O), whereas the dominant feature in the RR

spectrum of azurin is peak N at -410 cm^{-1} (26). Nevertheless, the close match in vibrational frequencies and general spectral intensities to those of both azurins and plastocyanin implies that amicyanin has a similar set of ligands and copper coordination geometry.

The appearance of a large number of overtone and combination bands in the $750\text{--}900\text{-cm}^{-1}$ region is another characteristic of blue copper proteins. A set of such bands is clearly visible in the RR spectrum of amicyanin (Fig. 2) and shows considerable resemblance to high frequency region of A. denitrificans azurin (Fig. 2, inset). Assignments for these observed peaks in amicyanin are given in Table II. The first intense feature at 756 cm^{-1} which corresponds to the expected frequency for 2L probably also contains a significant contribution from a fundamental vibration, the C-S stretching mode of the cysteinate ligand (Table I). The other two most intense features in both amicyanin and azurin correspond to combinations of L+O (at 807 and 809 cm^{-1} , respectively) and of M+O and/or 2N (at 820 and 824 cm^{-1} , respectively). Although less well-resolved, the high frequency region of spinach plastocyanin has had its C-S fundamental assigned at 767 cm^{-1} and potential L+O and M+O combination bands at 786 and 810 cm^{-1} , respectively (26).

Comparison of the spectroscopic data for amicyanin with those of the structurally characterized azurins and plastocyanins gives us an insight into the metal-binding site of amicyanin. Amicyanin shows an absorption maximum at 595 nm (similar to those of azurins and plastocyanins) with an extinction coefficient of $4,610\text{ M}^{-1}\text{ cm}^{-1}$,

again within the range for blue copper proteins. The appearance of a blue-copper type RR spectrum upon excitation within this absorption band strongly suggests that amicyanin has cysteine as one of its ligands and that the absorption maximum at 595 nm is due to Cys(S) \rightarrow Cu(II) charge transfer. The high energy ($> 370 \text{ cm}^{-1}$) of the resonance-enhanced fundamentals in amicyanin implies that the Cu-S(Cys) bond distance is likely to be short (i.e., $< 2.2 \text{ \AA}$ as in azurin and plastocyanin). The multiple intense peaks in the 350- to 420- cm^{-1} region are most likely due to coupling of internal ligand vibrational modes with the Cu-S stretch and imply a similarly constrained site as in azurin and plastocyanin. The similarity of the EPR parameters (17) also suggests a distorted trigonal geometry at the Cu(II) site in amicyanin. The comparison of the amino acid sequence of amicyanin from Methylobacterium AM1 (18) with that of poplar plastocyanin shows that one cysteine, two histidines, and one methionine are properly located to act as ligands for copper. Thus, the copper in amicyanins is likely to be present in a distorted trigonal planar array with one cysteine and two histidine ligands as well as a long axial methionine.

Another common attribute of the blue copper proteins is that the majority of the Raman fundamentals shift to lower energy when the protein is equilibrated in D_2O . A similar deuterium isotope dependence is observed with amicyanin. As shown in Table I, most of the vibrational modes below 500 cm^{-1} exhibit a -0.5 to -1.5 cm^{-1} shift in D_2O . These shifts are of the same magnitude as those for the azurins from Ps. aeruginosa and A. denitrificans (Table I), as

bond characteristic of blue copper sites, and help to explain the anomalous redox and spectral properties.

REFERENCES

1. Gray, H. B., and Solomon, E. I. (1981) in Copper Proteins (Spiro, T. G., ed.) Vol. 3, pp. 1-39, Wiley, New York
2. Lippin, A. G. (1980) in Metal Ions in Biological Systems (Sigel, H., ed.) Vol. 13, pp. 13-71, Marcel Dekker, New York
3. Adman, E. T. (1985) in Metalloproteins (Harrison, P., ed.) Part I, pp. 1-42, Verlag Chemie, Weinheim
4. Farver, O., and Pecht, I. (1984) in Copper Proteins and Copper Enzymes (Lontie, R., ed.) Vol. 1, pp. 183-214, CRC Press, Boca Raton
5. Norris, G. E., Anderson, B. F., and Baker, E. N. (1983) J. Mol. Biol. **165**, 501-521
6. Norris, G. E., Anderson, B. F., and Baker, E. N. (1986) J. Am. Chem. Soc. **108**, 2784-2785
7. Adman, E. T., Stenkamp, R. E., Sieker, L. C., and Jensen, L. H. (1978) J. Mol. Biol. **123**, 35-47
8. Adman, E. T., and Jensen, L. H. (1981) Isr. J. Chem. **21**, 8-12
9. Guss, J. M., and Freeman, H. C. (1983) J. Mol. Biol. **169**, 521-563
10. Garrett, T. P. J., Clingeffer, D. J., Guss, J. M., Rogers, S. J., and Freeman, H. C. (1984) J. Biol. Chem. **259**, 2822-2825
11. Church, W. B., Guss, J. M., Potter, J. J., and Freeman, H. C. (1986) J. Biol. Chem. **261**, 234-237
12. Penfield, K. W., Gay, R. R., Himmelwright, R. S., Eickman, N.

- C., Norris, V. A., Freeman, H. C., and Solomon, E. I. (1981) J. Am. Chem. Soc. 103, 4382-4388
13. Ainscough, E. W., Bingham, A. G., Brodie, A. M., Ellis, W. R., Gray, H. B., Loehr, T. M., Plowman, J. E., Norris, G. E., and Baker, E. N. (1987) Biochemistry 26, 271-282
 14. Tobari, J., and Harada, Y. (1981) Biochem. Biophys. Res. Commun. 101, 502-508
 15. Tobari, J. (1984) in Microbial Growth on C₁ Compounds (Crawford, R. L., and Hanson, R. S., eds.) pp. 106-112, American Society for Microbiology, Washington, DC
 16. Lawton, S. A., and Anthony, C. (1985) Biochem. J. 228, 719-726
 17. Husain, M., and Davidson, V. L. (1985) J. Biol. Chem. 260, 14626-14629
 18. Ambler, R. P., and Tobari, J. (1985) Biochem. J. 232, 451-457
 19. Husain, M., Davidson, V. L., and Smith, A. J. (1986) Biochemistry 25, 2431-2436
 20. Husain, M., Davidson, V. L., and Smith, A. J., unpublished results
 21. Rydén, L. (1984) in Copper Proteins and Copper Enzymes (Lontie, R., ed.) Vol. 1, pp 157-182, CRC Press, Boca Raton, FL
 22. Gray, K. A., Knaff, D. B., Husain, M., and Davidson, V. L. (1986) FEBS Lett. 207, 239-242
 23. Davidson, V. L., Husain, M., and Malkin, R. unpublished results
 24. Woodruff, W. H., Dyer, R. B., and Schoonover, J. R. (1988) in Biological Applications of Raman Spectroscopy (Spiro, T. G., ed.) Vol III, pp 413-438, John Wiley, New York

25. Nestor, L., Larrabee, J. A., Woolery, G., Reinhammar, B., and Spiro, T. G. (1984) Biochemistry 23, 1084-1093
26. Blair, D. F., Campbell, G. W., Schoonover, J. R., Chan, S. I., Gray, H. B., Malmstrom, B. G., Pecht, I., Swanson, B. I., Woodruff, W. H., Cho, W. K., English, A. M., Fry, H. A., Lumm, V., and Norton, K. A. (1985) J. Am. Chem. Soc. 107, 5755-5766
27. Mino, Y., Loehr, T. M., Wada, K., Matsubara, H., and Sanders-Loehr, J. (1987) Biochemistry, 26, 8059-8065
28. Loehr, T. M., Keyes, W. E., and Pincus, P. A. (1979) Anal. Biochem. 96, 456-463
29. Maret, W., Shiemke, A. K., Wheeler, W. D., Loehr, T. M., and Sanders-Loehr, J. (1986) J. Am. Chem. Soc. 108, 6351-6359
30. Baker, E. N., personal communication

Table I
Resonance Raman Vibrational Frequencies for
Azurins, Plastocyanin, and Amicyanin^a

Peak	<u>Ps. aeruginosa</u> azurin ^b		<u>A. denitrificans</u> azurin ^c		<u>P. denitrificans</u> amicyanin ^d		<u>Spinach</u> plastocyanin ^e
	freq.	shift in D ₂ O	freq.	shift in D ₂ O	freq.	shift in D ₂ O	
A	116(w)		112(w)				
B	138(vvw)						
C	165(vvw)						
D	188(w)		184(w)				
E	199(vw)						
F	222(w)				245(w)		
G	266.1(w)		255(w,br)	0	264(m,br)	-1.0	
H	286.7(m)	-5	282(w,br)	0	283.5(w)	-0.8	270.1(m)
I	308(w)		g		g		320(w)
J	333(vw)		336(vw)	-1	330.8(w)	-0.7	328(w)
			350(w)	-2	345(w)	-1.0	343.1(w)
K	348.2(w)	-2	363(w)	-3	358(w)		
L	372.6(s)	-0.9	375(s)	-0.4	376.6(s)	-0.3	377.3(s)
M	400.5(m)		397.9(s)	0	391.9(s)	-0.8	387(m)
N	408.6(vs)	-1.0	411.2(vs)	-1.0	412.0(w)	-2.5	406.7(m)
O	427.9(s)	-1.2	429.4(s)	-0.4	429.6(vs)	-0.8	425.3(vs)
P	441(w)	-1.5	444.2(m)	0	449(w)	-1.2	441.5(m)
Q	454.6(w)	-0.6 ^f	459(m)	-1.4	462(w)	-1.3	
R	474(w)	-1.0			481.6	-1.5	480(w)
S	492(w)	+1.3					491(w)
T	569(vvw)	-2	565(vw)				
U	657.2(w)						

Table I, continued:

Peak	<u>Ps. aeruginosa</u>		<u>A. denitrificans</u>		<u>P. denitrificans</u>		<u>Spinach</u>
	azurin ^b		azurin ^c		amicyanin ^d		plastocyanin ^e
	freq.	shift in D ₂ O	freq.	shift in D ₂ O	freq.	shift in D ₂ O	
V	678(vw)						
W	753.2(m)		756(m,br)		756(m)		767(m)
X	932(vvw)		937(vw)		934(vw)		
Y	975(vvw)				970(vw)		

^a Frequencies and isotope shifts in cm^{-1} ; w, weak; m, medium; s, strong; br, broad; v, very.

^b Frequencies (12 K) and isotope shifts (25 K) from reference 25.

^c Frequencies and isotope shifts (90 K) from reference 13.

^d This work, at 15 K.

^e Frequencies (12 K) from reference 25.

^f At 300 K.

^g Frozen solutions exhibit an ice mode at 308 cm^{-1} , which shifts 11 cm^{-1} in D₂O.

Table II
 Overtone and Combination Bands (in cm^{-1}) in the Resonance
 Raman Spectrum of P. denitrificans Amicyanin

Fundamentals		Overtones and Combinations		
		Observed	Assignment	Predicted
L	377	756	2 L	754
M	392	768	L + M	769
N	412	783	2 M	784
O	430	807	L + O M + N	807 804
P	449			
Q	462	820	M + O 2 N	822 824
R	482		L + Q	839
		842	M + P N + O	841 842
		859	L + R 2 O	859 860
		894	2 P	898
		911	P + Q	911

FIGURE LEGENDS

FIG 1. Resonance Raman spectrum of P. denitrificans amicyanin in the low frequency region. Sample concentration ~2 mM protein in 0.01 M potassium phosphate buffer (pH 7.2). Spectrum was obtained at 15 K with 647.1-nm excitation (150 mW), $0.5\text{-cm}^{-1}\text{s}^{-1}$ scan rate, 4-cm^{-1} resolution, and represents the accumulation of 16 scans. S denotes peaks from frozen solvent (translational modes of ice) and L denotes a laser plasma line. INSET: Resonance Raman spectrum of A. denitrificans azurin (13). Sample concentration ~2 mM protein in 0.05 M phosphate buffer (pH 6.5). Spectrum was obtained at 90 K with 647.1-nm excitation (160 mW at the sample Dewar), resolution of 4 cm^{-1} , scan rate of $0.5\text{ cm}^{-1}\text{ s}^{-1}$ and represents the accumulation of 25 scans.

FIG 2. Resonance Raman spectra of P. denitrificans amicyanin in the overtone and combination band region. Sample conditions same as in Fig. 1. INSET: Resonance Raman spectrum of A. denitrificans azurin (13). Sample conditions same as in Figure 1, inset, except that the data were subjected to a 25-point smooth.

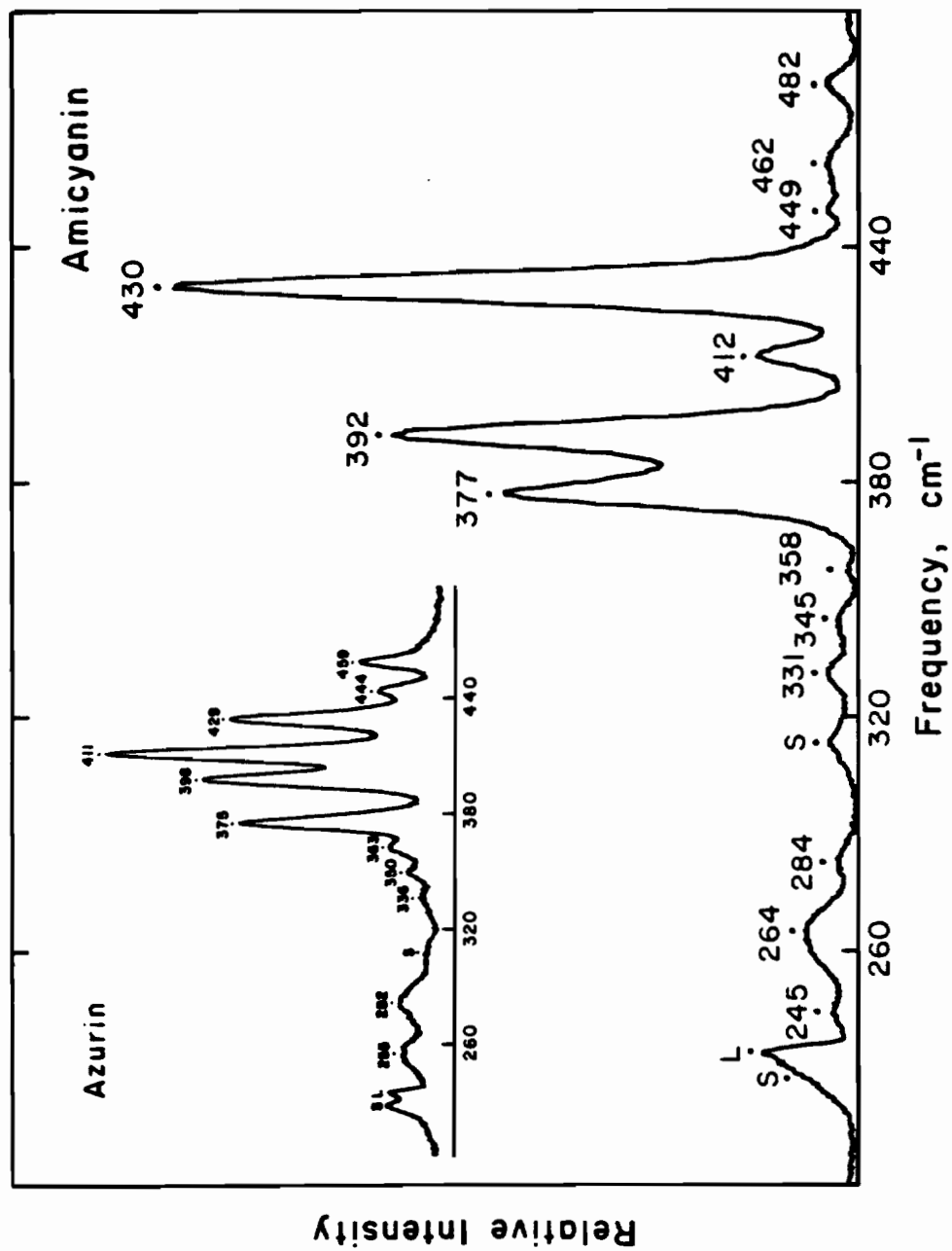


FIGURE 1

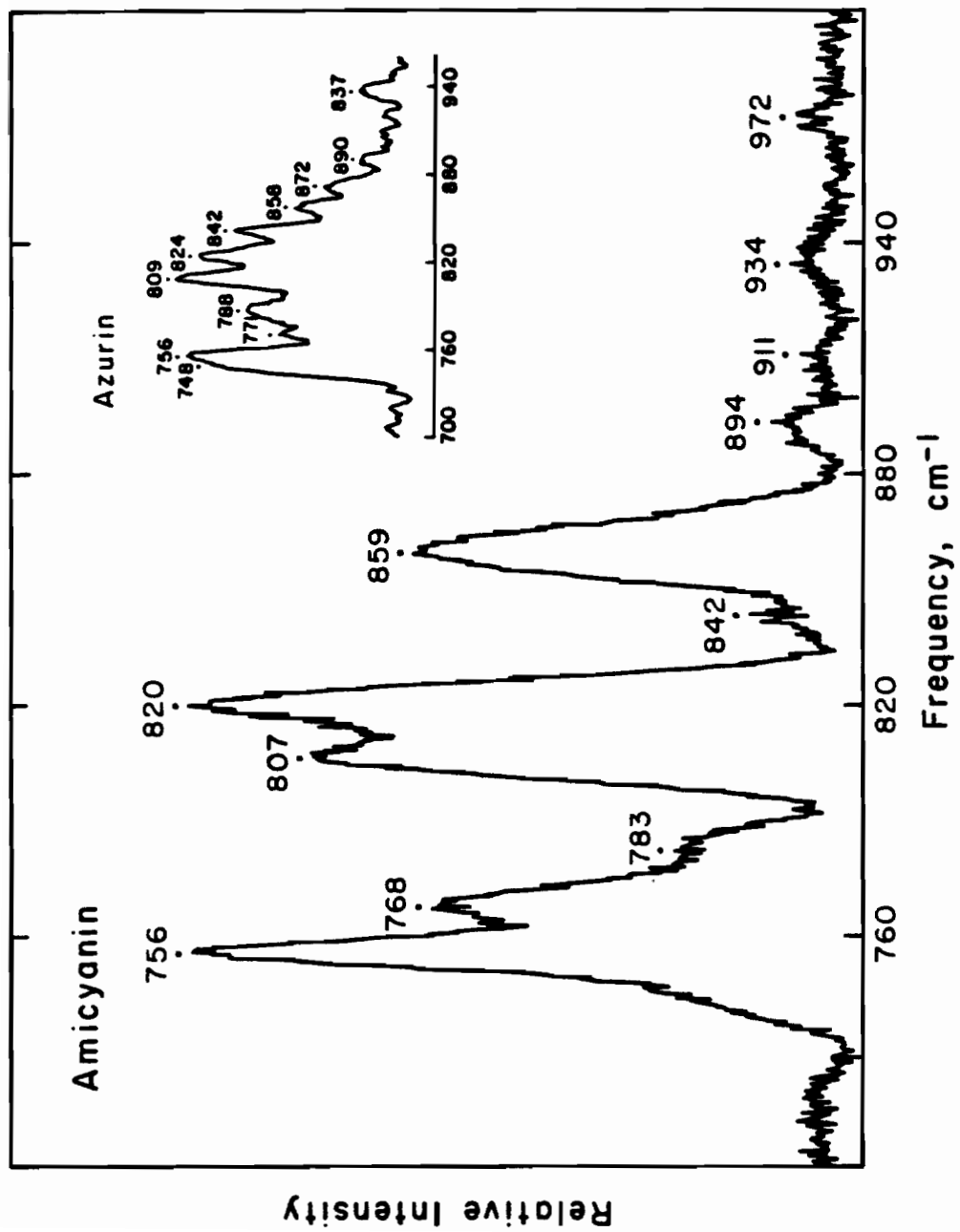


FIGURE 2

CHAPTER IV

RESONANCE RAMAN SPECTROSCOPY OF OXYHEMOCYANIN.

ISOTOPE EFFECTS DUE TO SOLVENT HYDROGEN AND OXYGEN

INTRODUCTION

It is well established that a number of copper proteins and enzymes such as hemocyanin, tyrosinase, and laccase contain antiferromagnetically coupled binuclear copper centers (1). These proteins have unusual spectroscopic properties and they react with dioxygen under physiological conditions. Among these binuclear copper proteins hemocyanins and tyrosinases have been extensively studied using chemical and spectroscopic methods (1-4). However, the detailed nature of the copper binding sites in these proteins is still not clearly understood.

Hemocyanin (Hc) is a high molecular weight respiratory protein found in the hemolymph of invertebrates in the arthropod and mollusc phyla (5, 6). It is oligomeric and each subunit binds one oxygen molecule per two copper atoms. The size of the polypeptide chain differs between the two phyla. Arthropod Hc is made up of oxygen binding units of 75,000 Daltons whereas mollusc Hc is composed of subunits of 50,000 Daltons. Deoxyhemocyanin is colorless and contains two Cu(I) which bind dioxygen to give rise to the blue-

colored oxy form. Oxyhemocyanin is characterized by intense absorption maxima near 345 nm ($\epsilon = 20,000 \text{ M}^{-1} \text{ cm}^{-1}$ per 2 Cu) and 570 nm ($\epsilon = 1,000 \text{ M}^{-1} \text{ cm}^{-1}$ per 2 Cu) as well as a positive feature at ~480 nm in its circular dichroism spectrum (6, 7).

Hemocyanin exhibits unique magnetic susceptibility and EPR properties (8, 9). Both deoxy and oxyHc are EPR silent. For deoxyHc this originates from the inherent diamagnetism due to a filled d-shell for Cu(I), while for oxyHc this is due to the antiferromagnetic coupling of the free d electron on each of the two Cu(II) ions, resulting in a $-J > 550 \text{ cm}^{-1}$ (8). Furthermore, the met form of Hc has also been found to be EPR silent (9). The EPR measurements and the strong antiferromagnetic interaction suggest the existence of either a protein donated endogenous bridge or a solvent-derived exogenous bridge between the two copper atoms of hemocyanin. Evidence for protein tyrosine groups as a candidate was presented (9) but was ruled out by the x-ray crystal structure (10). EPR measurements on a single-peroxo-bridged dicopper complex (11a), a model for oxyHc, showed the complex to be EPR silent. This suggested that a peroxo bridge alone can be responsible for the strong antiferromagnetic coupling in the model and hence in oxyHc. However, this cannot explain the antiferromagnetic coupling in metHc which lacks the peroxo bridge. Furthermore, binuclear copper complexes with a single hydroxo group have been shown to exhibit strong antiferromagnetic coupling (11b).

X-ray crystallographic measurements on deoxyHc from the arthropod, Panulirus interruptus, showed that the two copper ions are

ligated to three histidines each (Fig. 1A), and each of the six histidines is conserved among arthropod hemocyanins (10, 12). However, only three of these six histidines are conserved for hemocyanins from molluscs (e.g., Helix pomatia) (12c). Whether or not there is a non-protein bridging ligand between the two coppers in deoxyhemocyanin is uncertain at the present crystallographic resolution of 3.2 Å. EXAFS measurements of different deoxyhemocyanins have established the Cu-Cu distance to be ~3.4 Å (13-15), which is similar to the Cu-Cu distance in the crystal structure of deoxyHc. It is presumed that the histidine ligands remain bound to copper in the oxy form, but the site may undergo a change in coordination geometry in the presence of O₂.

Resonance Raman (RR) spectroscopy has provided further structural details on the active site in oxyHc (4). It has demonstrated that molecular O₂ is bound as a peroxide ion, as is evidenced by the observation of a peroxide-like O-O vibration at 750 cm⁻¹ and its isotopic shift to 708 cm⁻¹ with ¹⁸O₂ (16). Furthermore, RR studies using ¹⁶O¹⁸O showed that the two oxygen atoms are equivalent and, therefore, must be bound to the two Cu atoms in a μ-peroxo fashion (17). The low energy of this peroxide mode may be attributed either to the hydrophobic environment or to hydrogen bonding interactions between the peroxide oxygens and hydrogen donor groups in the protein.

The O-O stretch at ~750 cm⁻¹ in oxyhemocyanin is strongly enhanced with the visible excitation and, hence, the absorption band at 570 nm can be assigned to O₂²⁻ → Cu(II) charge transfer (CT) (16).

The near-UV band at 345 nm has been suggested to arise either from peroxide \rightarrow Cu(II) CT (18) or from a simultaneous pair excitation (19) as is seen in coupled cupric dimeric compounds (20, 21). Excitation within the near-UV band leads to the appearance of a number of new RR features between 150-350 cm^{-1} (16, 19, 22). Based on ^{65}Cu and D_2O isotopic substitution, many of these are assigned as vibrational modes of the Cu(II)-coordinated histidines (19, 22). These assignments are supported by the vibrational spectra of model Cu(II)-imidazole complexes (23).

The above-mentioned structural and spectroscopic data have been combined to arrive at a model for the binuclear copper site in deoxy and oxyhemocyanins (Fig. 1B). The presence of a bridging hydroxo group, at least in the oxy form, is inferred from the strong coupling of the Cu(II) ions and the apparent absence of a bridging group from the protein. In an attempt to obtain more definitive evidence for the presence of a hydroxo bridge, we decided to compare the RR spectra of oxyHC in H_2O , H_2^{18}O and D_2O . We primarily investigated the RR spectra in the 100-600 cm^{-1} region because $\delta(\text{Im-Cu-O})$ and $\nu(\text{Cu-OH})$ are expected to occur at frequencies of 100-300 cm^{-1} and 400-600 cm^{-1} , respectively. Both vibrations should exhibit substantial shifts of -5 to -20 cm^{-1} , respectively, with ^{18}O in place of ^{16}O and somewhat smaller shifts to lower energy with D in place of H. If neither vibration could be detected due to lack of resonance enhancement, there is still the possibility that imidazole ligands trans to a Cu-OH moiety would show some $\nu(\text{Cu-O})$ character coupled with their resonance-enhanced $\nu(\text{Cu-imidazole})$ modes. The latter

might be detected as 3-5 cm^{-1} shifts to lower energy in ^{18}O , similar to what has been observed for the $\nu(\text{Fe-N}_{\text{trans}})$ in Fe-O-Fe-containing proteins and model compounds (25, 26). In addition, we checked the deuterium isotope dependence of the peroxide vibrational mode at $\sim 750 \text{ cm}^{-1}$ in order to learn if the oxygens of the coordinated peroxide are hydrogen bonded to suitable hydrogen-donor amino acid residues or water molecules in the vicinity of the dioxygen binding site.

EXPERIMENTAL PROCEDURES

Protein preparation. Hemocyanin was prepared from the mollusc, Busycotypus canaliculatum. Specimens of B. canaliculatum were obtained from the Marine Biological Laboratory, Woods Hole, Massachusetts. The specimens arrived packed in a box containing seawater-soaked straw. Hemolymph was obtained following the method from (16). The specimens were rinsed with 0.54 M NaCl (physiological concentration) and dried with Kimwipes. They were then held over a clean beaker in ice. The animal was restrained from retracting its foot by inserting a spatula on the right side between the foot muscles and the horny outer surface of the foot (Fig. 2). A number of holes were made on the left side of the foot with a syringe needle and the foot was squeezed. At first transparent liquid flowed out which was discarded. Finally blue-colored hemolymph oozed out which was drawn off with a Pasteur pipette and passed through a funnel containing glass wool to remove clotted protein. The volume obtained

varied from animal to animal and ranged from 1 mL to 5 mL (according to Dr. Joann Sanders-Loehr, previous preparations gave ~30 mL per animal, but we could not get that good a yield). The total yield of hemolymph from one dozen animals was ~42 mL.

The hemolymph was transferred to 15 mL centrifuge tubes kept on ice and was centrifuged in a Sorvall centrifuge for 10 minutes at 10,000 rpm. (12,000 x g in an SS-34 rotor) to remove cell membranes and other insoluble material. The supernatant was collected and stored overnight in the refrigerator. Additional clotted blood was seen the next morning, and it was removed by centrifugation for 15 minutes at 7,000 rpm. The supernatant was filtered through a 0.45 μm Millipore filter (with a glass fiber pre-filter) and then sterilized by passage through sterile 0.45 μm Millipore filters and the sample collected in a sterile bottle, and stored in the refrigerator (short term) or at -15°C freezer (long term). The sample integrity based on optical and Raman spectra was maintained well in the frozen samples. If samples are to be stored only in the freezer, the Millipore filtration steps can be omitted.

At pH values below ~8.5, hemocyanin from B. canaliculatum exists as high molecular weight, 100S aggregates (27a) resulting in a turbid solution. This creates a problem for obtaining a Raman spectrum because it produces a high background signal. Although the sample can be concentrated by pelleting in an ultracentrifuge (with ~50% yield), it is too viscous to be concentrated by ultrafiltration. These problems were alleviated by exhaustively dialyzing hemocyanin at pH 9.8 with carbonate buffer which resulted in an optically

transparent solution due to dissociation into subunits of 15S to 60S (27a). This sample was readily concentrated by centrifugation through an ultrafiltration membrane (~100% yield).

Isotope exchange: D₂O. A protein concentration of about 1.4 mM in Cu was determined using the molar absorptivity of $\epsilon = 10,000 \text{ M}^{-1} \text{ cm}^{-1}$ per Cu for oxyhemocyanin (27b). Two 5.0 mL aliquots were placed in ultracentrifuge tubes (Beckman #355603, 10.4 mL capacity) and centrifuged in a 70.1 Ti rotor at ~50,000 rpm for 40 minutes at -10°C using a Beckman Model L5-65 ultracentrifuge. For each aliquot three separate layers were obtained. The upper layer was colorless, the middle one blue and the bottom layer a dark blue pellet. The layers were separated very gently and quickly and the volumes of the two liquid layers were measured. The pellets (0.1 mL each) were dissolved in ~500 μL carbonate buffers (H₂O and D₂O buffers, 0.05 M, pH 9.82 and pH reading of 9.84, respectively) by adding buffer dropwise and stirring each with a glass rod. Some whitish precipitate remained. After dissolution of the pellets, the volumes were made up to 5.0 mL each with the corresponding buffer.

The D₂O buffer was prepared by making up separate 1 M solutions of NaHCO₃ and anhydrous Na₂CO₃ in D₂O (99.8% deuterium, Aldrich Chemical Company). Then 110 μL of 1M NaHCO₃ was mixed with 140 μL of 1M Na₂CO₃ to give a pH reading of 9.8 in a final volume of 5 mL with a concentration of 0.05 M. The concentration of D₂O in the resulting hemocyanin sample was estimated to be 98%.

Hemocyanin solutions were cycled through the deoxy state prior to isotope replacement. The reason for this was that a bridging hydroxo group should be more loosely coordinated and, thus, more susceptible to exchange with solvent OH^- ions in the Cu(I) form of the protein. The D_2O sample was made anaerobic as shown in Figure 3. Argon gas (saturated with D_2O to keep the sample from dehydrating) was passed over the surface of the sample in a serum bottle. During this treatment the sample was stirred with two small magnetic stirrer bars until the blue color of the solution faded. This took ~6 hours and the solution changed to a whitish-blue color indicating that ~50% of the protein was in the deoxy state. Then both the H_2O and D_2O samples (reoxygenated) were transferred to two separate centrifuge tubes and were centrifuged for ~10 minutes at 10,000 rpm (12,000 x g in an SS-34 rotor). The supernatants were collected separately and saved overnight in the refrigerator.

The supernatants were ultracentrifuged for 2.0 hours at 50,000 rpm in a 70.1 Ti rotor. The two layers that were obtained were separated and their volumes measured. The volumes of the supernatants were 4.8 mL each, so the pellets were 0.2 mL each. Each pellet was dissolved in 100 μL of the corresponding H_2O and D_2O carbonate buffers (.05 M, pH ~9.8) without using a stirring rod. Since the pellets were slow to dissolve, they were left overnight in tilted test tubes so that the pellets were totally immersed in buffer at all times. The next morning the pellets were found to be dissolved and had a hemocyanin concentration of 8 mM in copper. Approximately 55% of the initial hemocyanin was present in the final

samples. Two 20 μL samples of each were used for Raman experiments. The remainder of the samples was left in the refrigerator for about five days after which they were stored in the freezer. Raman spectra of deuterium-exchanged samples showed a -6 cm^{-1} shift of the 234 cm^{-1} ice mode. This is typical of the behavior of D_2O at 15 K, and, thus, indicates $> 80\%$ deuterium substitution.

Isotope exchange: H_2^{18}O . About 1.5 mL of the hemolymph which had been stored frozen was pipetted into a dialysis bag. The sample was dialyzed against 450 mL of 0.2 M carbonate buffer, pH 9.8 for about 20 hours with one exchange of buffer in a 5°C cold room. The dialyzed sample, which had a clear blue color, was left overnight in the refrigerator.

Two 400 μL aliquots were concentrated by centrifugation in a Centricon 30 concentrator (Amicon) to obtain a final volume of 70 μL . The Centricon volume was calibrated by comparison with a Centricon containing a known volume of 70 μL and marking its meniscus on the tube tilted at $\sim 30^\circ$ angle. Then one of the samples was diluted with 300 μL of H_2O and the other with 300 μL of H_2^{18}O (97% ^{18}O , YEDA Research and Development Co. Ltd., Israel) both containing 0.2 M carbonate buffer, pH 9.8. Both the buffers were prepared by dissolving 10.4 mg of NaHCO_3 and 8.6 mg of Na_2CO_3 in 1 mL of respective H_2O or H_2^{18}O to give a pH of 9.8 and a concentration of 0.2 M in each solution.

Each of the hemocyanin samples was transferred to a serum bottle fitted with a rubber septum and connected through a two-way stopcock

to a CO gas cylinder in a hood. Each sample was then placed on ice and flushed with CO gas (H_2O saturated by passage through 0.2 mL of H_2O or H_2^{18}O carbonate buffer) for 10 minutes while shaking the serum bottle gently. Then the sample was incubated for 5 minutes. The above processes were repeated twice until the sample became colorless. The reason for converting oxyHc to the CO derivative of deoxyHc was to facilitate exchange of a bridging OH group. Both the samples were stored in the hood overnight to allow time for ^{18}O exchange. The samples were then exposed to air for 6 hours to allow the CO to be replaced by O_2 (6). The optical spectra of both the samples were taken to check the extent of reoxygenation and they were found to be nearly 100% reoxygenated. Finally, the samples were concentrated using a Centricon 30 to give a final volume of $\sim 70 \mu\text{L}$ and had a hemocyanin concentration of 6.6 mM and 4.7 mM in Cu for the H_2O and H_2^{18}O samples, respectively, and an ^{18}O content of 63% for the H_2^{18}O sample based on mass spectrometry (Fig. 4) of the Centricon filtrate.

The presence of only 63% ^{18}O in the hemocyanin buffer was considerably smaller than the value of 93% expected from the known dilution of the original 97% ^{18}O solvent. While carrying out the isotopic exchange with H_2^{18}O buffer, there were steps in which H_2O from the air could get into the sample, thereby diluting it and making the isotopic exchange less effective. Water from air might have condensed on the inside wall of the container when the sample stored in the refrigerator or on ice was opened, causing a dilution of the sample. To minimize the condensation of water from air inside

the container, the samples should first be brought to room temperature before opening. In subsequent experiments, sample containers were kept sealed, including the ultrafiltration device. Samples were placed in small containers to minimize the volume of air space. When freezing the samples, the containers were wrapped with parafilm to avoid water from the freezer getting into the samples.

A second isotope exchange experiment was performed taking the above precautions for both the H_2O and H_2^{18}O hemocyanin samples. In addition, the CO derivatives were reoxygenated by bubbling with O_2 gas for 12 minutes, instead of exposing the samples to air. On taking the mass spectra of the original H_2^{18}O buffer as well as the H_2^{18}O Centricon filtrate, it was found that the percentage of ^{18}O in pure carbonate buffer was 92% (compared to 97% in original H_2^{18}O) and that of ^{18}O in Centricon filtrate was 80% (compared to an expected value of 87% based on ^{18}O in the buffer).

Instrumentation. Electronic absorption spectra were obtained on a Lambda 9 Perkin-Elmer spectrophotometer at room temperature. A computer-interfaced Jarrell-Ash spectrophotometer (28) was used to obtain the Raman spectra. Excitation was provided by Spectra Physics 164-05 (Ar) or Coherent Innova 90 (Ar) ion lasers. The detector was an RCA C31034A photomultiplier tube at -25°C with an ORTEC model 9302 amplifier/discriminator. Resonance Raman spectra of hemocyanin were obtained on samples at 278 K, 90 K and 15 K in a 150° backscattering geometry. Samples were placed in melting-point capillaries and inserted into the copper cold finger of a Dewar cooled with an ice-

water slurry (~278 K) or liquid nitrogen (~90 K). The indicated temperatures are measured values, determined with an iron-constantan thermocouple in a glass capillary placed in the copper rod. A closed-cycle helium Displex (Air Products) was used for samples at 15 K. Samples were pipetted onto the gold-plated cold finger of the Displex (Fig. 5). Other conditions used were a slit-width of 6 cm^{-1} , scan rate of $0.5\text{--}1.0 \text{ cm}^{-1} \text{ s}^{-1}$ and a laser power of 10–15 mW in the UV or 100 mW in the visible, measured at the sample after passing through a filter monochromator (Applied Photophysics). Typically, two sets of spectra were collected in 8–10 multiple scans each and then averaged together if they showed good agreement.

To obtain RR spectra of samples with different isotopic compositions the samples were run consecutively under identical spectral conditions. Frequencies were corrected using an indene standard (29) for $500\text{--}800 \text{ cm}^{-1}$ region and laser plasma lines at 117 and 138 cm^{-1} for $50\text{--}400 \text{ cm}^{-1}$ region. Absolute frequencies are accurate to $\pm 1 \text{ cm}^{-1}$; relative frequencies for isotope comparisons are accurate to $\pm 0.5 \text{ cm}^{-1}$. Typical sample concentrations were 1.5 mM in Cu for experiments at 278 and 90 K and 6.5 mM to 8 mM for experiments at 15 K. Sample integrity was monitored by obtaining electronic absorption spectra before and after Raman studies. At low temperature no degradation was observed but prolonged exposure of the sample to UV laser light at 278 K caused it to denature to some extent, as was also evident by the decolorization of the sample at the spot where it was hit by the laser.

Mass spectra of the Centricon filtrate of the H_2^{18}O samples were obtained on a VG Analytical 7070E mass spectrometer operated with electron impact ionization at 70 eV.

RESULTS AND DISCUSSION

Copper-Peroxide Vibrational Modes. Oxyhemocyanin from B. canaliculatum has absorption bands in the UV/visible region at 345 and 565 nm (Fig. 6). The absorption at 565 nm with an extinction coefficient of $500 \text{ M}^{-1} \text{ cm}^{-1} \text{ Cu}^{-1}$ has been assigned as an $\text{O}_2^{2-} \rightarrow \text{Cu(II)}$ CT band (16). The intense absorption at 345 nm has been assigned as another peroxide to Cu(II) CT or to a simultaneous pair excitation (18, 19). Resonance Raman spectra obtained with excitation into the 565 nm absorption band show an intense peak at 747 cm^{-1} and weaker spectral features at 420 and 550 cm^{-1} (Fig. 7). The spectral feature at 747 cm^{-1} has been assigned to the peroxide O-O stretching vibration on the basis of its isotopic shift with $^{18}\text{O}_2$ (16). The peaks at ~ 234 and $\sim 315 \text{ cm}^{-1}$ are ice lattice modes (30). The peaks at 420 and 550 cm^{-1} have not been previously assigned, although the latter has been suggested to be $\nu(\text{Cu-O}_2)$ of the bound peroxide (31).

Our immediate interest was to determine if the bound peroxide showed evidence of hydrogen bonding. When the protein was equilibrated in D_2O , no spectral shift of $\nu(\text{O-O})$ at 747 cm^{-1} (Fig. 8) or $\nu(\text{Cu-O}_2)$ at 550 cm^{-1} was observed. A shift of 0.5 cm^{-1} or more would have been readily detected under these conditions. The lack of a deuterium isotope effect on either of the peroxide-related

vibrational modes implies that the peroxide oxygens which are thought to bridge the binuclear copper site are not hydrogen bonded either to the protein or to any water molecule in the oxygen binding pocket. These results are consistent with the X-ray crystal structure on P. interruptus hemocyanin which shows that hemocyanin has mainly hydrophobic amino acid residues, particularly in the vicinity of the histidine ligands and the oxygen binding site (10). The present data are also consistent with the failure to observe any deuterium isotope effect on the kinetics of O₂ binding by P. interruptus hemocyanin (32). Thus, the proposal that one of the histidine ligands might be hydrogen bonded to the coordinated peroxide and thereby trigger cooperative oxygen binding (24), does not seem very likely for either arthropod or molluscan hemocyanin.

The iron-containing respiratory proteins hemoglobin and hemerythrin represent an interesting contrast to hemocyanin. They are similar to hemocyanin in providing a non-polar environment at the oxygen-reactive metal site, but differ in that the dioxygen in each case is coordinated to only a single iron atom. The resulting superoxide species in oxymyoglobin is stabilized by hydrogen bonding to the distal histidine (33), while the peroxide species in oxyhemerythrin appears to be protonated and hydrogen bonded to the Fe-O-Fe moiety (34, 35). These proton-dependent interactions result in deuterium isotope shifts of +5 cm⁻¹ for the 1122 cm⁻¹ $\nu(\text{O-O})$ of Co(II)-substituted oxyhemoglobin, +4 cm⁻¹ for the 844 cm⁻¹ $\nu(\text{O-O})$ of oxyhemerythrin, and +4 cm⁻¹ for the 496 cm⁻¹ $\nu(\text{Fe-O-Fe})$ of oxyhemerythrin (36).

Equilibration of deoxyhemocyanin with H_2^{18}O , followed by conversion to oxyhemocyanin in H_2^{18}O had no observable effect on either the O-O vibration at 747 cm^{-1} (data not shown) or the Cu-O₂ vibration at 550 cm^{-1} (Fig. 9). Since the bridging oxo group in oxyhemerythrin has been found to exchange with solvent oxygen upon a 10- to 20-hour incubation in the deoxy state (25), it is likely that a bridging hydroxo group in deoxyhemocyanin would have exchanged during the 6- to 10-hour incubation in the CO-bound deoxy state. The lack of a solvent ^{18}O dependence indicates that $\nu(\text{O-O})$ and the probably $\nu(\text{Cu-O}_2)$ are pure modes of vibration which are not significantly coupled with the vibrations of a putative Cu-OH-Cu moiety.

The broad peak at 550 cm^{-1} has been assigned as $\nu(\text{Cu-O}_2)$ on the basis of its loss of intensity with $^{18}\text{O}_2$ (31). The frequency of 550 cm^{-1} is also within the expected range for an M-O₂ vibration. The corresponding values for $\nu(\text{Fe-O}_2)$ in oxyhemoglobin and oxyhemerythrin are 567 and 503 cm^{-1} , respectively (36). It is surprising that $\nu(\text{Cu-O}_2)$ is more enhanced than $\nu(\text{O-O})$ with UV excitation, whereas $\nu(\text{Cu-O}_2)$ has much less intensity than $\nu(\text{O-O})$ with visible excitation (Fig. 7). The behavior of $\nu(\text{Cu-O}_2)$ lends support to the assignment of the 345 nm absorption as an additional $\text{O}_2^{2-} \rightarrow \text{Cu(II)}$ CT band. The lower energy π^*_A peroxide orbital responsible for this electronic transition has been suggested to have better overlap with the Cu orbitals, thereby explaining the greater intensity of the 345 nm absorption (18). This superior orbital overlap would also be expected to produce greater resonance

enhancement of the Cu-O₂ vibrational mode with UV excitation, as has been observed in the present experiments.

Copper-Ligand Vibrational Modes. We also explored the Raman spectrum of hemocyanin in the low frequency region of 50-400 cm⁻¹ using 363.8 nm excitation. Six sample peaks were observed in this region at 174, 230, 269, 292, 313, and ~345 cm⁻¹ (Fig. 10). The peaks at 117, 132, and 138 cm⁻¹ are plasma lines which are notable in the absence of a filter monochromator (Fig. 10A) and were still not completely removed with a filter monochromator. The six low frequency sample modes have been reported previously; those at 230, 269, 292, and 313 cm⁻¹ being sensitive to the mass of the copper and those at 230, 269, and 313 cm⁻¹ undergoing shifts in D₂O (22, 31). We observed a similar deuterium isotope sensitivity to that reported previously for oxyhemocyanin in D₂O (Table I). On the basis of their combined Cu and hydrogen isotope dependence, the peaks at 230, 269, and 313 cm⁻¹ have been assigned to Cu-imidazole vibrations, whereas the Cu-dependent peak at 292 cm⁻¹ has been suggested as a Cu-X vibration with X as the putative bridging ligand (22).

Examination of oxyhemocyanin in H₂¹⁸O failed to reveal an oxygen isotope dependence in any of the low frequency protein modes (Fig. 10). The only peak which shows a broadening and partial shift to lower energy in H₂¹⁸O is the peak at 230 cm⁻¹. This peak is in the same location as an ice mode observed with visible excitation (Fig. 7) which typically shifts 6-8 cm⁻¹ to lower energy in D₂O or H₂¹⁸O buffer controls. However, with 363.8 nm excitation the considerably

greater resonance enhancement of the sample peaks normally obscures the contribution of the ice mode. Thus, the relative intensity of the 230 cm^{-1} peak and the 1 cm^{-1} shift to lower energy in D_2O (Table I) is maintained in liquid samples which have no contribution from an ice mode (22). We attribute the ^{18}O -dependence of the 230 cm^{-1} to the successive aging of the sample between the time the spectra in Figure 10A and Figure 10B were obtained, which resulted in decreased enhancement of the protein modes relative to the ice mode. The D_2O sample was considerably fresher and showed no apparent decrease in intensity at 230 cm^{-1} . The failure of the 292 cm^{-1} peak to shift to lower energy in H_2^{18}O indicates that it cannot be assigned to the vibration of a bridging hydroxide. Similarly, the lack of ^{18}O -dependence for the 269- and 313-cm^{-1} peaks implies that these are pure $\nu(\text{Cu-Im})$ with no observable coupling to $\nu(\text{Cu-OH})$ of a bridging hydroxide.

CONCLUSIONS

Our RR data on hemocyanin from B. canaliculatum demonstrated that all of the vibrational modes which have been assigned to Cu-imidazole vibrations are perturbed by deuterium substitution, but are insensitive to H_2^{18}O substitution. This implies that these modes are pure stretching modes which do not involve coupling to the vibrations of other ligands. Furthermore, none of the other vibrational modes including $\nu(\text{O-O})$ and $\nu(\text{Cu-O}_2)$ showed any shift to lower energy at H_2^{18}O . Even if one cannot observe $\nu(\text{Cu-OH})$ from a bridging hydroxide

group, one might have observed it coupling with $\nu(\text{Cu-Im})$ or $\nu(\text{Cu-O}_2)$ to give rise to a frequency shift of 1 cm^{-1} or more to lower energy.

Plausible explanations for the above observations are that (i) there is no hydroxo bridge; (ii) if there is a hydroxo bridge, it is non-chromophoric with 345 or 565 nm absorption; (iii) that $\nu(\text{Cu-Im})$ and $\nu(\text{Cu-O}_2)$ are pure vibrational modes which do not couple with any other modes; or (iv) that the bridging hydroxide did not exchange under our conditions. Thus, although we did not observe any vibrational mode due to the bridging ligand, we cannot rule out its presence on the basis of RR spectral data only.

The peak at 550 cm^{-1} due to $\nu(\text{Cu-O}_2)$ is considerably more intense with UV excitation than with visible. This indicates that the 345 nm absorption band has peroxide \rightarrow Cu(II) CT character. The lack of a deuterium isotope effect on either $\nu(\text{O-O})$ or $\nu(\text{Cu-O}_2)$ implies that the bound peroxide moiety is not involved in hydrogen bonding. Its association with two Cu(II) ions must, therefore, provide adequate stabilization to allow for the reversible dissociation of O_2 and to prevent irreversible oxidation by the dissociation of O_2^{2-} . These results contrast with those obtained for hemoglobin and hemerythrin where the bound dioxygen is associated with only one metal ion and the complexes must be further stabilized by the formation of hydrogen bonds.

REFERENCES

1. Solomon, E. I. (1988) in Oxidases and Related Redox Systems (King, T. E., Mason, H. S., and Morrison, M., eds.), pp. 309-329, Alan R. Liss, Inc., New York.
2. Préaux, G., and Gielens, C. (1984) in Copper Proteins and Copper Enzymes (Lontie, R., ed.), vol. II, pp. 160-198, CRC Press, Inc., Boca Raton, FL.
3. Solomon, E. I. (1981) in Copper Proteins (Spiro, T. G., ed.), vol. 3, pp. 41-108, Wiley, New York.
4. Loehr, T. M., and Shiemke, A. K. (1988) in Biological Applications of Raman Spectroscopy (Spiro, T. G., ed.), Vol.3, pp. 439-490, Wiley, New York.
5. Lontie, R., and Witters, R. (1981) in Metal Ions in Biological Systems (Sigel, H., ed.), Vol. 13, pp. 229-258, Marcel Dekker, New York.
6. Van Holde, K. E., and Miller, K. I. (1982) Q. Rev. Biophys. 15, 1.
7. Urbach, F. L. (1981) in Metal Ions in Biological Systems (Sigel, H., ed.), Vol. 13, pp. 73-115, Marcel Dekker, New York.
8. (a) Dooley, D. M., Scott, R. A., Ellinghaus, J., Solomon, E. I., and Gray, H. B. (1978) Proc. Natl. Acad. Sci. USA 75, 3019.
(b) Moss, T. H., Gould, D. C., Ehrenberg, A., Loehr, J. S., and Mason, H. S. (1973) Biochemistry 12, 2444.
9. Wilcox, D. E., Long, J. R., and Solomon, E. I. (1984) J. Am. Chem. Soc. 106, 2186.

10. Linzen, B., Soeter, N. M., Riggs, A. F., Schneider, H.-J., Schartau, W., Moore, M. D., Yokota, E., Behrens, P. Q., Nakashima, H., Takagi, T., Nemoto, T., Vereijken, J. M., Bak, H. J., Beintema, J. J., Volbeda, A., Gaykema, W. P. J., and Hol, W. G. J. (1985) Science **229**, 519.
11. (a) Karlin, K. D., Haka, M. S., Cruse, R. W., Meyer, G. J., Farooq, A., Gultneh, Y., Hayes, J. C., and Zubieta, J. (1988) J. Am. Chem. Soc. **110**, 1196.
(b) Coughlin, P. K., and Lippard, S. J. (1981) J. Am. Chem. Soc. **103**, 3228.
12. (a) Gaykema, W. P. J., Volbeda, A., and Hol, W. G. J. (1986) J. Mol. Biol. **187**, 255.
(b) Volbeda, A., and Hol, W. G. J. (1988) in Oxidases and Related Redox Systems (King, T. E., Mason, H. S., and Morrison, M., eds.), pp. 291-307, Alan R. Liss, New York.
(c) Lerch, K., Huber, M., Schneider, H.-J., Drexel, R., and Linzen, B. (1986) J. Inorg. Biochem. **26**, 213.
13. Woolery, G. L., Powers, L., Winkler, M., Solomon, E. I., and Spiro, T. G. (1984) J. Am. Chem. Soc. **106**, 86.
14. Co, M. S., and Hodgson, K. O. (1981) J. Am. Chem. Soc. **103**, 3200.
15. Co, M. S., Hodgson, K. O., Eccles, T., and Lontie, R. (1981) J. Am. Chem. Soc. **102**, 984.
16. Freedman, T. B., Loehr, J. S., and Loehr, T. M. (1976) J. Am. Chem. Soc. **98**, 2809.

17. Thamann, T. J., Loehr, J. S., and Loehr, T. M. (1977) J. Am. Chem. Soc. **99**, 4187.
18. Eickman, N. C., Himmelwright, R. S., and Solomon, E. I. (1979) Proc. Natl. Acad. Sci. USA **76**, 2094.
19. Larrabee, J. A., Spiro, T. G., Ferris, N. S., Woodruff, W. H., Maltese, W. A., and Kerr, M. S. (1977) J. Am. Chem. Soc. **99**, 1979.
20. Schugar, H. J., Solomon, E. I., Cleveland, W. L., and Goodman, L. (1975) J. Am. Chem. Soc. **97**, 6442-6450.
21. Hansen, A. E., and Balehausen, C. J. (1965) Trans. Faraday Soc. **61**, 631-639.
22. Larrabee, J. A., and Spiro, T. G. (1980) J. Am. Chem. Soc. **102**, 4217.
23. Cornilsen, B. C., and Nakamoto, K. (1974) J. Inorg. Nucl. Chem. **36**, 2467.
24. Reed, C. A. (1985) in Biological and Inorganic Copper Chemistry (Karlin, K. D., Zubieta, J., eds.), pp. 61-73, Academic Press, New York.
25. Shiemke, A. K., Loehr, T. M., and Sanders-Loehr, J. (1984) J. Am. Chem. Soc. **106**, 4951.
26. Czernuszewicz, R. S., Sheats, J. E., and Spiro, T. G. (1987) Inorg. Chem. **26**, 2063.
27. (a) de Phillips, H. A., Jr., Nickerson, K. W., and van Holde, K. E. (1970) J. Mol. Biol. **50**, 471.
(b) Ke, C. H., and Shubert, J. (1972) Radiat. Res. **49**, 507.

28. Loehr, T. M., Keyes, W. E., Pincus, P. A. (1979) Anal. Biochem. **96**, 456.
29. Hendra, P. J., and Loader, E. J. (1968) Chem. Ind. 718.
30. Maret, W., Shiemke, A. K., Wheeler, W. D., Loehr, T. M., and Sanders-Loehr, J. (1986) J. Am. Chem. Soc. **108**, 6351.
31. Nestor, L. M., and Spiro, T. G., personal communication.
32. Armstrong, G. D., and Sykes, A. G. (1986) Inorg. Chem. **25**, 3135.
33. Phillips, S. E. V., and Schoenborn, B. P. (1981) Nature **292**, 81.
34. Stenkamp, R. E., Sieker, L. C., Jensen, L. H., McCallum, J. D., and Sanders-Loehr, J. (1985) Proc. Natl. Acad. Sci. USA **82**, 713.
35. Shiemke, A. K., Loehr, T. M., and Sanders-Loehr, J. (1986) J. Am. Chem. Soc. **108**, 2437.
36. Loehr, T. M. (1988) in Oxygen Complexes and Oxygen Activation by Transition Metals (Martell, A. E., and Sawyer, D. T., eds.), pp. 17-32, Plenum, New York.

TABLE I. Assignment of Resonance Raman Vibrational Modes in
Hemocyanin from Busycon canaliculatum

Frequency (cm^{-1})	Δcm^{-1} for $^{65}\text{Cu}^{\text{a}}$	Δcm^{-1} in D_2O	Δcm^{-1} in H_2^{18}O	Assignment ^b
174	0	0	0	-----
230	-2	-1	0	$\nu(\text{Cu-Im})$
269	-2	-1	0	$\nu(\text{Cu-Im})$
292	-2	0	0	$\nu(\text{Cu-X})$
313	-2	-2	0	$\nu(\text{Cu-Im})$
345	0	0	0	-----
550	n.d.	0	0	$\nu(\text{Cu-O}_2)$
747	n.d.	0	0	$\nu(\text{O-O})$

^a Data for ^{65}Cu - relative to ^{63}Cu -substituted hemocyanin obtained at 77 K (ref. 31). n.d. = not determined.

^b Assignment for $\nu(\text{O-O})$ from reference 16. All others from references 22 and 31.

FIGURE LEGENDS

- Figure 1. (A) Active site structure of deoxy hemocyanin based on x-ray crystallography. Six histidine residues at the copper binding site are shown along with the α -helical segments to which they are attached. Adapted from reference 10.
- (B) Proposed structures for deoxy and oxyhemocyanin. Dashed and dotted bonds indicate greater uncertainty. Adapted from reference 24.
- Figure 2. (A) Channeled whelk (Busycotypus canaliculatum).
- (B) Cross-section of Hexis aspersa, a related gastropod. Hemolymph reservoirs lie in soft tissue (heart) behind retractable foot. (1) Indicates the location of the spatula and (2) indicates the location of the syringe needle for extracting the hemolymph.
- Figure 3. Arrangement for passing Ar gas through the sample of hemocyanin for its anaerobic reduction.
- Figure 4. Mass spectra to determine ^{18}O content of hemocyanin sample. (A) Water distribution (^{16}OH , $^{16}\text{OH}_2$, ^{18}OH , $^{18}\text{OH}_2$) in the ultrafiltrate from the first preparation of H_2^{18}O hemocyanin.
- (B) Water content in the instrument. The total counts in the ^{16}OH and $^{16}\text{OH}_2$ peaks in (B) were subtracted from total

counts for ^{16}OH and $^{16}\text{OH}_2$ peaks in (A). The resulting counts were then used to obtain the % ^{18}O in the ultrafiltrate.

Figure 5. Closed-cycle helium dispex used to obtain Raman spectra at 15 K. Gold-plated cold finger is 2.5 cm in diameter and contains 7 depressions which each hold sample volumes of 10-20 μL .

Figure 6. Absorption spectrum of oxyhemocyanin.

Figure 7. Raman spectra of oxyhemocyanin with visible excitation. Conditions used: protein concentration ~ 5 mM in copper in 0.02 M carbonate buffer (pH 9.8), 150 degree backscattering geometry, 100 mW power at the sample. (A) Excitation at 514.5 nm, scan rate of $0.5 \text{ cm}^{-1} \text{ s}^{-1}$, slit width of 5 cm^{-1} , total of 4 scans accumulated with a 25-point smooth. (B) Excitation at 528.7 nm, slit width of 6 cm^{-1} , total of 25 scans with a 17-point smooth. L = laser plasma line.

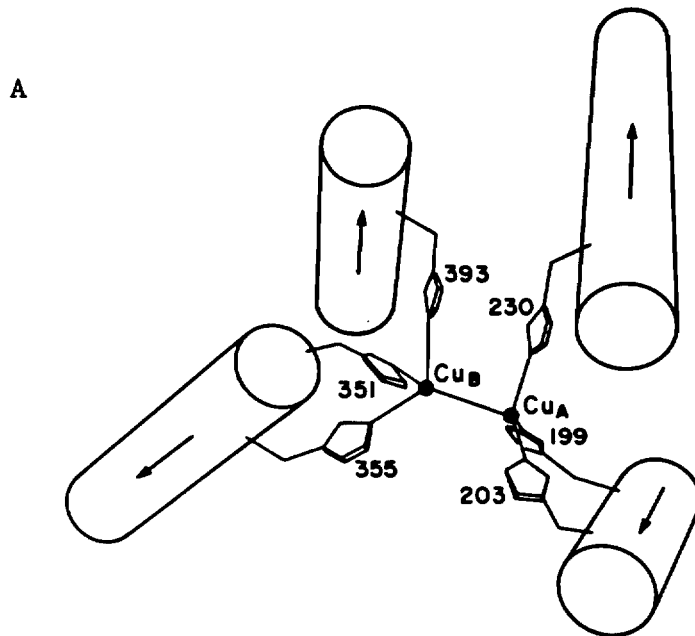
Figure 8. Raman spectra of oxyhemocyanin in H_2O (—) and D_2O (- - -) with visible excitation at 514.5 nm. Conditions as in Figure 7a, 16 scans collected with a 17-point smooth.

Figure 9. Raman spectra of oxyhemocyanin in H_2O (—) and H_2^{18}O (- - -) with UV excitation at 363.8 nm (12 mW). Other conditions as in Figure 7, slit width of 6 cm^{-1} , 16 scans collected with a 21-point smooth.

Figure 10. Low frequency Raman spectra of oxyhemocyanin in H_2O (—) and H_2^{18}O (- - -) with UV excitation at 363.8 nm (10–15 mW). Other conditions as in Figure 7, slit width of 6 cm^{-1} , 16 scans collected with a 9-point smooth.

(A) Data set with 63% H_2^{18}O substitution, filter monochromator omitted. L = laser plasma line.

(B) Data set with 80% H_2^{18}O substitution. Indicated frequencies are for samples in H_2^{16}O .



DEOXYHEMOCYANIN

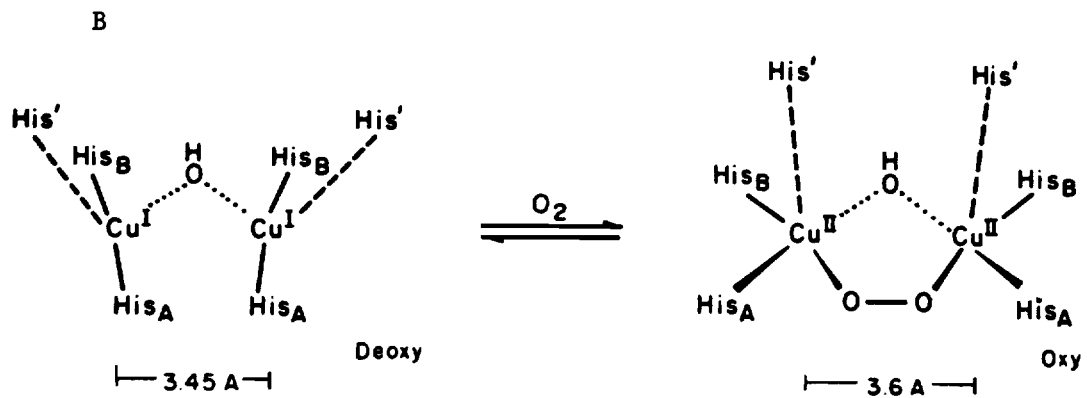


FIGURE 1

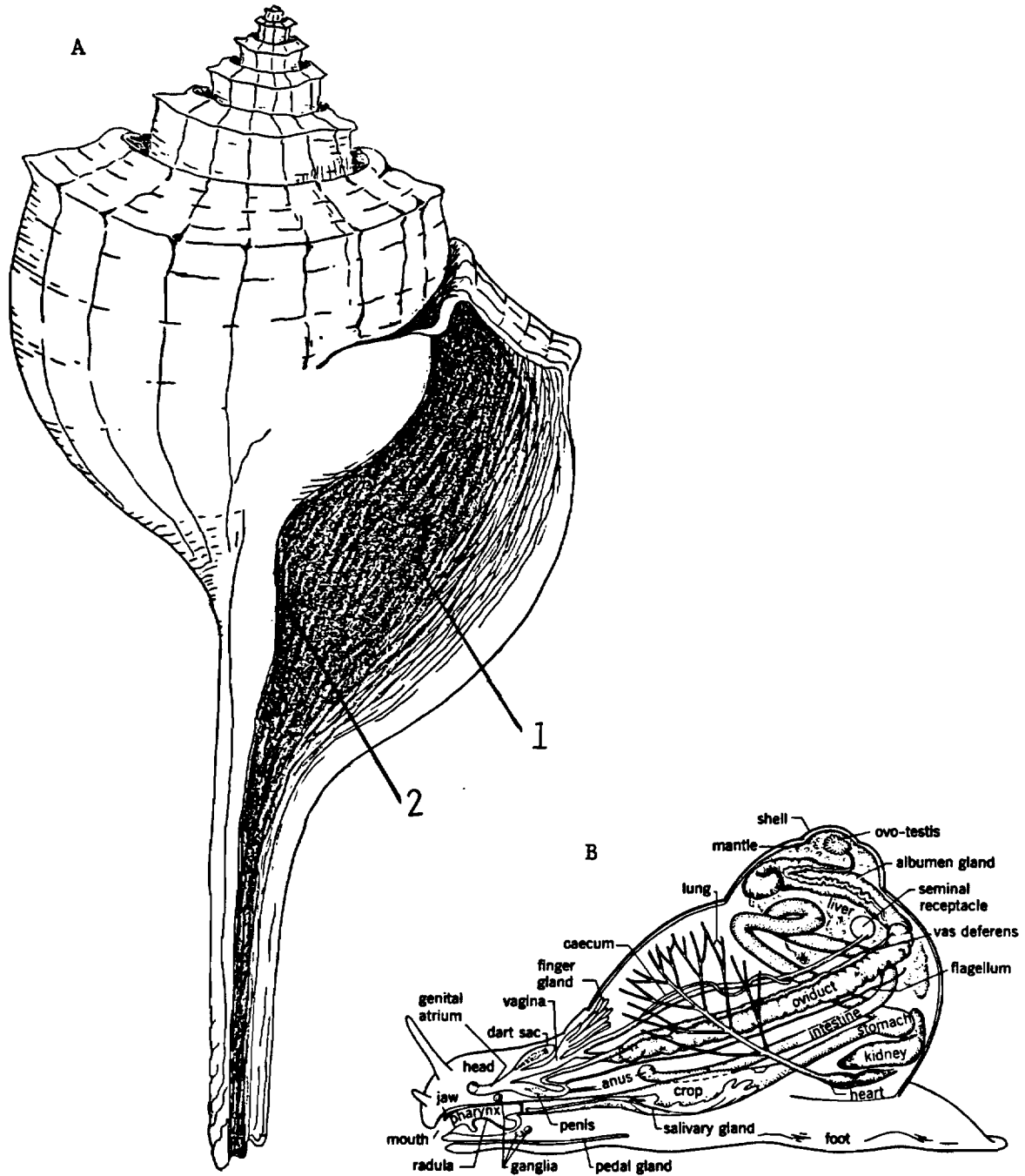


FIGURE 2

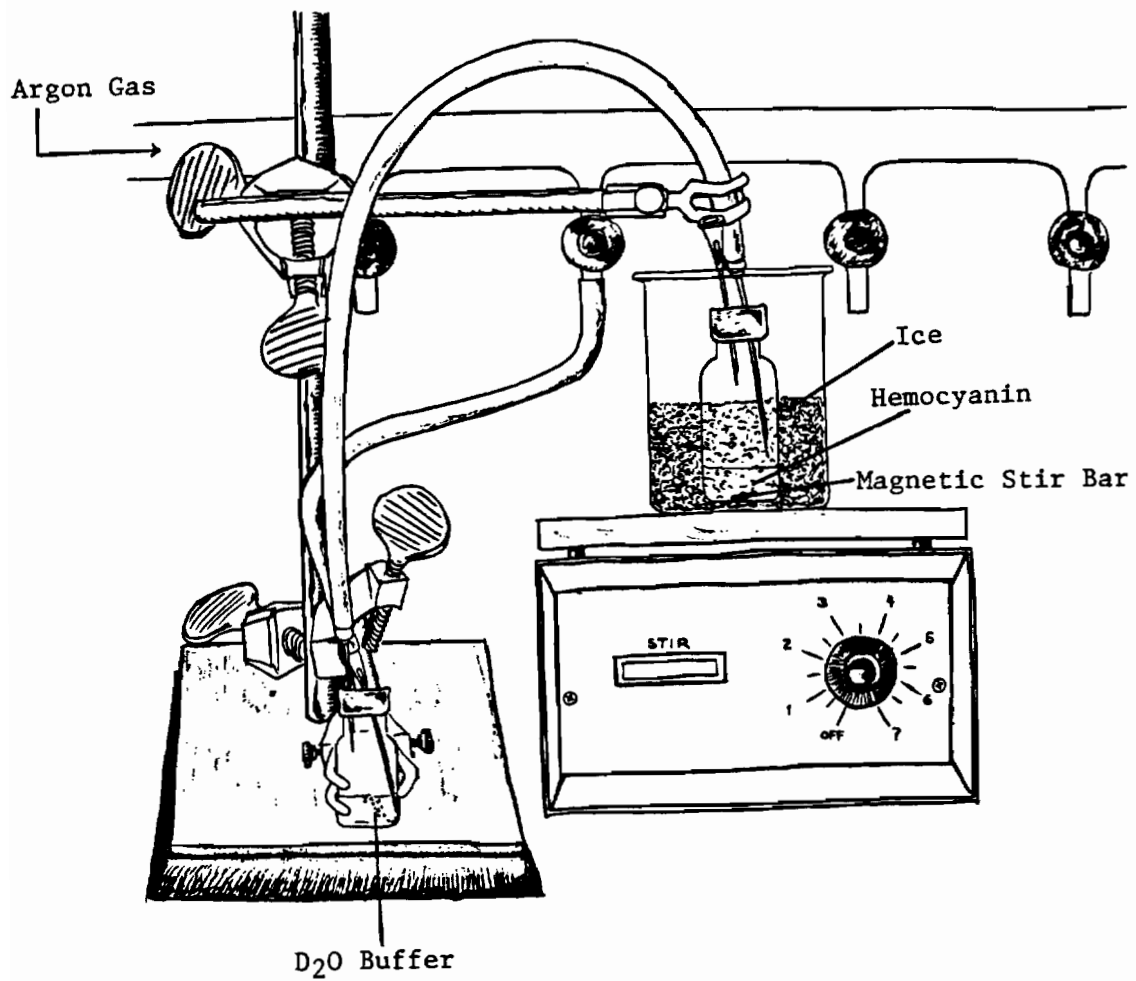


FIGURE 3

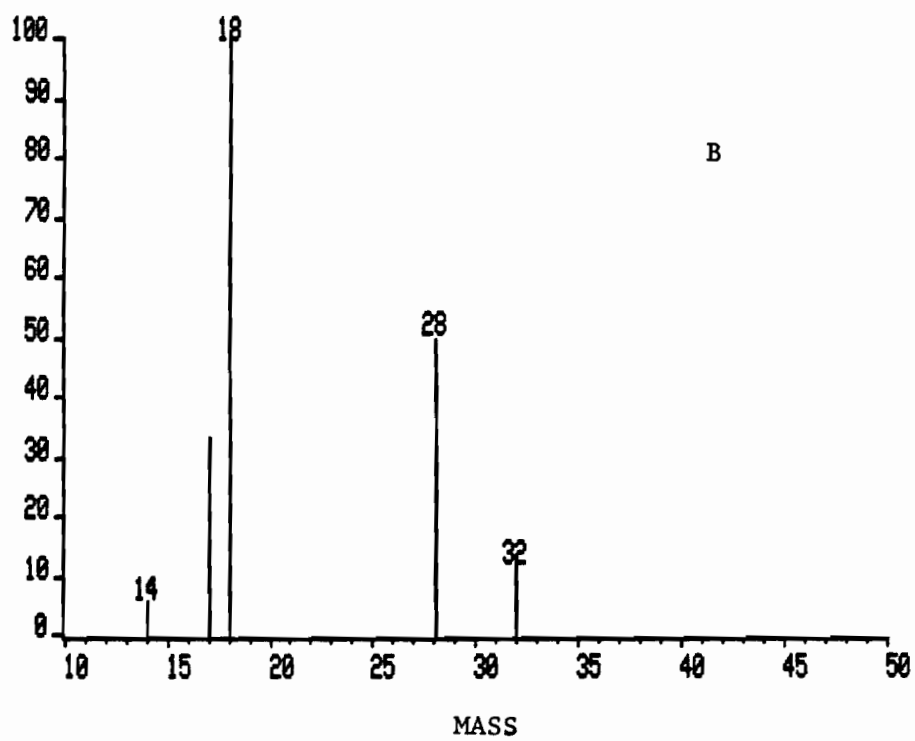
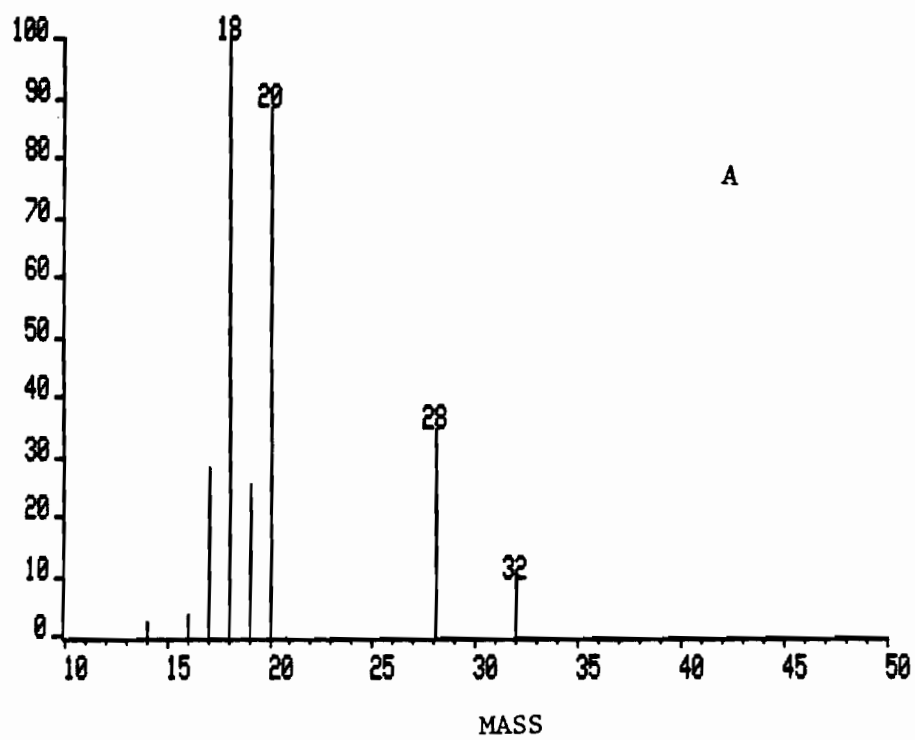


FIGURE 4

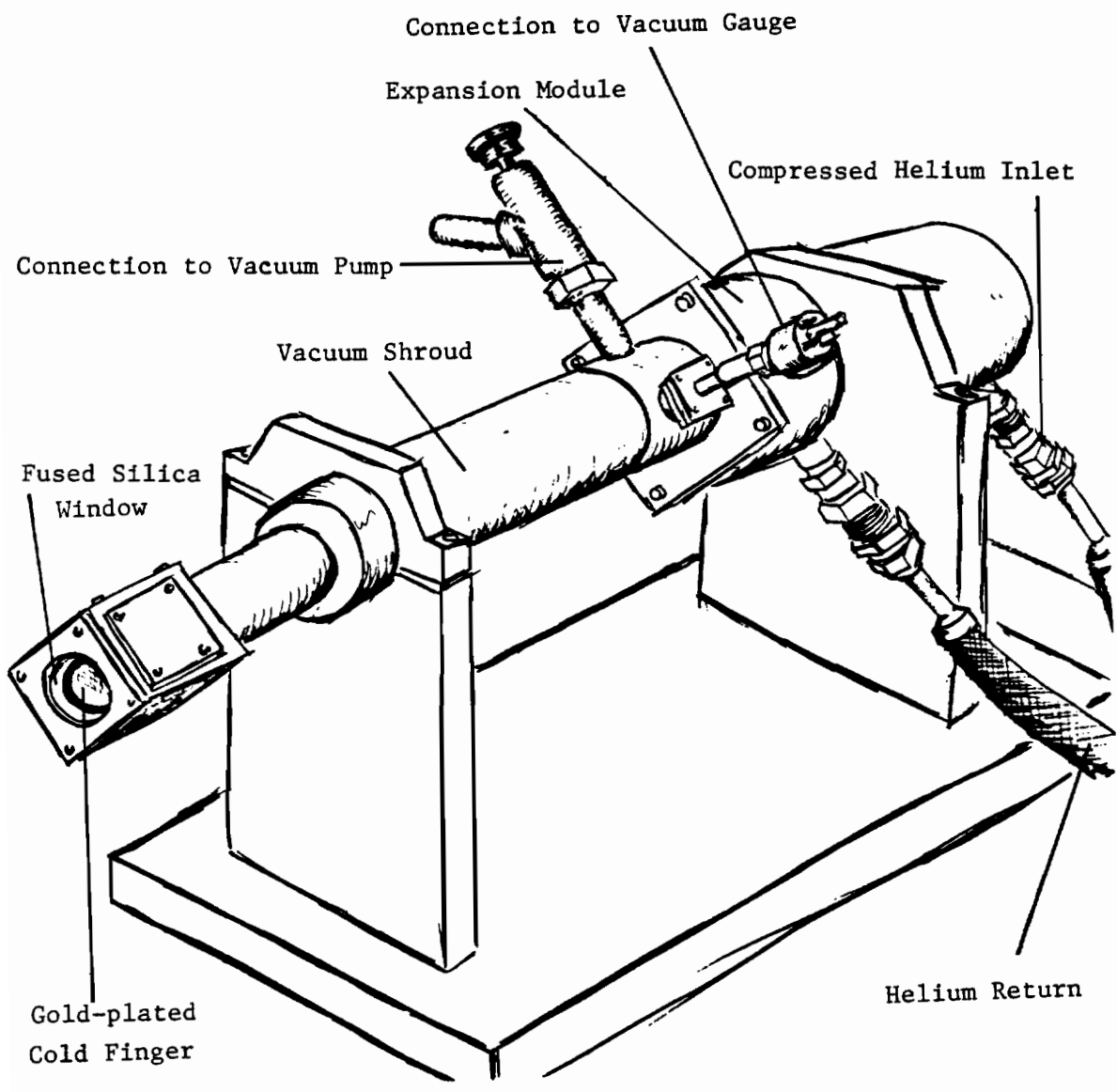


FIGURE 5

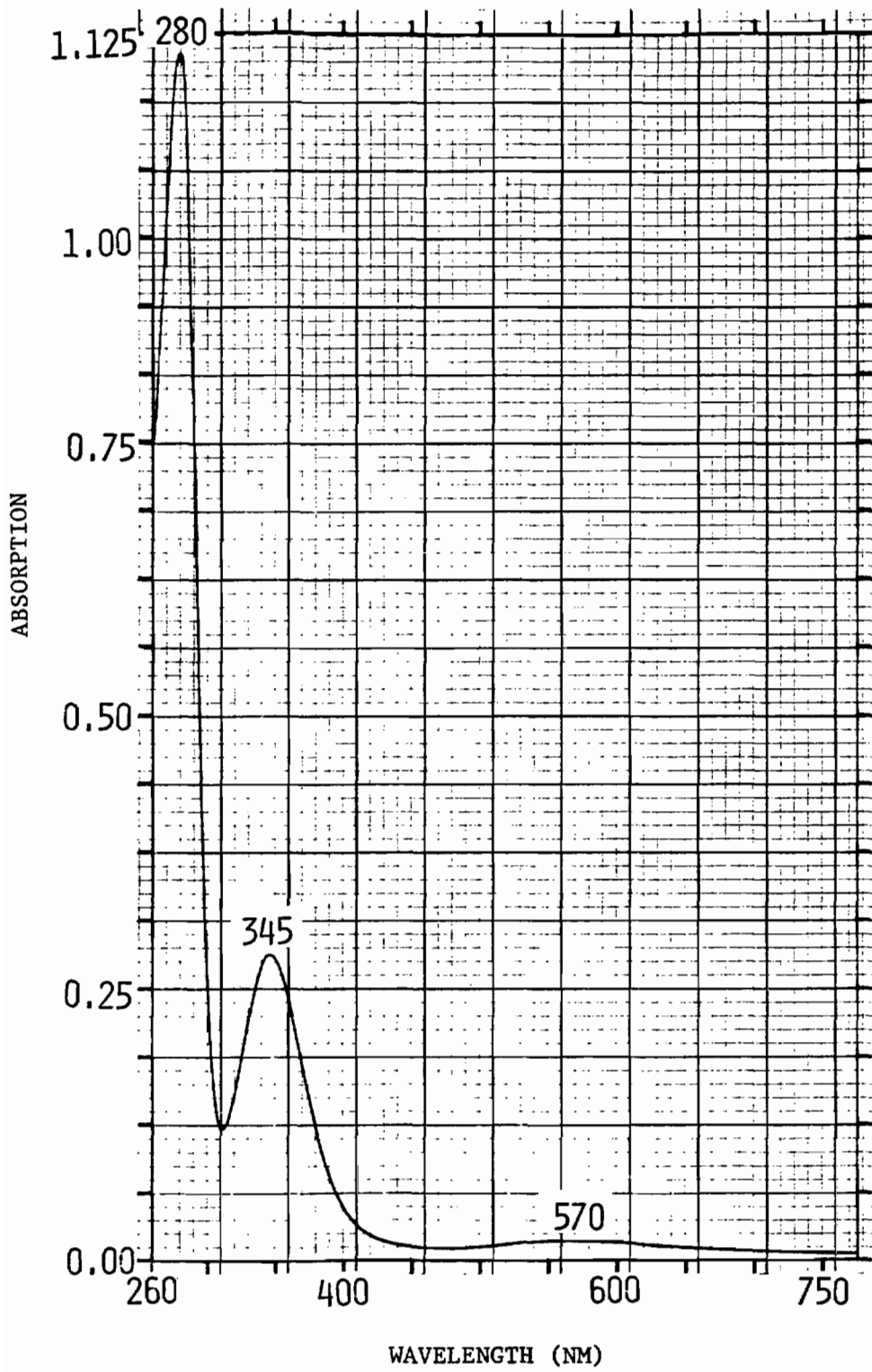


FIGURE 6

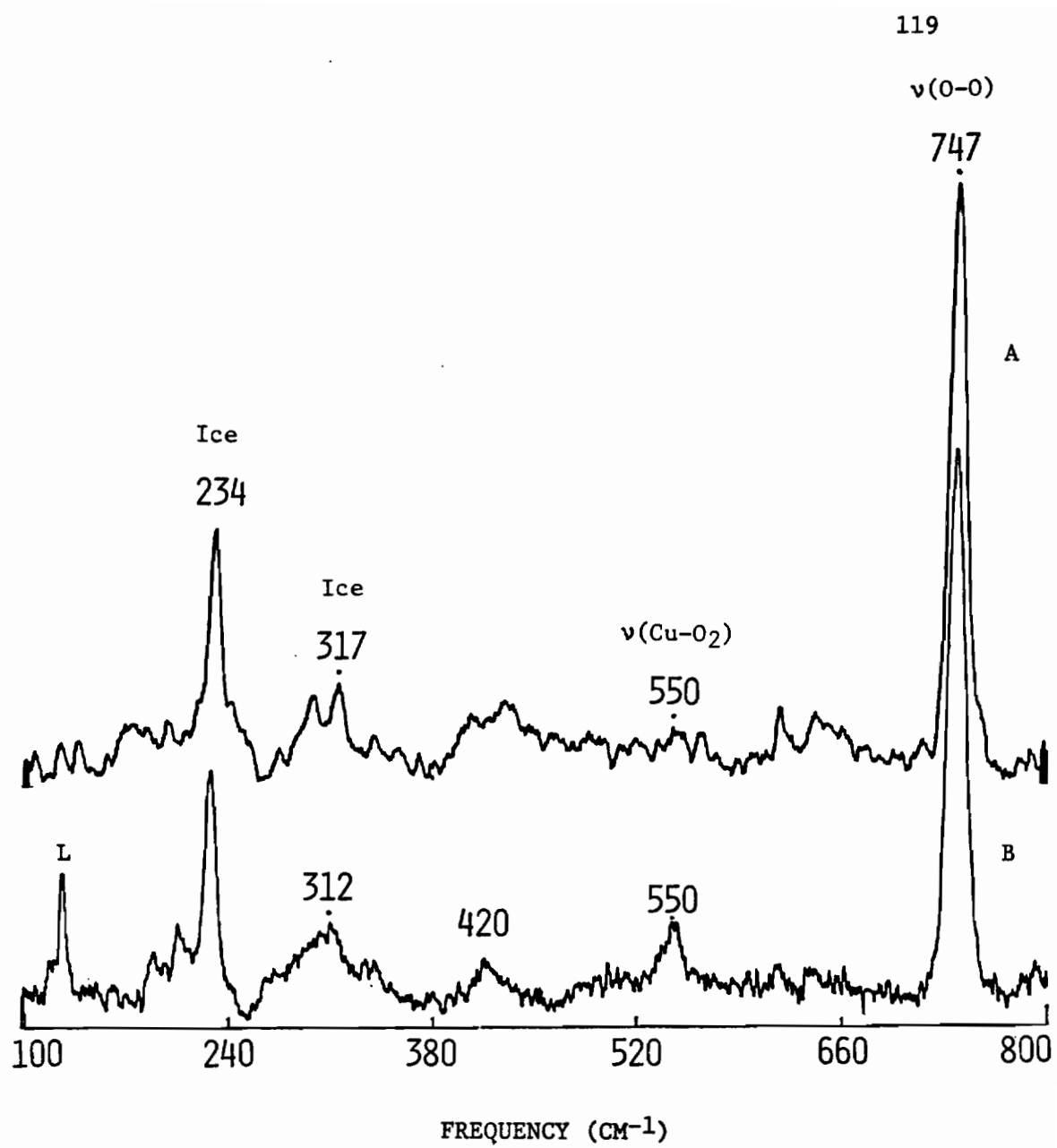


FIGURE 7

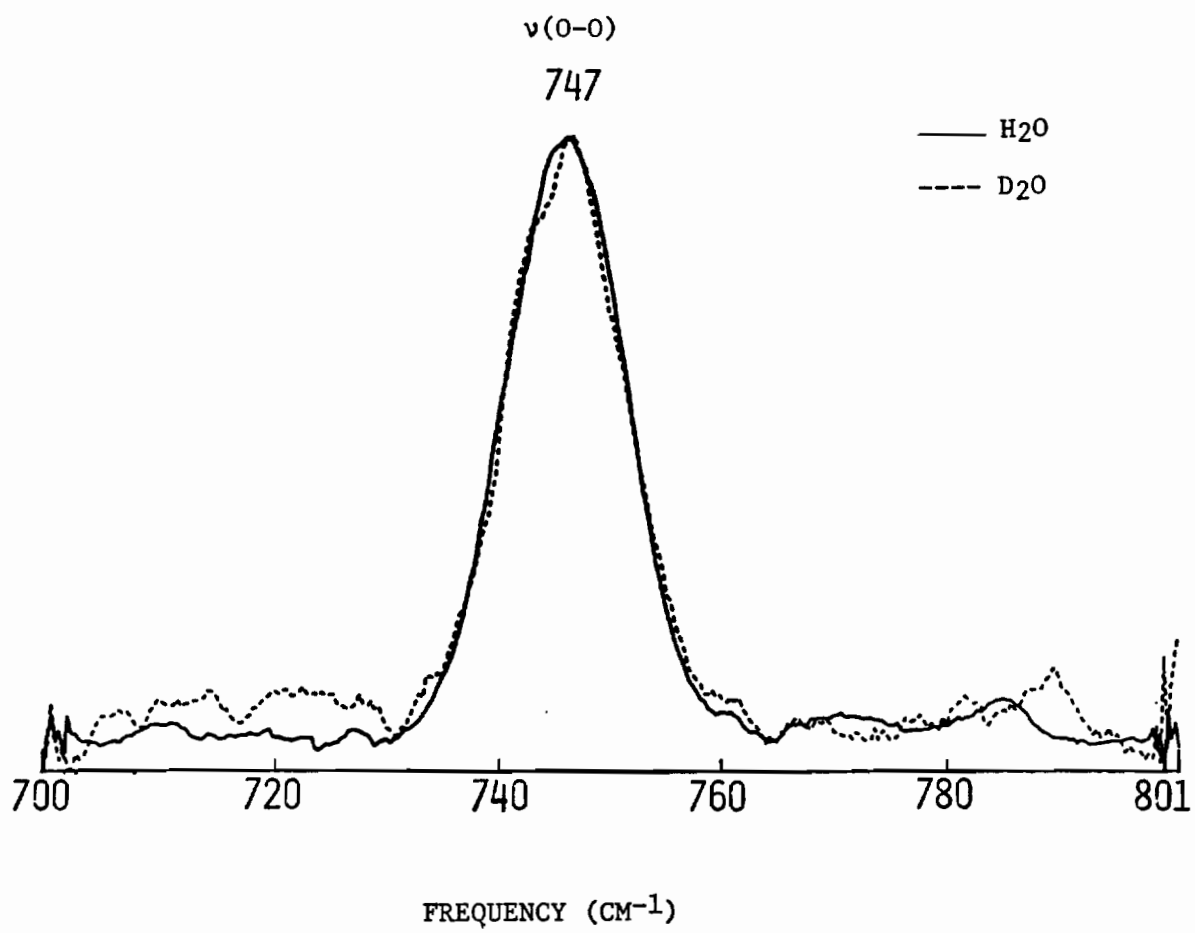


FIGURE 8

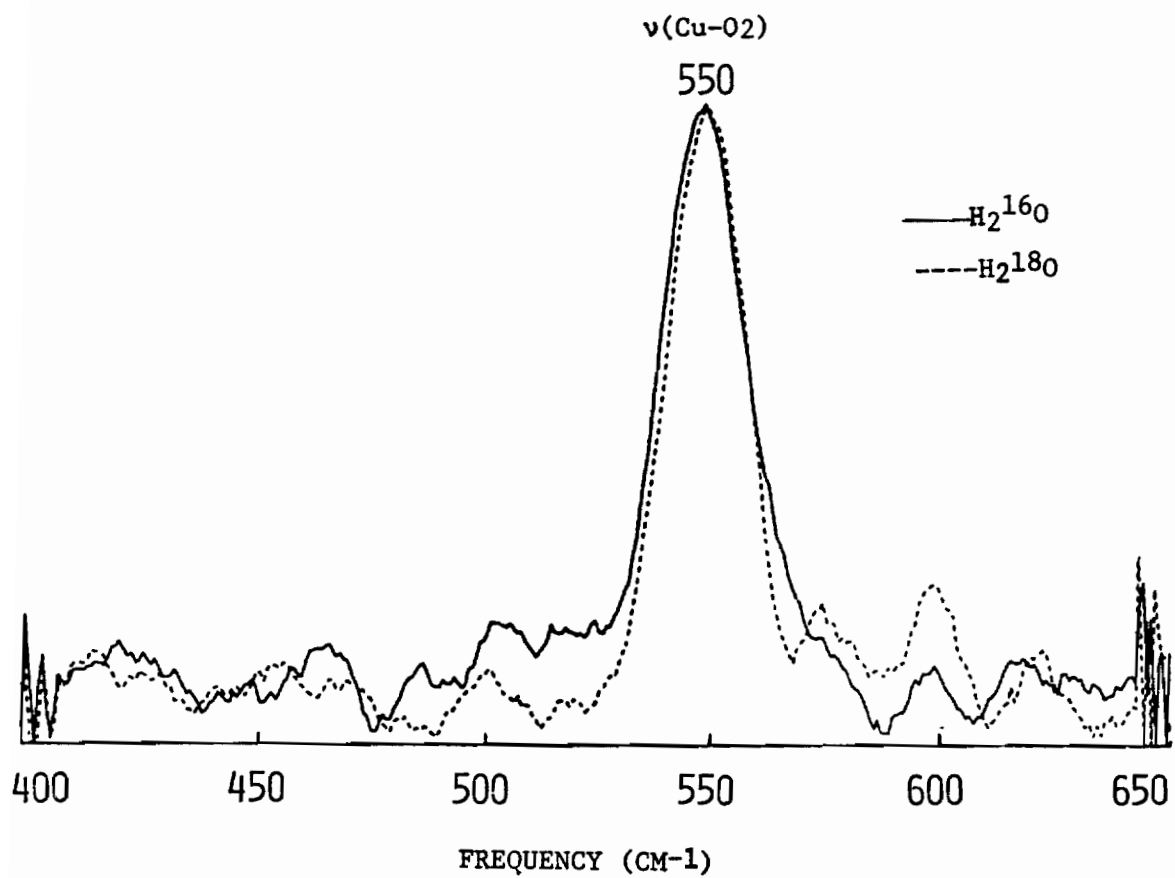


FIGURE 9

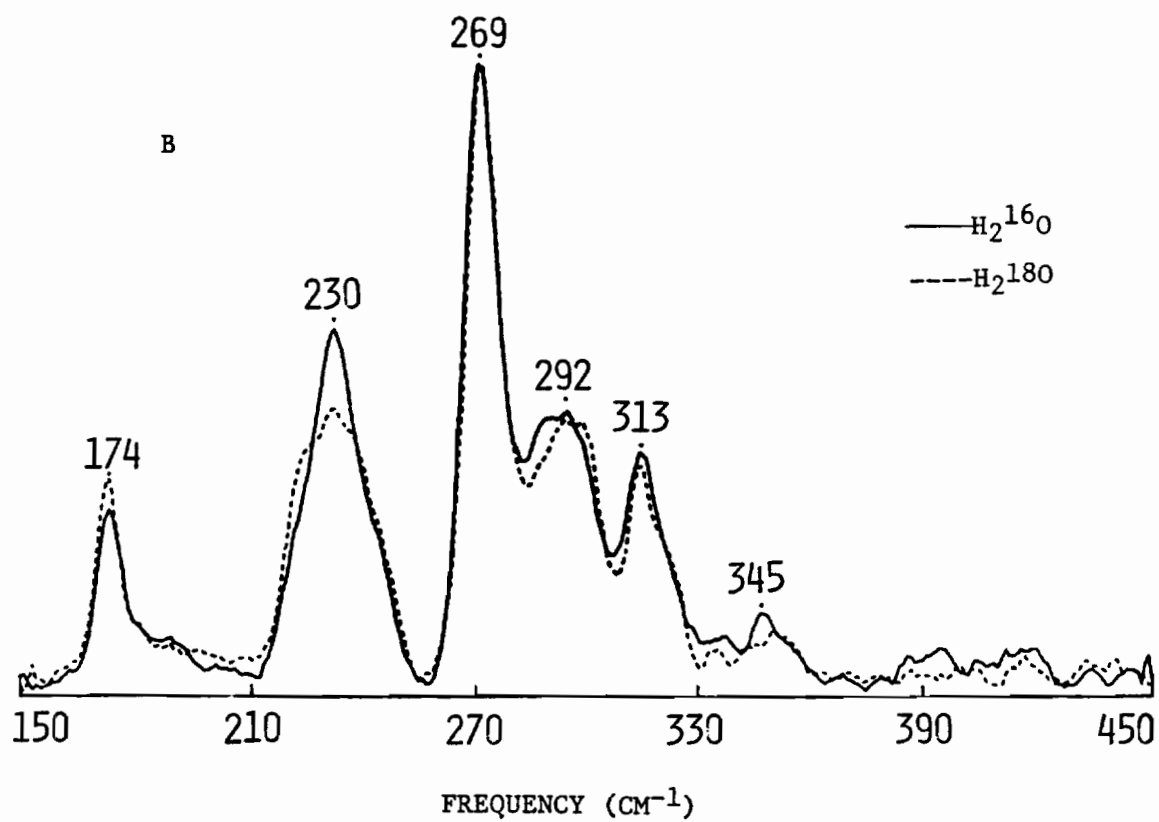
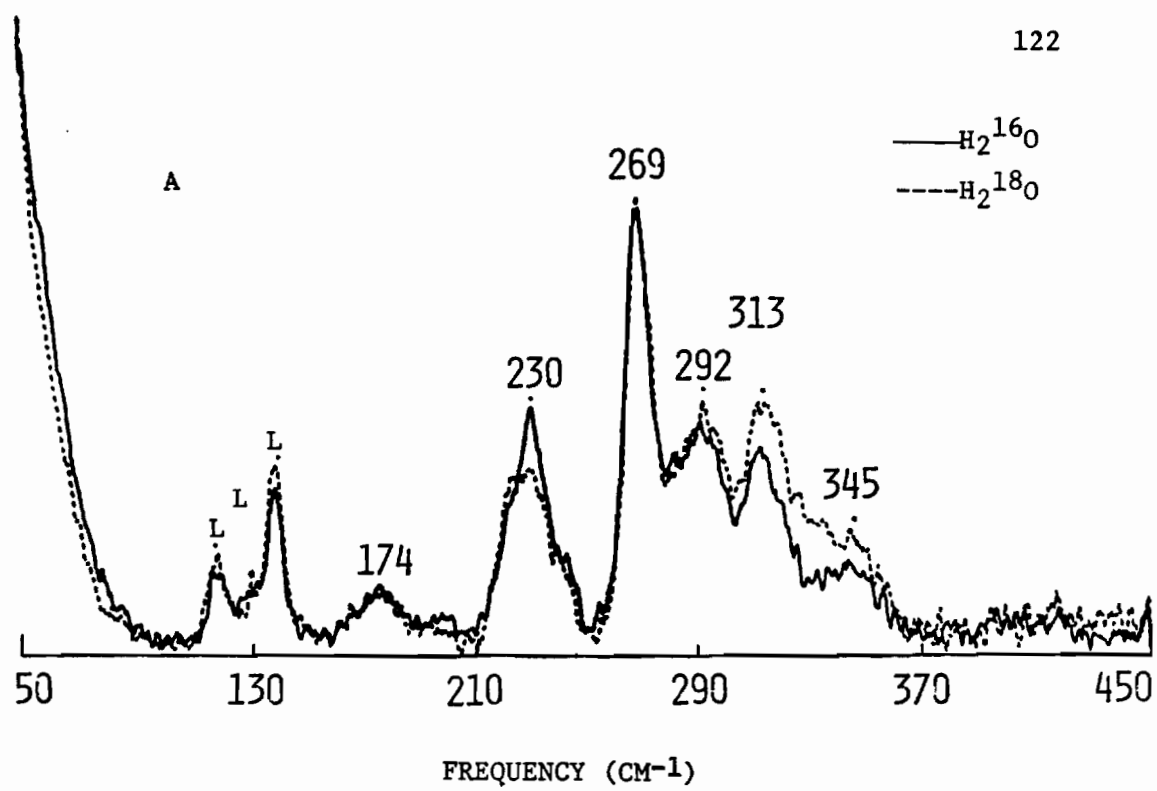


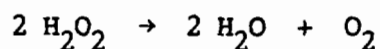
FIGURE 10

CHAPTER V

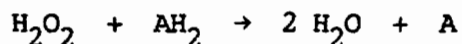
RESONANCE RAMAN SPECTROSCOPY OF MAMMALIAN, FUNGAL AND BACTERIAL CATALASES. EVIDENCE FOR TYROSINATE COORDINATION

INTRODUCTION

Catalases (EC 1.11.1.6 $\text{H}_2\text{O}_2:\text{H}_2\text{O}_2$ oxidoreductase) are ubiquitous heme enzymes found in aerobic organisms ranging from bacteria to higher plants and animals. Functionally, catalases are related to peroxidases: both promote H_2O_2 oxidation by mechanisms which involve ferryl intermediates (1-4). Catalases differ from peroxidases, with the exception of chloroperoxidase (5a) and myeloperoxidase (5b), in their ability to utilize H_2O_2 as both an electron acceptor and an electron donor yielding the disproportionation reaction:



Due to this catalytic activity, catalases are involved in the protective destruction of H_2O_2 generated in respiring cells. Catalases can also oxidize a variety of compounds such as alcohols, alkyl peroxides, and formic acid. This peroxidatic activity requires a hydrogen donor other than hydrogen peroxide:



Catalases are tetrameric proteins of high molecular weight (220,000-350,000) where each subunit has a protoporphyrin IX

prosthetic group. The three-dimensional structures of two catalases are known. The structure of bovine liver catalase has been refined to 2.5-Å resolution by Rossmann and coworkers (6-8) and that of the fungal catalase from Penicillium vitale to 2.0-Å resolution has been reported by Vainshtein and coworkers (9-11). The heme positions and orientations are identical in these two enzymes and are located some 20 Å from the surface accessible via a largely hydrophobic channel (7, 12). The amino acid sequence of bovine catalase consists of 506 residues (13), but that of the larger P. vitale catalase remains to be determined, although an x-ray sequence of 670 residues has been proposed (11).

A surprising result from the crystal structure analyses of the two catalases is the iron coordination to an axial tyrosinate ligand (residue 357 in the bovine liver sequence; residue 345 in the fungal catalase). Comparisons with structures of other heme enzymes show this to be an anomalous fifth ligand (14, 15), although the identity of the proximal ligand in catalase had been debated for several decades (1, 15). The occupancy of the sixth coordination site is less clear, the question being whether or not a water molecule is ligated in the resting form. It appears to be vacant in the resting bovine enzyme as judged from the absence of electron density above the iron (7), whereas electron density near the distal histidine in P. vitale catalase might be a water molecule (11). Another anomaly exhibited by catalases is their resistance to reduction by reagents such as dithionite (1). This may relate to inaccessibility by anionic reagents. The negatively charged tyrosinate ligand may also

serve to create a sufficiently weak ligand field to hold iron in its high-spin ferric resting state, and facilitate the formation of high valent intermediates.

The present study was undertaken to provide the first comprehensive investigation of several catalases by resonance Raman spectroscopy. In addition, we wished to probe the utility of resonance Raman spectroscopy for identifying tyrosinate ligand vibrations in heme enzymes. Non-heme iron-tyrosinate proteins and iron-phenolate model complexes exhibit highly characteristic resonance-enhanced vibrational modes of the coordinated phenolate ligand when excited within their phenolate \rightarrow Fe(III) charge transfer (CT) bands (16-18). In heme proteins, axial metal-ligand vibrations have been studied by resonance Raman spectroscopy, although their intensities are generally weaker by comparison to the strongly enhanced porphyrin ring vibrational modes. Thus, for example, the Fe-O₂ vibration of hemoglobin (19), the Fe-S(cysteinate) vibration of cytochrome P-450-cam (20), and the Fe-N(histidine) vibration of deoxymyoglobin (21, 22) have been reported.

Heme-linked tyrosine ligands were previously known only in hemoglobin (Hb) mutants (23, 24). The crystal structure of Hb M Boston [His-E7(58) α \rightarrow Tyr] shows that the distal histidine is replaced by a tyrosine which coordinates to the Fe(III) and displaces the usual proximal His-F8, yielding a 5-coordinate iron incapable of O₂-binding (24). In Hb M Iwate [His-F8(87) α \rightarrow Tyr], the proximal histidine ligand is replaced by tyrosine; low resolution x-ray data indicate that the iron is six coordinate, binding both the abnormal

tyrosine and the distal His-E7 (23). Resonance Raman spectra of these mutant hemoglobins have been investigated by Nagai et al. and shown to reveal several vibrational bands characteristic of tyrosinate coordination (25). Their data show that Fe(III) in the hemes of Hb M Boston and Iwate is high spin, suggesting that the metal ion in both mutants is five coordinate. Moreover, the observation of Ainscough et al. (26) that addition of 1-methylimidazole to Hb M Iwate produced a low-spin, six-coordinate heme supported the spectroscopic finding. The only previous resonance Raman study of catalase focused on the spectral distinction between the resting form and compound II of the horse blood enzyme (27). That paper predated the recent x-ray structural investigations of catalases and, hence, could not address the tyrosinate ligation.

Here we report resonance Raman spectra of bovine, Aspergillus niger (fungal), and Micrococcus luteus (bacterial) catalases. The consistent observation of weak vibrational modes typical of coordinated tyrosine that are maximally enhanced with visible excitation confirms the presence of the tyrosine ligand in bovine catalase, and suggests the same ligation in the A. niger and M. luteus enzymes.

MATERIALS AND METHODS

Bovine liver catalase, purchased as a crystalline suspension in alkylbenzyltrimethylammonium chloride (Boehringer Mannheim), was further purified similar to previous methods (28, 29). Five mL of

the suspension were exhaustively dialyzed against deionized RO water followed by exhaustive dialysis against 20 mM potassium phosphate buffer (pH 7.0). The suspension was centrifuged, and the pellet dissolved overnight in 1.0 mL HEPES buffer (50 mM, pH 7.0) at 4 °C. After a final centrifugation, the resulting deeply colored catalase solution ($\sim 220 \mu\text{M}$, purity index, $\text{RZ} = A_{405}/A_{276} = 0.90$; cf. 0.89 (28)) was used for spectral measurements and found to be stable for up to 2 weeks at 4 °C. Bovine catalase samples were also prepared at pH 5.0 by ultrafiltration (Amicon) in 10 mM acetate buffer containing 100 mM NaCl, and at pH 9.0 by dialyzing the 220 μM sample against Tris/HCl buffer (50 mM, pH 9.0). Sample concentrations were calculated from $\epsilon_{406} = 3.24 \times 10^5 \text{ M}^{-1}\text{cm}^{-1}$ (30).

Samples of A. niger catalase were prepared by dissolution of lyophilized enzyme (Calbiochem-Behring) in 50 mM HEPES buffer (pH 7.01) to a concentration of $\sim 340 \mu\text{M}$ based on $\epsilon_{406} = 3.6 \times 10^5 \text{ M}^{-1}\text{cm}^{-1}$ (31). Although the RZ of this material was only 0.5 (cf. 0.8 in Ref. 31), resonance Raman spectra were very similar in S/N to those of a $\sim 125 \mu\text{M}$ sample purified extensively by column chromatography according to the method of Jones et al. (32). Catalase from M. luteus was prepared following a previously published method (33), and purified by the Jones et al. procedure (32), with a final passage through a hydroxyapatite column. The Raman spectroscopy sample was $\sim 125 \mu\text{M}$ (pH 7.0, phosphate buffer) as calculated from $\epsilon_{406} = 4.0 \times 10^5 \text{ M}^{-1}\text{cm}^{-1}$ (34).

All samples of catalase gave excellent resonance Raman spectra with Soret excitation, but generally showed strong background

fluorescence when subjected to visible-band excitation. This fluorescence is markedly aggravated by sample freezing and thawing. We attempted to identify the fluorophore(s) by excitation between 450 and 600 nm using a Perkin-Elmer MPF-66 spectrofluorimeter with bovine liver catalase samples of 1.2 and 36 μM , but failed to discern any signals. Nevertheless, it is likely that some fluorophore is present in high enough concentration in the 100-300 μM Raman samples to hamper the resonance Raman experiments. Possible sources of fluorescence with excitation >450 nm are bilirubins arising from degraded hemes in catalase (7) or a minor Zn-porphyrin contaminant arising from zinc insertion by ferrochelatase (35). This contaminant does not appear to alter the protein structure sufficiently to be separable by chromatography. No diminution in the fluorescence of bovine liver catalase was achieved by further purification of the Boehringer-Mannheim enzyme on a Sephadex G-75 superfine column by downward elution in 0.1 M HEPES (pH 7.0). Similar results were obtained after extensive chromatography of the A. niger enzyme. Only the M. luteus catalase showed some decrease in fluorescence after repeated separations with hydroxyapatite. Additionally, a M. luteus catalase preparation which had never been frozen gave the highest quality resonance Raman spectra yet obtained with visible excitation. The integrity of all catalase samples was confirmed by absorption spectroscopy and assays for enzyme activity (36) immediately prior to and following Raman spectroscopic measurements. No evidence of laser-induced degradation was observed.

Highly purified crystalline hemin dimethylester, $\text{ClFe}^{\text{III}}\text{PPIX DME}$, where PPIX DME = protoporphyrin IX dimethylester, was a gift from Prof. Kevin M. Smith (University of California, Davis). For Raman studies, 1-2 mg of the sample was dissolved in one mL of CCl_4 , CH_2Cl_2 , or CS_2 . Crystalline hemin (equine, type III) was purchased from Sigma and used without further purification. A second set of complexes was provided by Prof. Harold M. Goff (University of Iowa) which consisted of the functionalized 5-(2-hydroxyphenyl)-10,15,20-tritolyl Fe^{III} porphyrin monomer, $\text{ClFe}(\text{TTOHP})$, and the phenolate-bridged (tetraarylporphinato) Fe^{III} dimer, $[\text{Fe}(\text{TTOP})]_2$, whose structure has been reported (37). This dimer exhibits phenolate coordination to a high-spin Fe^{III} porphyrin, and serves as a catalase model. Resonance Raman samples of the monomer and dimer were prepared in CS_2 solution (1 mg/mL) or mixed in KBr (1-2 mg/100 mg KBr) for illumination in a spinning sample holder.

Electronic absorption spectra were recorded on a Perkin-Elmer Lambda 9 spectrophotometer. Resonance Raman spectra were obtained either on samples maintained at -4°C in standard melting-point capillaries held in a copper cold finger inserted into a Dewar for use with $\sim 150^\circ$ -backscattering or at room temperature using a 90° -scattering geometry. In the latter case, the strong airflow from a four-inch diameter muffin fan was directed against the capillary. Excitation was provided by Spectra-Physics ion lasers (164-05 Ar, 164-01 Kr, 2025-11 Kr). The Raman spectrophotometer and computer programs have been described previously (38, 39). Multiple scans were added to improve the S/N ratio of most spectra.

RESULTS AND DISCUSSION

Absorption Spectra

The electronic absorption spectra of bovine liver, A. niger, and M. luteus catalases are very similar. Their Soret bands are located at 405 ± 1 nm with $\epsilon = 3.24 \times 10^5$ (30), 3.6×10^5 (31), and 4.0×10^5 $M^{-1}cm^{-1}$ (34) for the mammalian, fungal, and bacterial catalases, respectively. The variation in these values most likely reflects inconsistencies in the overall heme integrity of these enzymes rather than fundamental differences in their absorptivities; an effective $\epsilon_{405} = 1 \times 10^5$ $M^{-1}cm^{-1}$ per heme appears to be a reasonable expectation for each of these systems. Their fused α and β bands are typical of pentacoordinated ferric hemes and are observed at 500–550 nm ($\epsilon \sim 4.5 \times 10^4$ $M^{-1}cm^{-1}$). In addition, absorption bands characteristic of high spin ferric hemes are at ~ 625 nm ($\epsilon \sim 2.8 \times 10^4$ $M^{-1}cm^{-1}$).

Porphyrin Marker Bands

Resonance Raman spectra of the three catalases were investigated with a number of different Soret and visible excitation wavelengths because of the strong dependence of the activities of vibrational modes of the porphyrin macrocycle and Fe^{III} -ligand modes on the excitation energy. Data for bovine catalase are shown in Figure 1 for the 900 – 1700 cm^{-1} frequency region, and are listed along with vibrational assignments in Table I. The dominant bands observed in

this region are the oxidation-state, spin-state, and coordination-number marker bands (44, 45). The band most diagnostic of the iron oxidation state is ν_4 which lies at $\sim 1368\text{--}1375\text{ cm}^{-1}$ for ferric hemes and at $\sim 1345\text{--}1360\text{ cm}^{-1}$ for ferrous hemes (39, 44, 45). Its appearance at $\sim 1373\text{ cm}^{-1}$ in resting bovine liver catalase corroborates the Fe^{III} assignment.

The primary bands characteristic of the iron spin state are ν_3 , ν_{19} , and ν_{10} . Since the frequencies of these bands correlate strongly with the heme core size, their positions reflect the spin state of the heme iron (44, 45). For ferric hemes, the observed ranges for these high-spin (hs) and low-spin (ls) markers are as follows. For ν_3 (polarized, maximal intensity with Soret excitation): $1478\text{--}1494\text{ cm}^{-1}$ (hs), $1497\text{--}1508\text{ cm}^{-1}$ (ls); for ν_{19} (anomalously polarized, maximal enhancement with α , β excitation): $1548\text{--}1576\text{ cm}^{-1}$ (hs), $1577\text{--}1590\text{ cm}^{-1}$ (ls); and for ν_{10} (depolarized, α , β excitation): $1605\text{--}1626\text{ cm}^{-1}$ (hs), $1636\text{--}1642\text{ cm}^{-1}$ (ls). The bands at 1483 (ν_3), 1568 (ν_{19}), and 1626 (ν_{10}) cm^{-1} in Figure 1 establish the high-spin nature of the ferric site. As expected ν_3 is maximally enhanced with near-Soret, 457.9-nm excitation whereas the intensities of ν_{19} and ν_{10} increase with 496.5- and 514.5-nm excitation. The 1625-cm^{-1} band most likely includes a contribution from the $\nu(\text{C}=\text{C})_{\text{vinyl}}$ mode. This vibrational mode is polarized and maximally enhanced with Soret excitation, whereas ν_{10} is depolarized and only enhanced by excitation in the visible region. Similarly, the 1571-cm^{-1} peak observed with Soret excitation is assigned to ν_2 .

The degrading quality of the spectra with longer excitation wavelengths, especially with 496.5 and 514.5 nm, arises from the strong background fluorescence discussed above. Resonance Raman spectra of heme proteins and metalloporphyrins are not usually recorded with excitation wavelengths >550 nm. We include in Figure 1 a spectrum excited at 568.2 nm; this spectrum resembles the near-Soret excitation (457.9 nm) spectrum to a much greater extent than any of the spectra obtained with visible excitation. The generality of this observation, although not pursued for the present, may relate to a change in the nature of the scattering mechanism invoked at this wavelength relative to that via α and β band excitation.

The three spin-state marker bands are also sensitive to the coordination number of the heme (39, 40, 44-46). For high-spin Fe^{III} , band ν_3 is at the high end of the range, 1487-1494 cm^{-1} , for pentacoordinate species, but at the low end, 1478-1482 cm^{-1} , for hexacoordinate complexes. Bands ν_{19} and ν_{10} parallel this pattern: 1565-1576 and 1622-1626 cm^{-1} for pentacoordinate, and 1548-1562 and 1605-1612 cm^{-1} , respectively, for hexacoordinate complexes. The values in beef liver catalase are, thus, diagnostic of a pentacoordinate heme as anticipated from the absorption spectrum, and in concert with the x-ray diffraction results (7). Although ν_3 (1484 cm^{-1}) is a little low for typical pentacoordination, both ν_{19} and ν_{10} at 1568 and 1625 cm^{-1} , respectively, are well within the appropriate frequency ranges for pentacoordinate complexes. Moreover, the spectrum shown in Fig. 1A is typical of other pentacoordinate ferric

hemes as, for example, in the peroxidases, horseradish peroxidase (47, 48), manganese peroxidase (39), and lignin peroxidase (49-51).

Corresponding resonance Raman spectra for the A. niger catalase are shown in Figure 2. They are again characteristic of high spin ferric heme with ν_4 at 1373 cm^{-1} , ν_3 at 1489 cm^{-1} , ν_{19} at 1569 cm^{-1} , and ν_{10} at 1625 cm^{-1} . The spectrum obtained with 406.7-nm excitation (Fig. 2A), a wavelength that is in near perfect agreement with the Soret band position, shows even greater enhancement of ν_3 and ν_4 than with 457.9-nm excitation (Figs. 1A or 2B). This is the expected behavior for totally symmetric modes that are dominant with pure A-term scattering (44). The low-frequency spectrum of A. niger catalase recorded with Soret excitation agrees well with that of the porphyrin model complex (Fig. 4, Table I). Longer wavelength excitation of A. niger catalase again leads to substantial fluorescence and, hence, degradation of spectral quality.

In the catalase from A. niger, the evidence for a pentacoordinate iron is even more convincing than for the bovine liver enzyme based on the positions of ν_3 , ν_{19} , and ν_{10} . The crystal structure of a catalase from the related ascomycete fungus, P. vitale, suggests the possibility of a water molecule in the vicinity of the distal histidine (11). The present results make it highly unlikely that there is a ligand in the sixth coordination site.

The resonance Raman spectra of the bacterial catalase from M. luteus (Table I, Figs. 3B and 4) are quite similar to those of the mammalian and fungal sources and again indicative of pentacoordinate,

high-spin Fe^{III} . A study of the polarization properties of the bands in the 1100–1700 cm^{-1} region are shown in Fig. 3B and 3C. These data are very similar to those reported previously for horse blood catalase (27), and the spectra are typical of ferric hemes. The appearance of anomalously polarized bands at 1303, 1346, and 1568 cm^{-1} may be noted immediately. Additionally, two polarized lines are evident; one is the oxidation state marker ν_4 at 1374 cm^{-1} , and the second is a component of the ν_{10} band at 1626 cm^{-1} . The change in the shape of the peak at $\sim 1620 \text{ cm}^{-1}$ between \parallel and \perp polarization indicates that it is the lower frequency component at $\sim 1610 \text{ cm}^{-1}$ that is polarized. Most of the remaining bands in this spectrum appear to be depolarized, consistent with the behavior of non-totally symmetric modes of vibration which are maximally excited in the α and β absorption bands. The cyano adduct (Fig. 3A) has a resonance Raman spectrum characteristic of a hexacoordinate ferric heme. The oxidation-state sensitive band ν_4 is at 1377 cm^{-1} , whereas ν_{10} shifts some 12 cm^{-1} to higher frequency for this low-spin system.

Iron-Tyrosinate Bands

Tyrosine occurs frequently as an iron ligand in non-heme iron proteins and can be readily identified from its resonance Raman "fingerprint" (17). Excitation into the tyrosinate $\rightarrow \text{Fe}^{\text{III}}$ charge transfer band at $\sim 500 \text{ nm}$ leads to the appearance of a characteristic set of phenolate vibrational modes, the most prominent of which are $\nu(\text{C}=\text{C})$ at ~ 1600 and $\sim 1500 \text{ cm}^{-1}$, $\nu(\text{C}-\text{O})$ at $\sim 1270 \text{ cm}^{-1}$, $\delta(\text{C}-\text{H})$ at

$\sim 1170 \text{ cm}^{-1}$, and a coupled $\nu(\text{Fe-O}) + \text{phenolic } \nu_{12}$ at $\sim 570 \text{ cm}^{-1}$. Table II lists the vibrational frequencies of these modes in a number of non-heme iron proteins and a model compound. Most of the phenolate modes occur within a remarkably narrow range of frequencies of $\pm 5 \text{ cm}^{-1}$, despite the certain wide range of protein environments. The most variable is $\nu(\text{C-O})$ which has been observed between $\sim 1260\text{--}1290 \text{ cm}^{-1}$.

Tyrosinate ligation to heme iron has been reported for two hemoglobin mutants based on crystallographic data, and has been corroborated by resonance Raman spectroscopy (Table II). In this case, four of the five tyrosinate modes appeared as distinct, polarized spectral peaks which increased in intensity as the excitation wavelength increased from 457.9 nm to 514.5 nm. We thought that a similar set of peaks should be detectable in the resonance Raman spectra of the various catalases. In fact, only one of the five modes, $\nu(\text{C=C})$ at $\sim 1612 \text{ cm}^{-1}$, is definitively and repeatedly observable.

The Raman spectra of all three catalases show a new peak at $\sim 1612 \text{ cm}^{-1}$ which is a distinct feature with 488.0- and 496.5-nm excitation, but diminishes to a shoulder upon excitation at 457.9 or 514.5 nm (Figs. 1-3). Comparison with the heme model compounds (Table I, Fig. 5) shows that this frequency is not a typical Raman mode for a pentacoordinate ferric porphyrin. Although it might be argued that this band is due to ν_{10} from a residual amount of a six-coordinate catalase species, this is untenable in view of the following facts: (a) the band is more strongly enhanced by 488.0-

than 514.5-nm excitation; this would not be expected for ν_{10} ; (b) the 1612-cm^{-1} band is insensitive to pH variation between 5.5 and 9.3, a range which should affect water coordination as a possible sixth ligand; (c) polarization studies indicate that a major component of the $1610/1625\text{-cm}^{-1}$ band is polarized (Fig. 3C), also inconsistent with its identification as ν_{10} ; and (d) the band is still clearly present in the low-spin, hexacoordinate cyano adduct (Fig. 3A). Thus, it is likely that the $\sim 1612\text{ cm}^{-1}$ vibration is indicative of a coordinated tyrosinate ligand in bacterial as well as fungal and mammalian catalase.

In addition to the peak at $\sim 1610\text{ cm}^{-1}$, a potential $\nu(\text{C-O})$ mode is observed at $\sim 1245\text{ cm}^{-1}$ for the native mammalian and fungal catalases (Figs. 1 and 2) and for the cyano derivative of the bacterial catalase (Fig. 3A). The anomalously low frequency of this vibrational mode could be accounted for by the known electrostatic interaction between the phenolate oxygen ligand and a nearby arginine residue; this interaction has been detected in the crystal structures of both the mammalian and fungal catalases (7, 12). Weaker features at ~ 1510 , 1175 , and 570 cm^{-1} could be obscured by porphyrin modes at 1525 , 1165 , and 555 cm^{-1} (Table I, Fig. 5) or by ν_3 at $\sim 1505\text{ cm}^{-1}$ in cyano catalase (Fig. 3A). The relative intensities of tyrosinate modes in catalases are quite different from those in non-heme iron proteins where the $\sim 1270\text{ cm}^{-1}$ mode is the strongest spectral feature and the peaks at ~ 1600 , 1500 , 1170 , and 570 cm^{-1} are of approximately equal intensity (16, 17). The predominance of the $\sim 1610\text{-cm}^{-1}$ mode may be more typical of tyrosine-

linked heme proteins. In the spectra of the mutant hemoglobins (25), although three of the other tyrosinate modes are clearly present, the feature at $\sim 1610 \text{ cm}^{-1}$ is of equal or greater intensity to that at $\sim 1270 \text{ cm}^{-1}$ and considerably more intense than those at ~ 1500 and 570 cm^{-1} .

The maximal enhancement of the catalase modes with $\sim 490\text{-nm}$ excitation is in accord with the observation of tyrosinate $\rightarrow \text{Fe}^{\text{III}}$ CT bands at $460\text{--}550 \text{ nm}$ in non-heme iron-tyrosinate proteins (17, 18). Although the molar absorptivities of these transitions are high, i.e., $\sim 2,000 \text{ M}^{-1}\text{cm}^{-1}$ per tyrosine ligand (52), they are comparatively weak relative to the very strong α and β bands in the optical spectra of the catalases. Indeed, the electronic absorption spectra of the catalases give no indication of the presence of such $\text{Tyr} \rightarrow \text{Fe}^{\text{III}}$ CT bands. A similar behavior is observed for the tetratolylporphyrin dimer, $[\text{Fe}(\text{TTOF})]_2$, where new peaks assignable to tyrosinate modes (Table II) are maximally enhanced with $\sim 488.0\text{-nm}$ excitation despite the lack of a distinct $\text{Tyr} \rightarrow \text{Fe}^{\text{III}}$ CT transition in the absorption spectrum. The features at 1588 and 1298 cm^{-1} are not observed in the Raman spectra of the monomer, $\text{ClFe}(\text{TTOHP})$, and are polarized, as expected for these tyrosinate modes. The 623-cm^{-1} peak in the dimer may be assigned to the $\nu(\text{Fe-O})$ mode, its high energy being commensurate with the short Fe-O bond length of 1.85 \AA (37). Two other new features which are less readily assigned to tyrosinate vibrations appeared at 663 and 904 cm^{-1} .

In conclusion, the resonance Raman spectra of hemes with coordinated tyrosines show that the tyrosinate ligand is most readily

identified by the appearance of a new polarized band at $\sim 1612\text{ cm}^{-1}$ which is maximally enhanced with visible excitation. This is very likely accompanied by another polarized mode at $1245\text{--}1310\text{ cm}^{-1}$. The other three modes which are diagnostic of iron-tyrosinate ligation in non-heme proteins and model complexes are more difficult to detect. The weak enhancement of (tyrosinate) ligand modes in the Raman spectra of heme-containing proteins and model complexes is typical of heme systems. In most cases, the resonance Raman spectra are dominated by porphyrin vibrational modes with distinctive, but smaller, contributions from axial ligands (59).

Acknowledgments—We are grateful to Professor Joann Sanders-Loehr for helpful discussions. We thank Professors Kevin Smith and Harold Goff for model compounds, Intel Corporation for the gift of the 310 computer system, and Tektronix Corporation for the 4054A graphics terminals. Dr. W. Douglas Wheeler carried out the computer conversion for the Raman spectrophotometer and revised our programs.

REFERENCES

1. Deisseroth, A., and Dounce, A. L. (1970) Physiol. Rev. 50, 319-375
2. Schonbaum, G. R., and Chance, B. (1976) in The Enzymes (Boyer, P. D., ed) Vol. 13, pp. 363-408, Academic Press, New York
3. Frew, J. E., and Jones, P. (1984) in Advances in Inorganic and Bioinorganic Mechanisms (Sykes, A. G., ed) Vol. 3, pp. 175-212, Academic Press, New York
4. Dawson, J. H. (1988) Science 240, 433-439
5. a) Dawson, J. H., and Sono, M. (1987) Chem. Rev. 87, 1255-1276
b) Iwamoto, H., Kobayashi, T., Hasegawa, E., and Morita, Y. (1987) J. Biochem. 101, 1407-1412
6. Murthy, M. R. N., Reid, T. J., III, Sicignano, A., Tanaka, N., and Rossmann, M. G. (1981) J. Mol. Biol. 152, 465-499
7. Fita, I., and Rossmann, M. G. (1985) J. Mol. Biol. 185, 21-37
8. Fita, I., Silva, A. M., Murthy, M. R. N., and Rossmann, M. G. (1986) Acta Cryst. B42, 497-515
9. Vainshtein, B. K., Melik-Adamyanyan, W. R., Barynin, V. V., and Vagin, A. A. (1980) Dokl. Akad. Nauk U. S. S. R. 250, 242-246
10. Vainshtein, B. K., Melik-Adamyanyan, W. R., Barynin, V. V., Vagin, A. A., and Grebenko, A. I. (1981) Nature (London) 293, 411-412
11. Vainshtein, B. K., Melik-Adamyanyan, W. R., Barynin, V. V., Vagin, A. A., Grebenko, A. I., Borisov, V. V., Bartels, K. S., Fita, I., and Rossmann, M. G. (1986) J. Mol. Biol. 188, 49-61
12. Melik-Adamyanyan, W. R., Barynin, V. V., Vagin, A. A., Borisov, V.

- V., Vainshtein, B. K., Fita, I., Murthy, M. R. N., and
Rossmann, M. G. (1986) J. Mol. Biol. 188, 63-72
13. Schroeder, W. A., Shelton, J. R., Shelton, J. B., Robberson, B.,
Apell, G., Fang, R. S., Bonaventura, J. (1982) Arch. Biochem.
Biophys. 214, 397-421
14. Poulos, T. L. (1988) Adv. Inorg. Biochem. 7, 1-33
15. Reid, T. J., III, Murthy, M. R. N., Sicignano, A., Tanaka, N.,
Musick, W. D. L., and Rossmann, M. G. (1981) Proc. Natl. Acad.
Sci. U. S. A. 78, 4767-4771
16. Loehr, T. M., Keyes, W., E., and Sanders-Loehr, J. (1982) in
Oxidases and Related Redox Systems (King, T. E., Mason, H. S.,
and Morrison, M., eds) pp. 463-482, Pergamon, Oxford
17. Que, L., Jr. (1988) in Biological Applications of Raman
Spectroscopy (Spiro, T. G., ed) Vol. 3, pp. 491-521, Wiley,
New York
18. Que, L., Jr. (1983) Coord. Chem. Rev. 50, 73-108
19. Brunner, H. (1974) Naturwissenschaften 61, 129-130
20. Champion, P. M., Gunsalus, I. C., and Wagner, G. C. (1978)
J. Am. Chem. Soc. 100, 3743-3751
21. Kitagawa, T., Nagai, K., and Tsubaki, M, (1979) FEBS Lett. 104,
376-378
22. Argade, P. V., Sassaroli, M., Rousseau, D. L., Inubushi, T.,
Ikedo-Saito, M., and Lapidot, A. (1984) J. Am. Chem. Soc. 106,
6593-6596
23. Greer, J. (1971) J. Mol. Biol. 59, 107-126.
24. Pulsinelli, D. D., Perutz, M. F., and Nagel, R. L. (1973)

Proc. Natl. Acad. Sci. U. S. A. 70, 3870-3873

25. Nagai, K., Kagimoto, T., Hayashi, A., and Kitagawa, T. (1983)
Biochemistry 22, 1305-1311
26. Ainscough, E. W., Addison, A. W., Dolphin, D., and James, B. R.
(1978) J. Am. Chem. Soc. 100, 7585-7591
27. Felton, R. H., Romans, A. Y., Yu, N.-T., and Schonbaum, G. R.
(1976) Biochim. Biophys. Acta 434, 82-89
28. Browett, W. R., and Stillman, M. J. (1979) Biochim. Biophys.
Acta 577, 291-306
29. Eglinton, D. G., Gadsby, P. M. A., Sievers, G., Peterson, J.,
and Thomson, A. J. (1983) Biochim. Biophys. Acta 742, 648-658
30. Samejima, T., and Yang, J. T. (1963) J. Biol. Chem. 238, 3256-
3261
31. Kikuchi-Torii, K., Hayashi, S., Nakamoto, H., and Nakamura, S.
(1982) J. Biochem. 92, 1449-1456
32. Jones, P., Pain, R. H., and Suggett, A. (1970) Biochem. J. 118,
319-323
33. Herbert, D., and Pinsent, J. (1948) Biochem. J. 43, 193-202
34. Chance, B., and Herbert, D. (1950) Biochem. J. 46, 402-414
35. Camadro, J.-M., Ibrahim, N. G., and Levere, R. D. (1984)
J. Biol. Chem. 259, 5678-5682
36. Beers, R. F., Jr., and Sizer, I. W. (1952) J. Biol. Chem. 195,
133-140
37. Goff, H. M., Shimomura, E. T., Lee, Y. J., and Scheidt, W. R.
(1984) Inorg. Chem., 23, 315-321
38. Loehr, T. M., Keyes, W. E., and Pincus, P. A. (1979)

Anal. Biochem. **96**, 456-463

39. Mino, Y., Wariishi, H., Blackburn, N. J., Loehr, T. M., and Gold, M. H. (1988) J. Biol. Chem. **263**, 7029-7036
40. a) Choi, S., Spiro, T. G., Langry, K. C., Smith, K. M., Budd, D. L., and La Mar, G. N. (1982) J. Am. Chem. Soc. **104**, 4345-4351
b) Choi, S., and Spiro, T. G. (1983) J. Am. Chem. Soc. **105**, 3683-3692
41. Abe, M., Kitagawa, T., and Kyogoku, Y. (1978) J. Chem. Phys. **69**, 4526-4534
42. Lord, R. C., and Yu, N.-T. (1970) J. Mol. Biol. **50**, 509-524
43. Yu, N.-T., De Nagel, D. C., and Kuck, J. F. R. (1987) in Biological Applications of Raman Spectroscopy (Spiro, T. G., ed) Vol. 1, pp. 47-80, Wiley, New York
44. Spiro, T. G. (1983) in Iron Porphyrins (Lever, A. B. P., and Gray, H. B., eds) Part II, pp. 89-159, Addison-Wesley, Reading, MA
45. Felton, R. H., and Yu, N.-T. (1978) in The Porphyrins (Dolphin, D., ed) Vol. 3, pp. 346-393, Academic Press, New York
46. Spiro, T. G., Stong, J. D., and Stein, P. (1979) J. Am. Chem. Soc. **101**, 2648-2655
47. Rakhit, G., and Spiro, T. G. (1974) Biochemistry **13**, 5317-5323
48. Turner, J., and Reed, D. E. (1984) Biochim. Biophys. Acta **789**, 80-86
49. Andersson, L. A., Renganathan, V., Chiu, A. A., Loehr, T. M., and Gold, M. H. (1985) J. Biol. Chem. **260**, 6080-6087

50. Andersson, L. A., Renganathan, V., Loehr, T. M., and Gold, M. H. (1987) Biochemistry **26**, 2258-2263
51. Kuila, D., Tien, M., Fee, J. A., and Ondrias, M. R. (1985) Biochemistry **24**, 3394-3397
52. Gaber, B. P., Miskowski, V., and Spiro, T. G. (1974) J. Am. Chem. Soc. **96**, 6868-6873
53. Tomimatsu, Y., Kint, S., and Scherer, J. R. (1973) Biochem. Biophys. Res. Commun. **54**, 1067-1074
54. Ainscough, E. W., Brodie, A. M., Plowman, J. E., Bloor, S. J., Loehr, J. S., and Loehr, T. M. (1980) Biochemistry **19**, 4072-4079
55. Antanaitis, B. C., Streckas, T., and Aisen, P. (1982) J. Biol. Chem. **257**, 3766-3770
56. Averill, B. A., Davis, J. C., Burman, S., Zirino, T., Sanders-Loehr, J., Loehr, T. M., Sage, J. T., and Debrunner, P. G. (1987) J. Am. Chem. Soc. **109**, 3760-3767
57. Keyes, W. E., Loehr, T. M., and Taylor, M. L. (1978) Biochem. Biophys. Res. Commun. **83**, 941-945
58. Pyrz, J. W., Roe, A. L., Stern, L. J., and Que, L., Jr. (1985) J. Am. Chem. Soc. **107**, 614-620
59. Yu, N.-T. (1986) Meth. Enzymol. **130**, 350-409

TABLE I

Raman frequencies for catalases from bovine liver (BL), *A. niger* (AN), and *M. luteus* (ML), and from high-spin ferric porphyrins

Assignment ^a	Catalase			Porphyrin Complexes	
	BL	AN	ML	ClFePP ^b	ClFePP ^c
ν_{10}	1625	1625	1626	1629	1626
$\nu(\text{C}=\text{C})_{\text{vinyl}}$	1625	1627	1624	1630	1626
$\nu(\text{C}=\text{C})_{\text{tyrosinate}}$	1612	1615	1614		
ν_{37}	1587	1591	1592	1589	1591
ν_{19}	1571	1569	1568	1569	1571
ν_2	1568	1574	1570	1567	1570
ν_{11}	1554	1554	1556	1554	1553
ν_{38}	1521	1524	1528	1533	
ν_3	1484	1489	1487	1490	1491
ν_{28}	~1462	1464		1450	1453
$\delta_{\text{s}}(=\text{CH}_2)_{\text{vinyl}}$ (1)	1428	1426	1432	1430	1435
ν_{20} and ν_{29}	~1400	1404	1406	1399	1403
		1392			
ν_4	1373	1373	1374	1370	1373
$\delta_{\text{s}}(=\text{CH}_2)_{\text{vinyl}}$ (2)	1343	1343	1346	1338	1340
ν_{21} and $\delta(\text{CH}=\)_{\text{vinyl}}$	1305	1304	1303	1304	1309
$\nu(\text{C}-\text{O})_{\text{tyrosinate}}$	~1244	1245			
ν_{13}	~1236	1235	1235	1228	1228
$\nu_5 + \nu_{18}$	1213	1218	1215	1219	
$\nu_{30} + \nu(\text{C}_{\beta}-\text{C}_{\alpha}\text{vinyl})$	1176	1173	1174	1167	1170

TABLE I (continued)

			1155		
ν_{22}	1126	1126	1127	1125	1127
$\gamma(\text{CH=})_{\text{vinyl}} + \text{arom. d rings}$	1005	1007	1004	1001	1008
ν_{45}	984	991		983	
	964			970	
ν_{46}	936	940	940		
		871		868	
				854	
	828	830	830	820	
ν_6	792	795	790		806
ν_{16}	756	754	752	754 ^e	756
	719	724	722	718	722
ν_{47}	711	713		690	694
ν_7	676	678	678	676	675
	623	620			
ν_{48}	596	594			
ν_{49}	553	555	553	547	555
pyr fold		510	506	498	492
pyr fold		424	426	418	425
$\delta_{\text{C}_b\text{C}_\alpha\text{C}_\beta}$ (1)		414	416	406	415
$\gamma_{\text{C}_b\text{S}}$	384	386	385	380	380
$2\nu_{35}$					373
ν_8	346	348	348	351	345
$\delta_{\text{C}_b\text{C}_\alpha\text{C}_\beta}$ (2)			332	330	324

TABLE I (continued)

$\gamma_{m a}^{C C}$		303	308	315	312
ν_9	265	269	268	267	266
				250	
	242	237			
				222	
	206	203	207	200	
		190	190	192	

^aAssignments from references 40 and 41.

^bClFe^{III}(protoporphyrin IX) solid; 1 mg/300 mg KBr; spinning sample.

^cClFe^{III}(protoporphyrin IX) in aqueous NaOH solution; from reference 40.

^dprotein Raman spectra exhibit relatively stronger scattering at $\sim 1005 \text{ cm}^{-1}$ which is most likely due to contributions from amino acids bearing aromatic rings, particularly phenylalanine and tryptophan (42, 43); in model complexes, Raman intensity is less pronounced at this frequency.

^eAssignment according to reference 41; the ν_{16} mode following reference 40b is located at $\sim 722 \text{ cm}^{-1}$.

TABLE II
Characteristic Raman frequencies for ferric phenolates^a

Sample	Frequencies, cm^{-1} ^b				
	$\nu(\text{C}=\text{C})$	$\nu(\text{C}=\text{C})$	$\nu(\text{C}-\text{O})$	$\delta(\text{C}-\text{H})$	$\nu(\text{Fe}-\text{O})$
Non-heme iron proteins and model					
Serum transferrin	1613	1508	1288	1174	
Ovotransferrin	1605	1504	1270	1170	
Lactoferrin	1605	1505	1275	1175	
Purple uteroferrin	1603	1503	1285	1168	575
Purple acid phosphatase	1597	1497	1281	1164	575
Protocatechuate-3,4-O ₂ ase	1602	1503	1263	1171	
Fe(salen)OC ₆ H ₄ X	1603	1501	1272	1168	568
Heme proteins and models					
Hemoglobin M Boston	1607	1506	1278		603
Hemoglobin M Iwate	1605	1506	1310		589
Bovine liver catalase	1612		1244?		
<u>A. niger</u> catalase	1615		1245?		
<u>M. luteus</u> catalase	1610				
[Fe(TTOP)] ₂	1588		1298		623

^aSources of data: serum transferrin (52); ovotransferrin (53); lactoferrin (54); uteroferrin (55); acid phosphatase (56); protocatechuate-3,4-dioxygenase (57); Fe(salen)OC₆H₄X model complex (58); hemoglobins M (25); catalases and [Fe(TTOP)]₂ (this work).

^bAssignments based on normal mode calculations. Peak assigned to $\nu(\text{Fe-O})$ is coupled with a tyrosine ring mode (17).

FIGURE LEGENDS

Figure 1. Resonance Raman spectra of bovine liver catalase in the high frequency region. Conditions used are:

(A) Enzyme concentration of $\sim 220 \mu\text{M}$ in 0.05 M HEPES buffer, pH 7.0, excitation at 457.9 nm, 50 mW power at the sample, scan rate of $2 \text{ cm}^{-1} \text{ s}^{-1}$, 150° backscattering geometry, slit width of 5 cm^{-1} , at 4° C , $900\text{--}1600 \text{ cm}^{-1}$ region, total of 25 scans accumulated, and displayed with a 13-point smooth.

(B) Excitation of 488.0 nm, laser power of 55 mW at the sample Dewar, other conditions same as in (A).

(C) Sample concentration of $185 \mu\text{M}$ in 0.05 M HEPES, pH 7.01, excitation of 496.5 nm with a laser power of 100 mW at the sample. Other conditions identical to those in (A).

(D) Catalase concentration of $70 \mu\text{M}$ in 0.05 M HEPES buffer, pH 7.01, excitation of 514.5 nm with a laser power of 75 mW at the sample and a total of 12 scans collected using a 90° scattering geometry. Other conditions same as in (A).

(E) Concentration of $\sim 70 \mu\text{M}$ stock solution of bovine liver catalase, excitation of 568.2 nm with a laser power of 40 mW. Other conditions same as in (A).

Figure 2. Resonance Raman spectra of A. niger catalase in the high frequency range of $900\text{--}1600 \text{ cm}^{-1}$. Conditions used are:

(A) Catalase concentration of 55 μM in 0.05 M phosphate buffer, pH 7.0, room temperature, 90° scattering geometry at an excitation of 406.7 nm with a laser power of 25 mW at the sample, slit-width of 5 cm^{-1} , scan rate of $1\text{ cm}^{-1}\text{ s}^{-1}$, and a total of 9 scans displayed with a 5-point smooth.

(B) Catalase concentration of $\sim 300\text{ }\mu\text{M}$ in 0.05 M HEPES (pH 7.01), 4° C , 150° backscattering geometry, excitation of 457.9 nm with a laser power of 80 mW, scan rate of $2\text{ cm}^{-1}\text{ s}^{-1}$, slit width of 5 cm^{-1} , and a total of 59 scans displayed with a 17-point smooth.

(C) Concentration of $\sim 550\text{ }\mu\text{M}$ in 0.05 M HEPES (pH 7.01), excitation of 488.0 nm with a laser power of 125 mW, slit-width of 4 cm^{-1} with 65 scans. Other conditions same as in (B).

(D) Concentration of $\sim 340\text{ }\mu\text{M}$ in above HEPES, excitation of 514.5 nm, laser power of 110 mW and 37 scans. Other conditions are identical to those in (C).

Figure 3. Resonance Raman spectra of M. luteus catalase in the region of $900\text{--}1600\text{ cm}^{-1}$. Conditions used are:

(A) Concentration of catalase $\sim 200\text{ }\mu\text{M}$ in 0.05 M Tris/HCl (pH 9.0) containing 0.05 M CN^- , excitation of 514.5 nm with a laser power of 35 mW, room temperature, 90° scattering geometry, slit-width of 5 cm^{-1} , scan rate of

$1 \text{ cm}^{-1} \text{ s}^{-1}$, 4 scans accumulated, and displayed with a 13-point smooth.

(B) Catalase concentration of $\sim 35 \mu\text{M}$ in 0.1 M phosphate buffer (pH 7.0), polarization of the scattered light parallel (||) to that of the incident light, with a total of 25 scans. Other conditions identical to those in (A).

(C) Polarization of the scattered light perpendicular (\perp) to that of the incident light. Other conditions identical to those in (B); a = anomalously polarized, d = depolarized, p = polarized.

Figure 4. Resonance Raman spectra of M. luteus catalase, A. niger catalase, and ClFe^{III} (protoporphyrin IX) (hemin chloride) in the low frequency region.

(A) M. luteus catalase, concentration of $\sim 110 \mu\text{M}$ in 0.05 M phosphate buffer (pH 7.0), 150° backscattering geometry, 4° C , excitation of 406.7 nm with a laser power of 45 mW at the sample, scan rate of $1 \text{ cm}^{-1} \text{ s}^{-1}$, slit-width of 5 cm^{-1} , with total scans of 16, and displayed with a 5-point smooth.

(B) A. niger catalase, concentration of $\sim 55 \mu\text{M}$ in 0.05 M phosphate buffer (pH 7.0), 90° scattering geometry, laser power of 25 mW at the sample in a capillary, room temperature, with total scans of 9, and displayed with a 17-point smooth. Other conditions same as in (A).

(C) $\text{ClFe}(\text{III})\text{PPIX}$ (hemin chloride) as solid in KBr ($\sim 1 \text{ mg}$

of hemin chloride per 300 mg KBr), excitation of 457.9 nm, room temperature, 150° backscattering geometry, laser power of 40 mW at the sample, slit-width of 6 cm⁻¹, scan rate of 1 cm⁻¹ s⁻¹, with total scans of 9, and using a 21-point smooth.

Figure 5. Resonance Raman spectra comparing bovine liver catalase with ClFe^{III}protoporphyrin IX dimethylester. Conditions used are:

(A) Bovine liver catalase, concentration of 220 μM in 0.05 M HEPES (pH 7.01), excitation of 457.9 nm, laser power of 50 mW at the sample in a capillary, 4° C, 150° backscattering geometry, slit-width of 5 cm⁻¹, scan rate of 1 cm⁻¹ s⁻¹, 25 scans and 13-point smooth.

(B) ClFe(III)protoporphyrin IX dimethylester [ClFe(III)PPIXDME], concentration ~2 mg/mL CS₂, excitation of 457.9 nm with a laser power of 75 mW at the sample in a capillary, slit-width of 6 cm⁻¹, scan rate of 2 cm⁻¹ s⁻¹, total scans of 19 and a 17-point smooth.

(C) Bovine liver catalase, excitation of 488.0 nm, laser power of 55 mW at the sample, scan rate of 2 cm⁻¹ s⁻¹. Other conditions same as in (A).

(D) ClFe(III)PPIXDME, concentration of ~1 mg/mL CS₂, excitation of 488.0 nm with a laser power of 65 mW, slit-width of 4 cm⁻¹, a total of 25 scans and a 21-point smooth. Other conditions similar to those in (B).

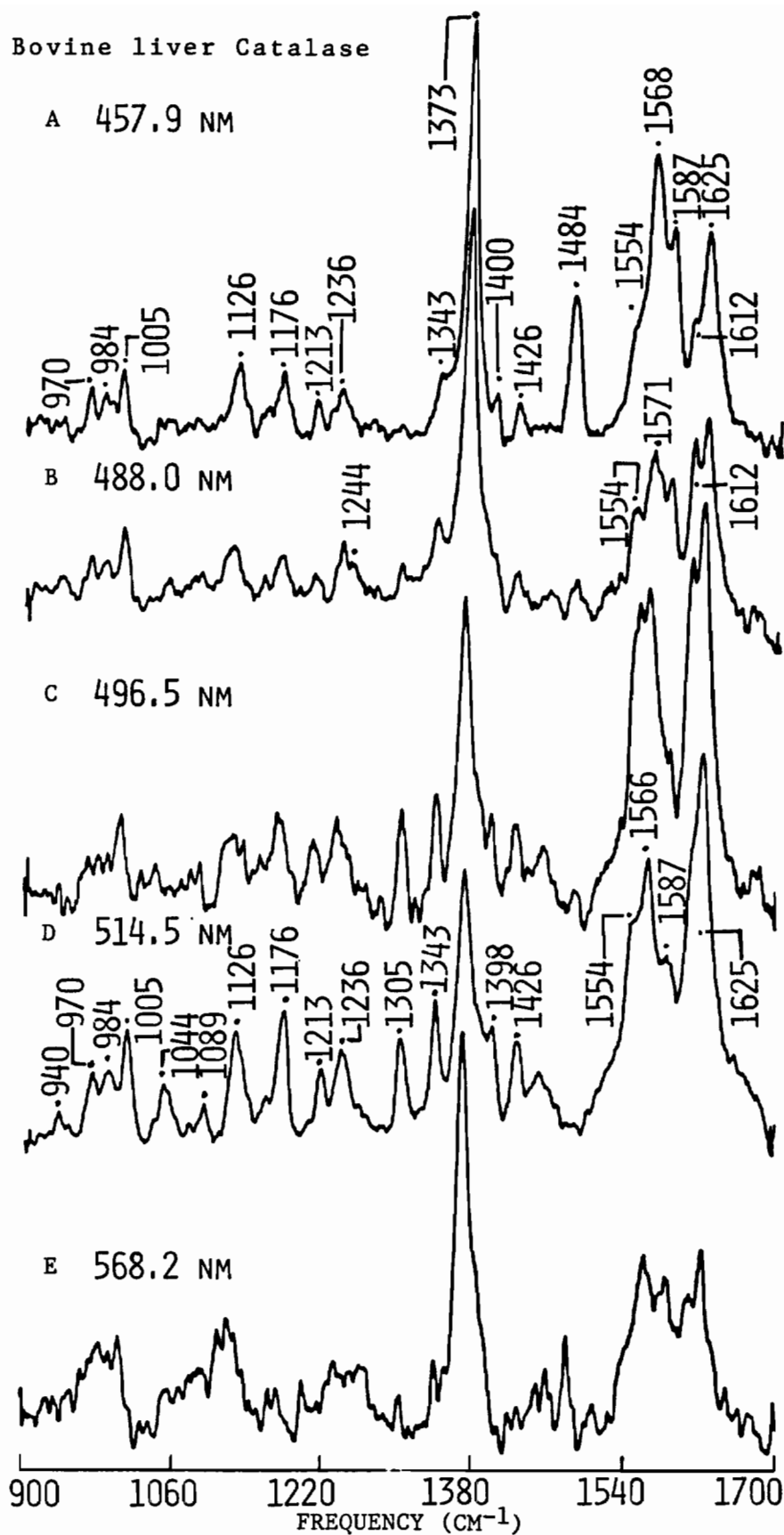


FIGURE 1

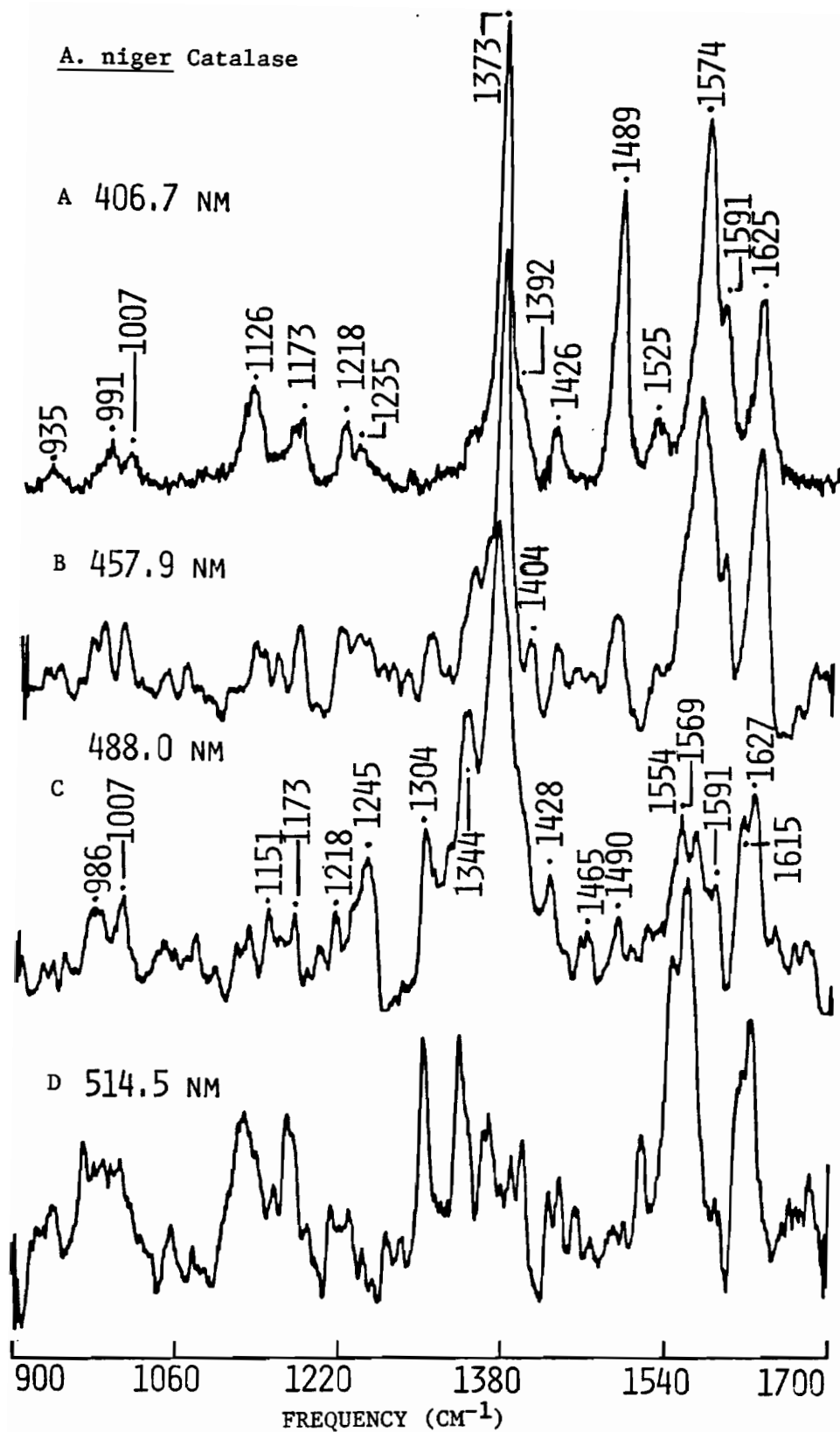


FIGURE 2

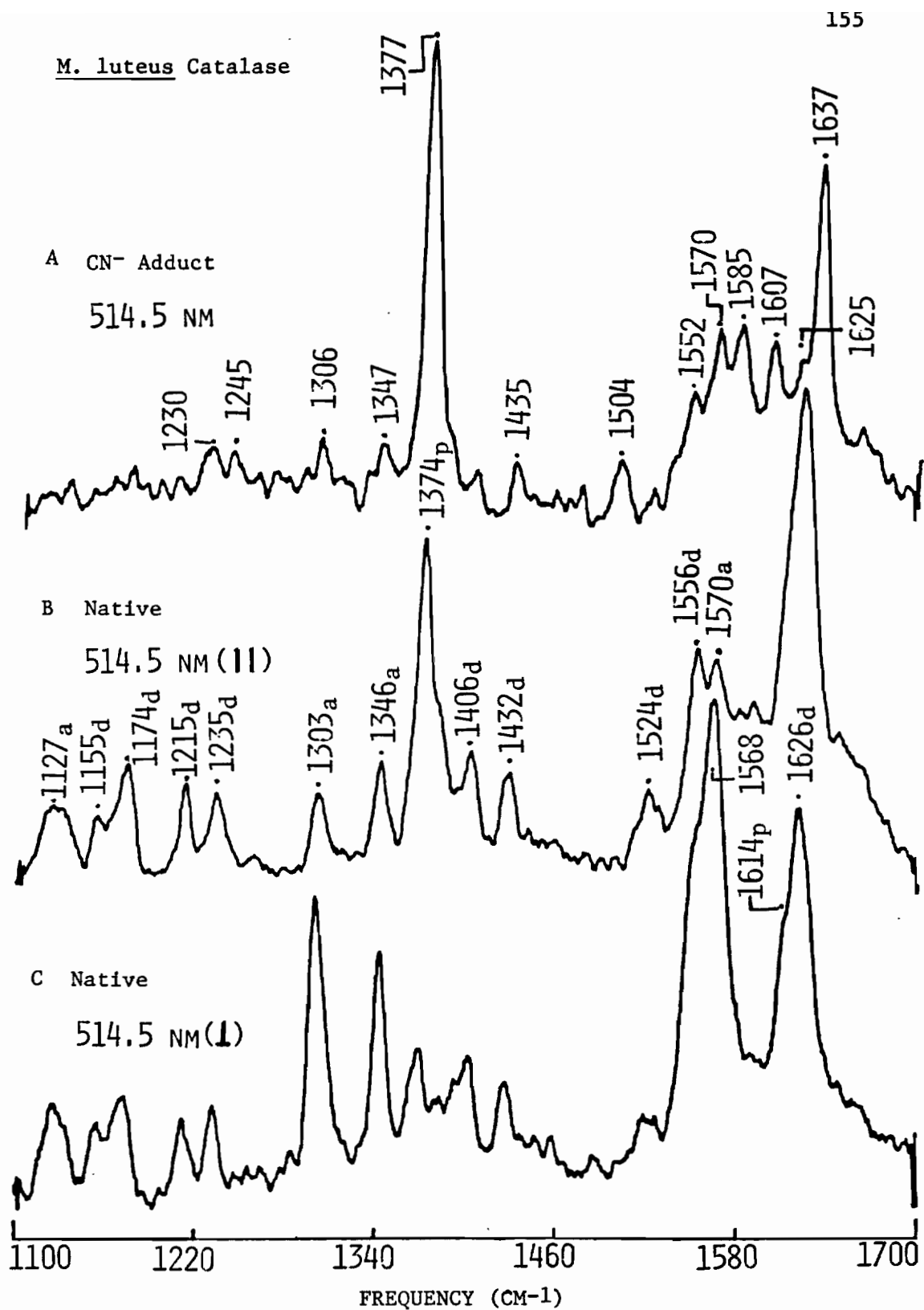


FIGURE 3

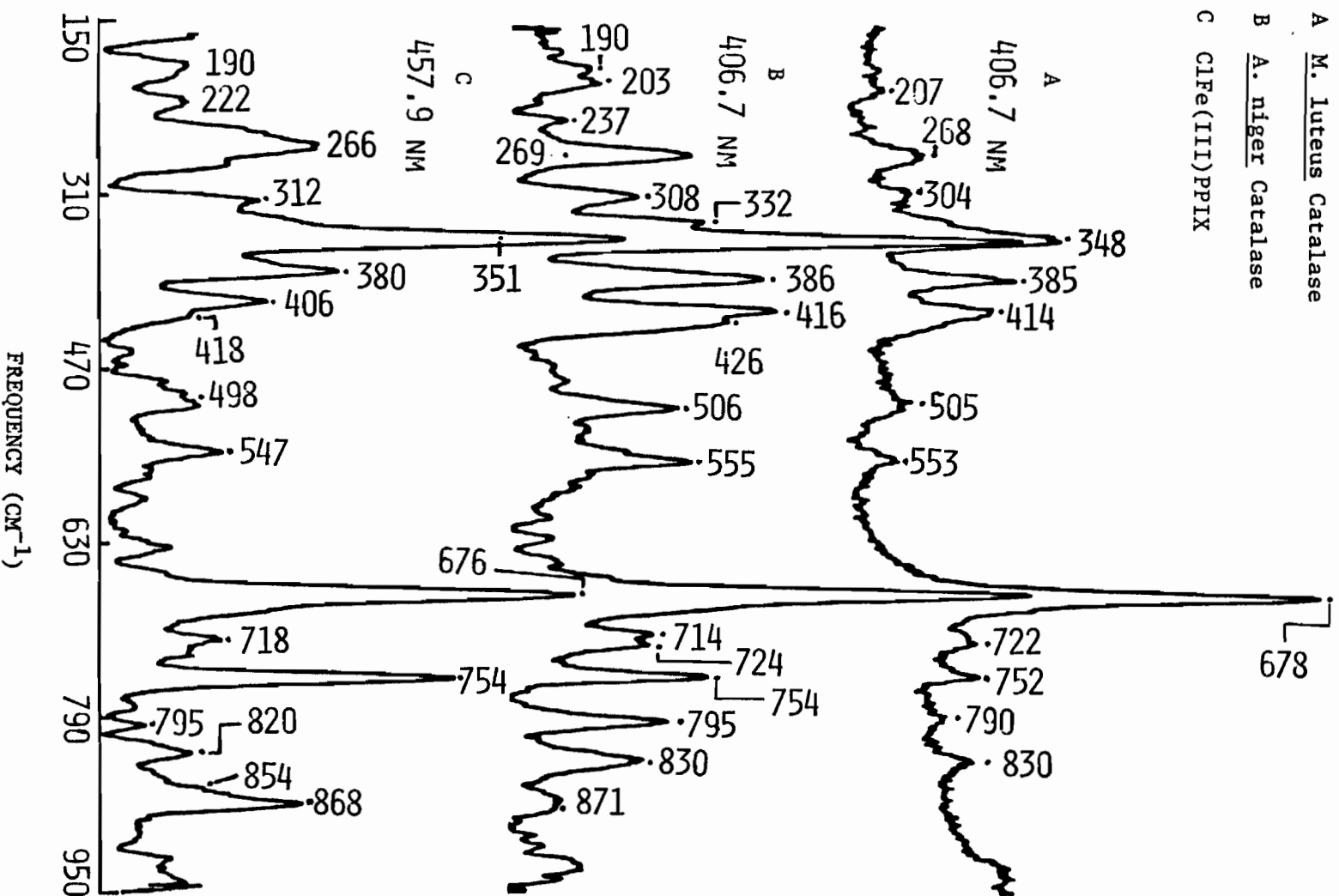


FIGURE 4

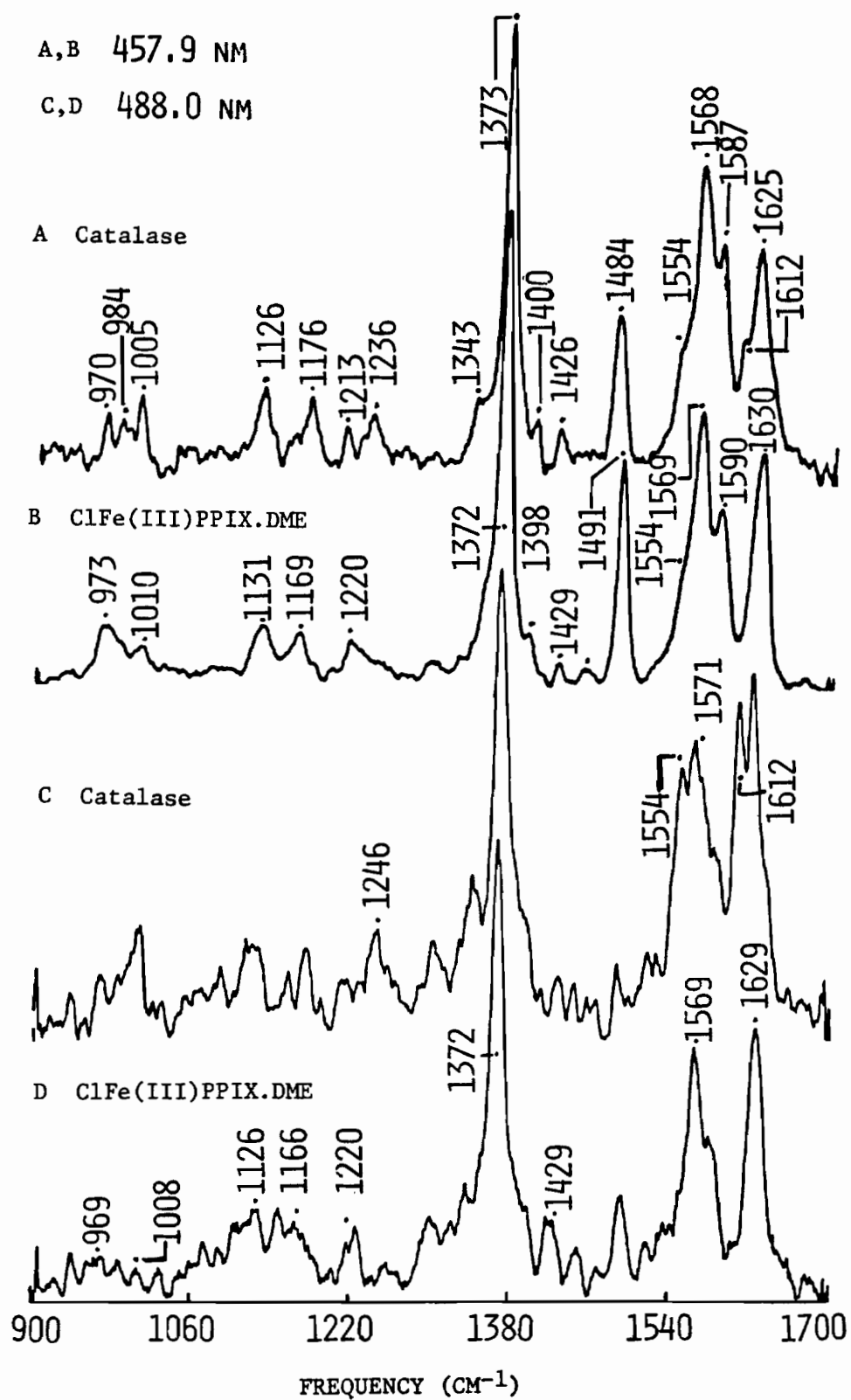


FIGURE 5

CHAPTER VI

RESONANCE RAMAN SPECTRA OF 5-(2-HYDROXYPHENYL)-10,15,20-(TRITOLYL) IRON(III)PORPHYRIN AND ITS DIMERIC COMPLEXES

INTRODUCTION

Recently a new class of iron-tyrosinate proteins and enzymes ranging from purple acid phosphatases, transferrins, catechol dioxygenases to catalases and mutant hemoglobins has emerged and has been a subject of extensive active research. The iron centers of these proteins and enzymes show similar spectroscopic properties which can be attributed mostly to the tyrosinate coordination. Experimental evidence for the tyrosinate ligation comes mainly from X-ray crystallography, absorption, and resonance Raman spectroscopy. The absorption spectra of iron-tyrosinate proteins in general show maxima around 400-600 nm resulting from tyrosinate to iron charge transfer. Resonance Raman (rR) spectroscopy has been widely used as an effective means to elucidate the coordination of tyrosinate to ferric iron in various metalloproteins (1). When excited into the tyrosinate to iron (III) charge transfer region, four resonance enhanced vibrational modes characteristic of these proteins/enzymes are observed at frequencies of 1600, 1500, 1270 and 1170 cm^{-1} . Normal coordinate analysis on the model complexes of metal-tyrosine

proteins (2) has made it possible to assign the peaks at 1600 and 1500 cm^{-1} as phenolate $\nu(\text{C}=\text{C})$, and those at 1270 and 1170 cm^{-1} as phenolate $\nu(\text{C}-\text{O})$ and $\delta(\text{C}-\text{H})$, respectively. In addition to these, another spectral feature at around 570 cm^{-1} (observed from 550–620 cm^{-1}) has also been noted for metal-tyrosinate proteins (3). Based on the shifts due to isotopic substitution on the model complexes, this peak has been assigned as $\nu(\text{Fe}-\text{O})$ (4).

To gain better insight into the active centers of iron-tyrosinate proteins and enzymes in biological systems, numerous efforts have been made to model them (5–7). In such an attempt to mimic the active site structure of iron tyrosinate proteins and enzymes, Goff and coworkers (University of Iowa) synthesized a phenolate-bridged dimer of 5-(2-hydroxyphenyl)-10,15,20-(tritolyl) iron(III)porphyrin complex* [(TTOPH)Fe Cl] (8). On the basis of the magnetic moment measurements (solid and solution states), the iron in both the monomer and the dimer were found to be high spin. In both the complexes, the ferric iron is pentacoordinated and is bonded to the four nitrogens of the pyrrole rings of the porphyrin moiety. The fifth coordination position is filled by a chloride ion in the monomer and by an oxygen of the phenolate group (from a second

*The abbreviations used are: Monomer is 5-(2-hydroxyphenyl)-10,15,20-(tritolyl)Fe(III)Cl abbreviated as (TTOPH)FeCl and the respective dimer is abbreviated as [(TTOP)Fe]₂; TetraphenylFe(III)Cl, μ -oxo and μ -nitrido dimers of tetraphenylporphyrinFe(III) complexes are abbreviated as (TPP)FeCl, [(TPP)Fe]₂O and [(TPP)Fe]₂N respectively.

monomer) in the dimer. The dimer is composed of an intermolecular phenolate doubly bridged Fe(III) complex having the structure shown in Figure 1. X-ray crystallographic measurement of the dimer (8) showed the iron-oxygen distance to be 1.847 Å which is reasonably close to those for other iron(III) phenolate complexes (2, 6). The coordination sphere of iron (III) of $[(\text{TTOP})\text{Fe}]_2$ resembles that of catalase in that the iron is high spin and pentacoordinated. Whereas catalase has a coordinated phenolate oxygen from tyrosine, the dimer has a phenolate oxygen (from a phenol ring) as the fifth ligand. This aspect of the structure attracted our attention and led us to study the vibrational spectra of the dimer and monomer, respectively, using the former as a model system for catalase, which is known to contain a phenolate-linked high spin heme (Chapter V). Further, we wanted to explore the low frequency vibrational spectra of the dimer for evidence, identification and location of metal-ligand vibrational modes, i.e., $\nu(\text{Fe-O})$, and to compare them to those of catalase and other phenolate complexes.

In this chapter, we present the assignments of the rR bands observed for the monomer $(\text{TTOPH})\text{FeCl}$ and the dimer $[(\text{TTOP})\text{Fe}]_2$. These assignments also include tentative assignment for phenolate peaks of the dimer at ~ 1588 and 1298 cm^{-1} and possible $\nu(\text{Fe-O})$ at 623 cm^{-1} . Some of the rR bands related to the phenolate vibrational modes are apparently buried underneath the intense vibrational peaks due to tetraphenylporphyrin moiety and, thus, are not distinct. These results establish that the vibrational spectra of $[(\text{TTOP})\text{Fe}]_2$ are a combination of vibrational modes due to tetraphenylporphyrin

and those due to the phenolate ligand. Hence it resembles that of catalase in which the vibrational modes are due to the porphyrin moiety and the tyrosinate ligand on Fe(III) (see chapter on catalase for details).

MATERIALS AND METHODS

The dark colored solid samples of the monomer and the dimer were a gift of Dr. Harold Goff (8). Both samples were used without further purification. The concentrations of the dimer and the monomer used were 4 $\mu\text{g/mL}$ and 38 $\mu\text{g/mL}$ in toluene, respectively, as determined from the absorption spectra. Resonance Raman spectra of the samples were obtained in solid as well as in solution states. 2 mg of the monomer and 1 mg of the dimer were mixed separately with 100 mg of KBr (Harshaw Chemical Co.) and ground by hand with a mortar and pestle for about 5 minutes. The ground mixture was then packed firmly into a stainless steel spinning sample holder using a tamper (Fig. 2 in Chapter II). The scattered light was collected in a 150° back-scattering geometry at room temperature. For polarization studies on solutions (respective concentrations of the monomer and the dimer were 0.5 mg/mL and 1.0 mg/mL in CS_2), scattered light after passing through an analyzer and a scrambler was collected in a 90° scattering geometry. The excitation was provided by a Spectra-Physics Argon ion laser (164-05). A Jarrell-Ash spectrophotometer interfaced to a computer, an ORTEC model amplifier/discriminator and a cooled RCA C31034A photomultiplier tube cooled to -25°C were part

of the equipment (9) used for data collection with an upgraded computer system described recently (10). A Perkin-Elmer Model 1800 FTIR instrument was used to obtain IR spectra from KBr pellet samples.

RESULTS AND DISCUSSION

The optical spectra of the monomer and the dimer (Fig. 2) correspond to their respective literature values (8). Further, they are also similar to those of literature values of Cl(TPP)Fe(III) (11) and dimeric hydroquinone complex of TPPFe(III), respectively, (12). Both of the samples exhibit spectral features characteristic of pentacoordinated high spin Fe(III)tetraphenylporphyrin complexes at 335-380, 415-420, 555-575, and ~650 nm. Although the coordination sphere of the dimer complex [(TTP)Fe]₂ resembles the active site of catalase, the absorption spectrum of the dimer is quite different from that of catalase. This difference may be accounted by the differences in the substituents of the porphyrin moiety.

The rR spectra of both the monomer and the dimer were obtained with 457.9, 488.0, and 514.5 nm excitations. The spectra in the region $>900\text{ cm}^{-1}$ of the monomer as well as the dimer as solids are presented in Figures 3 and 4; their low frequency spectra are displayed in Figure 5.

Analysis and assignments of various vibrational modes of the monomer and the dimer were made on the basis of comparison with those of literature values of Fe(III)tetraphenylporphyrin, the μ -oxo and

μ -nitrido bis-tetraphenylFe(III)porphyrin complexes (13-16). Since $[(\text{TTOP})\text{Fe}]_2$ is a tetraaryl iron(III) porphyrin complex with a phenolate bridge, we expected its vibrational properties to be closer to μ -oxo dimer of TPPFe(III) complex than to μ -nitrido dimer complex of Fe(III)TPP . Such a comparison is shown in Table I. Furthermore, in order to find out the extra peaks in dimer with respect to monomer, their rR spectra are compared as shown in Figures 3, 4, and 5.

As is evident from Table I, most of the spectral features of $[(\text{TTOP})\text{Fe}]_2$ are very similar to those of $[(\text{TPP})\text{Fe}]_2\text{O}$ as expected, since both of them have a ferric high-spin pentacoordinated iron with a tetraphenylporphyrin. In the high frequency region, the vibrational peaks are representative of ferric high spin tetraphenylporphyrin and are much closer to those of $[(\text{TPPFe})_2\text{O}]$ in frequencies than those of $[(\text{TPPFe})_2\text{N}]$. This again is not surprising because the latter has been found to have low spin Fe(III) (16). The spectral features that are different from μ -oxo dimer and μ -nitrido dimer can be attributed to the difference either in the type of aryl group present in the meso positions of the porphyrin moiety or in the coordination of the fifth ligand.

Comparing the rR spectral features of $(\text{TTOPH})\text{FeCl}$ with those of $[(\text{TTOP})\text{Fe}]_2$ a very close correspondence of their frequencies due to the tetraphenyl moieties are seen. Exceptions are three extra peaks at 1588, 1298 and 1112 cm^{-1} in the high frequency region and four extra peaks at 289, 623, 663, and 904 cm^{-1} in the low-frequency region of the dimer. All of these peaks are intensified with

488.0-nm excitation. The peaks at 1588, 1298, 904, 623, and 289 cm^{-1} are all of medium intensity and that at 1108 cm^{-1} is weak. Further, on analyzing the rR data of the dimer, these bands are found to have no counterparts in the rR spectra of $[(\text{TPP})\text{Fe}]_2\text{O}$ and $[(\text{TPP})\text{Fe}]_2\text{N}$. Since these peaks could not be accounted for and they are unique to $[(\text{TTOP})\text{Fe}]_2$, their appearance is most likely explained as due to phenolate ligation of Fe(III) in this dimer. Polarization measurements were also carried out on the solutions of both monomer and dimer (data not shown), but they were not satisfactory enough to give a conclusive result on the depolarization ratios of the weaker vibrational modes. The intensity enhancement of all the peaks unique to $[(\text{TTOP})\text{Fe}]_2$ follow the same pattern: they are less intense in solution than in the solid state.

The unique 1588- cm^{-1} band of $[(\text{TTOP})\text{Fe}]_2$ was found to be polarized. For various ferric phenolate proteins and complexes structural features in the frequency region of 1600 and 1500 cm^{-1} have been assigned as due to phenolate $\nu(\text{C}=\text{C})$ (1 and references therein). Since the fifth ligand of Fe(III) in $[(\text{TTOP})\text{Fe}]_2$ is a phenolate oxygen and an extra peak at 1588 cm^{-1} is seen in the proper region, we assign it as $\nu(\text{C}=\text{C})$. The intensity of the distinct medium intensity spectral feature at 1298 cm^{-1} for $[(\text{TTOP})\text{Fe}]_2$ decreases in solution, so that no reliable depolarization ratio could be determined. For numerous ferric phenolate proteins and complexes, a band in the region of 1260-1310 cm^{-1} has been observed and assigned as $\nu(\text{C}-\text{O})(\text{phenolate})$. We suggest that the 1298- cm^{-1} band corresponds to this $\nu(\text{C}-\text{O})$ mode.

Another peak characteristic of phenolate proteins and complexes has been observed at 1170 cm^{-1} that has been assigned as $\delta(\text{C-H})$ of the coordinated phenolate. However, a peak at $\sim 1186\text{ cm}^{-1}$ is present in the rR spectra of $(\text{TTOPH})\text{FeCl}$ as well as $[(\text{TTOF})\text{Fe}]_2$, suggesting that this peak is probably not due to phenolate $\delta(\text{C-H})$. Alternatively, a small spectral feature at $\sim 1112\text{ cm}^{-1}$ in the dimer (which has no counterpart in the monomer) appears consistently with near Soret and visible excitations. It is possible that it is the phenolate $\delta(\text{C-H})$, but it would be at a comparatively low frequency.

Fe(III) -tyrosinate proteins and typical model complexes have two strong features due to phenolate ring vibrations around 1600 and 1500 cm^{-1} . Although the 1588-cm^{-1} band in the dimer $[(\text{TTOF})\text{Fe}]_2$ very likely corresponds to the 1600 cm^{-1} peak, we could not locate the other peak. It is possible that the expected peak at $\sim 1500\text{ cm}^{-1}$ is masked by the presence of $\nu(\text{C}_\alpha\text{-C}_m)$ of the porphyrin ring in that region. In catalase (Chapter V), we also observed the $\sim 1600\text{-cm}^{-1}$ mode but not the 1500-cm^{-1} companion. This observation matches the data of Nagai *et al*, in whose study of Hb M, the 1500-cm^{-1} band was also of lower intensity. We suggest that the low intensity of the lower $\nu(\text{C=C})$ mode is a consequence of the heme moiety common in all these systems. In addition, we were only able to locate the $\nu(\text{C-O})$ phenolate vibrational mode at 1298 cm^{-1} of the two lower frequency bands characteristic of phenolate coordination. This pattern was also observed in our study of catalase and, thus, may be a similar feature of heme versus non-heme tyrosinate coordination.

In the low frequency region, four new peaks appear for $[(\text{TTOP})\text{Fe}]_2$ at 904, 663, 623, and 289 cm^{-1} . The peak at 904 cm^{-1} is of medium intensity and is maximally resonance enhanced with excitation at 488.0 nm; it follows the same excitation behavior as do the other peaks unique to $[(\text{TTOP})\text{Fe}]_2$. This peak disappears in solution spectra. The presence of the other low frequency peaks could not be verified in the solution spectra since these regions were dominated by solvent peaks. The peaks at 623 and 663 cm^{-1} in the rR spectra of $[(\text{TTOP})\text{Fe}]_2$ have no counterpart in the spectra of $(\text{TTOPH})\text{FeCl}$, $(\text{TPPFe})_2\text{O}$, and $(\text{TPPFe})_2\text{N}$, and follow the same enhancement pattern. This leads to the suggestion that these peaks in the dimer spectra could be due to $\nu(\text{Fe-O})$. However, most of the Fe-O stretches for model complexes such as $(\text{Salen})\text{Fe}(\text{OC}_6\text{H}_4\text{CH}_3)$ have been found to lie at $\sim 570 \text{ cm}^{-1}$. The higher frequency for $[(\text{TTOP})\text{Fe}]_2$ may relate to the short Fe-O bond lengths of 1.85 Å. Unfortunately, no reliable polarization data could be obtained for these peaks in solution that would have assisted in their assignments. Finally the peak at 289 cm^{-1} for $[(\text{TTOP})\text{Fe}]_2$ is seen distinctively only with 488.0-nm excitation; it also has no counterparts in the rR spectra of $(\text{TTOPH})\text{FeCl}$, or the μ -oxo dimer and μ -nitrido dimer of $\text{Fe}^{\text{III}}\text{TPP}$.

Comparison of the IR spectral frequencies of the monomer and the dimer shows close correspondence with those of their respective rR spectra. This observation indicates that the molecular symmetries of both the monomer and the dimer complexes are quite low. In the crystal structure determination of $[(\text{TTOP})\text{Fe}]_2$, there was ambiguity regarding the space group, $\text{Pmna}(D_{2h}^7)$ or $\text{P2na}(C_{2v}^6)$ (8). The absence

of mutual exclusion in the vibrational spectroscopic data supports the lower symmetry identification. Furthermore, C_2 and C_1 site symmetries of C_{2v}^6 are both fully allowed in IR and Raman spectroscopy.

However, comparison of the IR spectra of the monomer and the dimer to each other shows definitive alterations in the band pattern and intensities in the 350–400, 500–700, 850–950, 1250–1400, and 1550–1650 cm^{-1} regions (Fig. 6). In addition, the IR spectrum of the dimer reveals new bands of medium intensity at 1587, 1385, 901, 661, and 622 cm^{-1} which are absent from the IR spectrum of the monomer. Furthermore, The IR frequencies at 1587, 901, 661, and 622 cm^{-1} correspond to the rR peaks at 1588, 904, 663, and 623 cm^{-1} . The observation of these extra peaks in the IR spectrum of the dimer versus monomer supports and strengthens our assignments.

The new IR band at 1385 cm^{-1} is not seen in rR data, although this region is not obscured by other Raman features. However, the rR band observed at $\sim 1298 \text{ cm}^{-1}$ in the dimer, although not resolved as an individual band in the IR, lies in a region of significantly increased intensity relative to the spectrum of the monomer (Fig. 6). This suggests that the unique $\sim 1295\text{-cm}^{-1}$ band is present in both the IR and Raman data of the dimer complex as a feature characteristic of phenolate coordination.

In conclusion, vibrational spectroscopic studies on $[(\text{TTOP})\text{Fe}]_2$ show that it acts as a relevant model for catalase. Both catalase (Chapter V) and $[(\text{TTOP})\text{Fe}]_2$ exhibit intense rR peaks reminiscent of the porphyrin moiety along with less intense peaks assignable to

phenolate ligation to the ferric iron. The observation of lesser number of peaks due to phenolate vibrational modes and of their diminished intensity seems to be specific to heme systems in heme-proteins and their model complexes. Hence they differ from non-heme iron-tyrosinate proteins which show intense peaks due to phenolate-related vibrational modes.

REFERENCES

1. Que, Jr., L. (1988) in Biological Applications of Raman Spectroscopy (Spiro, T. G., ed., Wiley) Vol. 3, 491-521
2. Tomimatsu, Y., Kint, S., and Scherer, J. R. (1976) Biochemistry 15, 4918-4924
3. Nagai, K., Kagimoto, T., Hayashi, A., Taketa, F., and Kitagawa, T. (1983) Biochemistry 22, 1305-1311
4. Pyrz, J. W., Roe, A. L., Stern, L. J., and Que, L., Jr. (1985) J. Am. Chem. Soc. 107, 614-620
5. (a) Heistand II, R. H., Roe, A. L., and Que, L., Jr. (1982) Inorg. Chem. 21, 676-681
(b) Heistand II, R. H., Lauffer, R. B., Fikrig, E., and Que, L., Jr. (1982) J. Am. Chem. Soc. 104, 2789-2896
6. Koch, S. A., and Millar, M. (1982) J. Am. Chem. Soc. 104, 5255-5257
7. Ainscough, E. W., Addison, A. W., Dolphin, D., and James, B. R. (1978) J. Am. Chem. Soc. 100, 7585-7591
8. Goff, H. M., Shimomura, E. T., Lee, Y. J., and Scheidt, W. R. (1984) Inorg. Chem. 23, 315-321
9. Loehr, T. M., Keyes, W. E., and Pincus, P. A. (1979) Anal. Biochem. 96, 456-463
10. Mino, Y., Wariishi, H., Blackburn, N. J., Loehr, T. M., and Gold, M. H. (1988) J. Biol. Chem. 263, 7029-7036
11. Fleischer, E. B., Palmer, J. M., Srivastava, T. S., Chatterjee, A. (1971) J. Am. Chem. Soc. 93, 3162-3167

12. Kessel, S. L., and Hendrickson, D. N. (1980) Inorg. Chem. **19**,
1883-1889
13. Burke, J. M., Kincaid, J. R. and Spiro, T. G. (1978) J. Am.
Chem. Soc. **100**, 6077-6083
14. Stein, P., Ulman, A., and Spiro, T. G. (1984) J. Phys. Chem. **88**,
369-374
15. Schick, G. A., and Bocian, D. F. (1980) J. Am. Chem. Soc. **102**,
7982-7984
16. Schick, G. A., and Bocian, D. F. (1983) J. Am. Chem. Soc. **105**,
1830-1838

TABLE I

Resonance Raman Frequencies (cm^{-1}) and Assignments for (TTOPH)FeCl,
 [(TTOP)Fe]₂, (TPPFe)₂O^a and (TPPFe)₂N^b Complexes

(TTOPH)FeCl	[(TTOP)Fe] ₂	(TPPFe) ₂ O	(TPPFe) ₂ N	Assignments
1612	1614	1599	1599	Phenyl
n.o.	1588 [*]	n.o.	n.o.	New band
1575	1574	1561	1567	ν_{11}
1553	1552	1553	1567	ν_2
1516	1518	1511	1538	ν_{20}
1498	1499	1495	1506	ν_{12}
1451	1451	1450	1450	ν_3
n.o.	n.o.	1368	1374	-
1366	1365	1359	1367	ν_4
1338	1335	1333	1342	ν_{21}
n.o.	1298 [*]	n.o.	n.o.	New band
1273	1274	1271	1270	ν_{13}
1237	1234	1237	1235	$\nu(\text{C}_m\text{-Ph})$
1187	1186	n.o.	1188	n.a.
n.o.	1112 [*]	n.o.	n.o.	New band
n.o.	n.o.	1087	1088	ν_{15}
1082	1081	1083	1080	ν_5
n.o.	1037	1030	1030	Phenyl
1017	1018	1014	1012	ν_{31}

(Continuation of Table I)

1002	1005	1004	1004	ν_6
1001	1003	995	996	Phenyl
n.o.	904 [*]	n.o.	n.o.	New band
891	887	886	886	ν_7
843	847	848	846	ν_{16}
714	718	719 ^b	718	n.a.
c	663	n.o.	n.o.	New band
c	n.o.	640	640	Por.def.
n.o.	623 [*]	n.o.	n.o.	New band
572	578	571 ^b	571	n.a.
n.o.	n.o.	n.o.	424	$\nu(\text{Fe-N-Fe})$
388	390	390	386	Por.def.
n.o.	n.o.	363	n.o.	$\nu(\text{Fe-O-Fe})$
n.o.	n.o.	330 ^b	336	n.a.
n.o.	289 [*]	n.o.	n.o.	New band
253	256	257	257	n.a.
d.n.o.	d.n.o.	n.o.	252	n.a.
d.n.o.	d.n.o.	195	194	n.a.
d.n.o.	d.n.o.	195	195	n.a.

^aTaken from reference 13, 14 unless otherwise stated, ^bTaken from reference 15, ^cIn the noise level, n.o.= not observed, n.a.= not assigned, d.n.o.= data not obtained, Por.def.= porphyrin deformation

FIGURE LEGENDS

Figure 1. Structure of dimer of 5-(2-hydroxyphenyl)-10,15,20-(tritolyl)Fe(III)porphyrinato complex taken from reference 8. ORTEP plot of the $[(\text{TTOP})\text{Fe}]_2$ molecule showing overlap between the porphinato cores. The plane of the drawing is the N_4 plane of the heavy-lined core. The symmetry-unique portion of the molecule is drawn with heavy bonds and the position of the crystallographically required twofold axis is displayed. The drawing is contoured at the 50% probability level.

Figure 2. Electronic absorption spectra of (a) $(\text{TTOP})\text{FeCl}$ and (b) $[(\text{TTOP})\text{Fe}]_2$ in toluene. Respective concentrations are $38 \mu\text{g/mL}$ and $4 \mu\text{g/mL}$.

Figure 3. High frequency spectra of the monomer and the dimer in the solid states in a spinning sample holder with 150° back-scattering geometry, an excitation of 457.9 nm at room temperature with a slit-width of 5 cm^{-1} , a scan rate of $1 \text{ cm}^{-1} \text{ s}^{-1}$ and a laser power of 40 mW with multiple scans.

A. Dimer (1 mg/100 KBr).

B. Monomer (1 mg/50 KBr).

Figure 4. High frequency spectra of the dimer (A) and the monomer (B) as solids with an excitation of 514.5 nm and a laser

power of 100 mW at the samples. Other conditions are same as in Figure 3.

Figure 5. Low frequency spectra of the dimer (A) and the monomer (B) as solids with an excitation of 488.0 nm excitation, a laser power of 70 mW at the samples. Other conditions same as in Figure 3.

Figure 6. IR spectra of the dimer (A) and the monomer (B) as solids in KBr pellets. Cumulative scans of 10 each. Concentrations were ~1 mg/100 mg KBr.

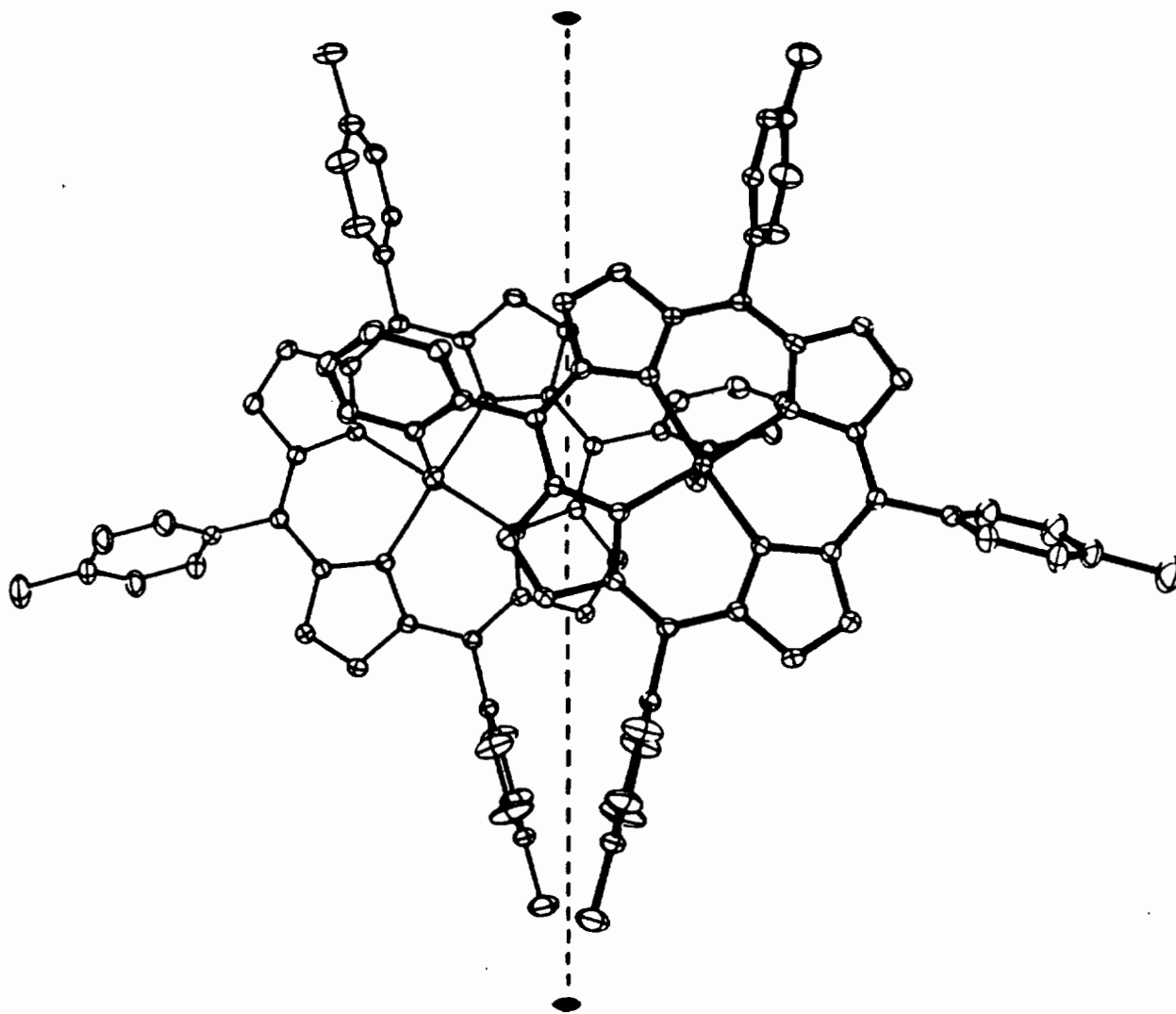


FIGURE 1

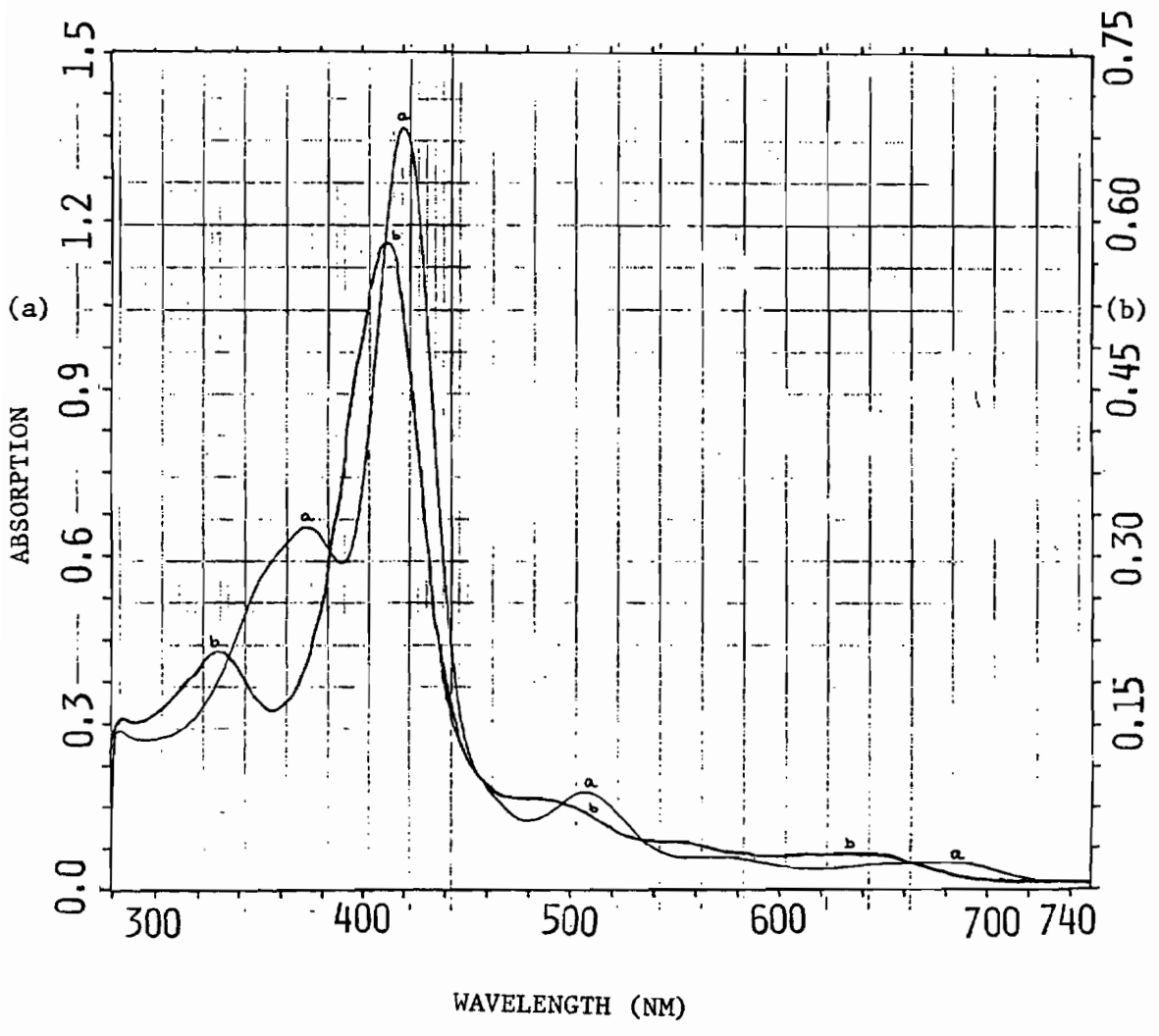


FIGURE 2

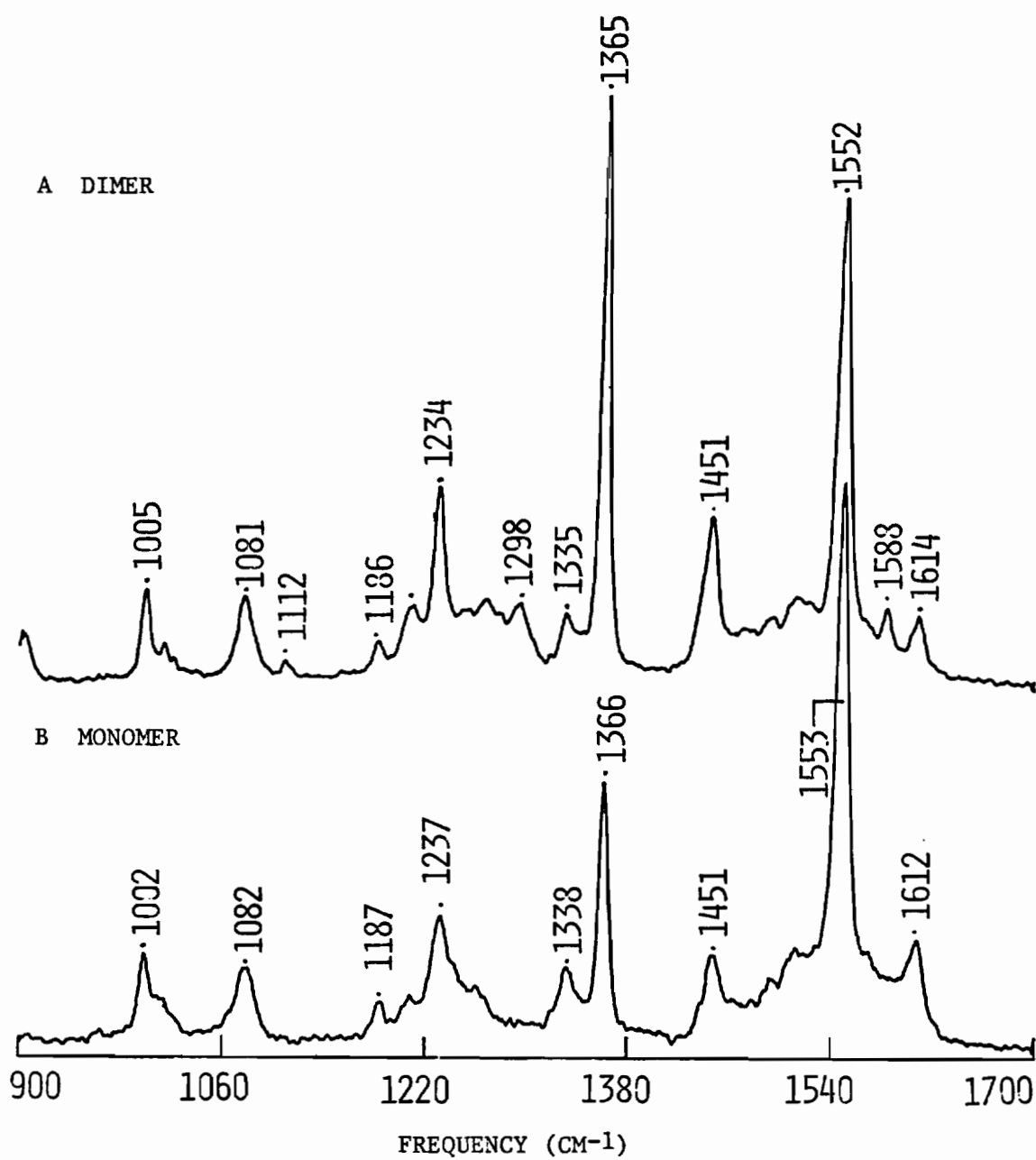


FIGURE 3

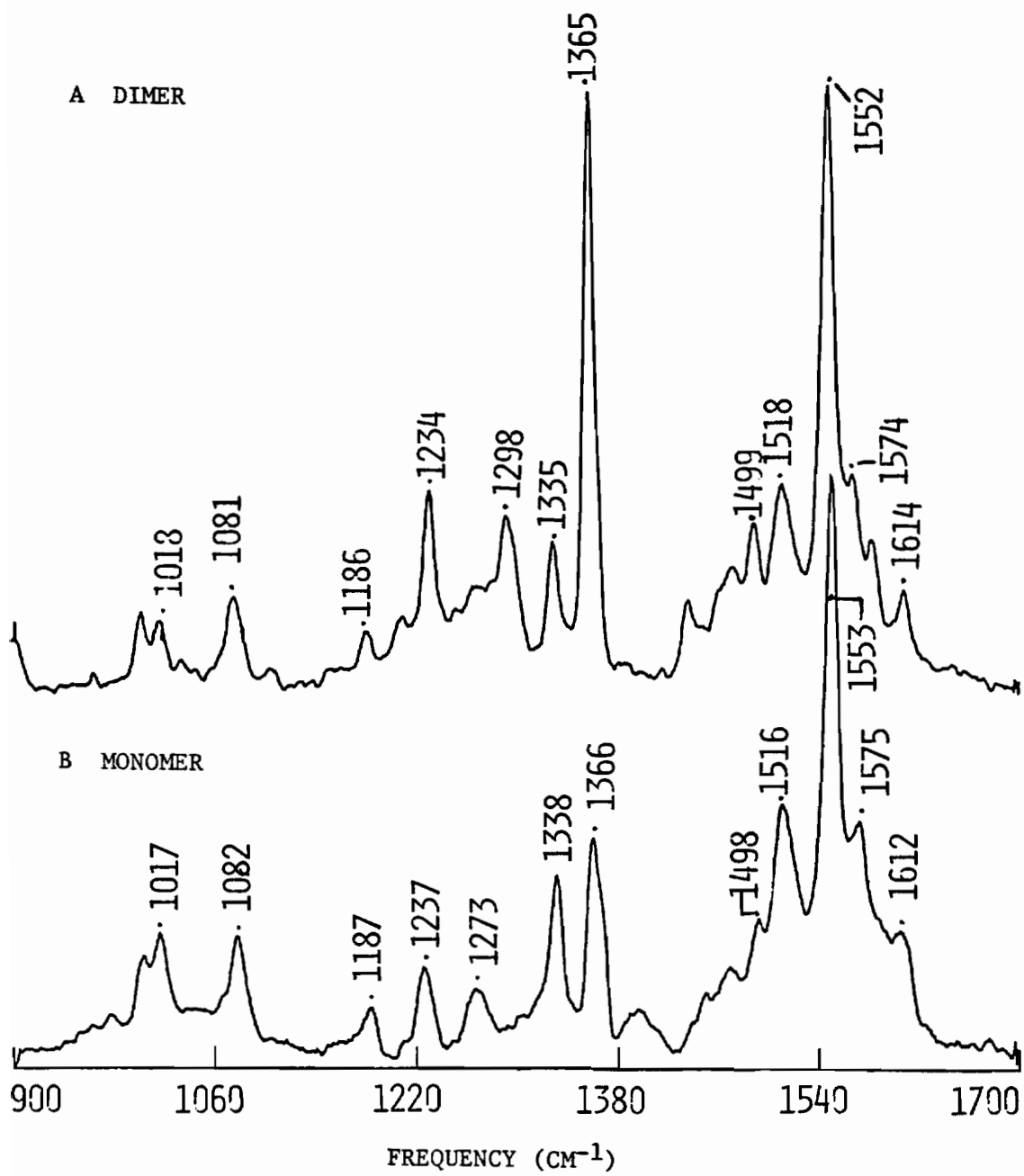


FIGURE 4

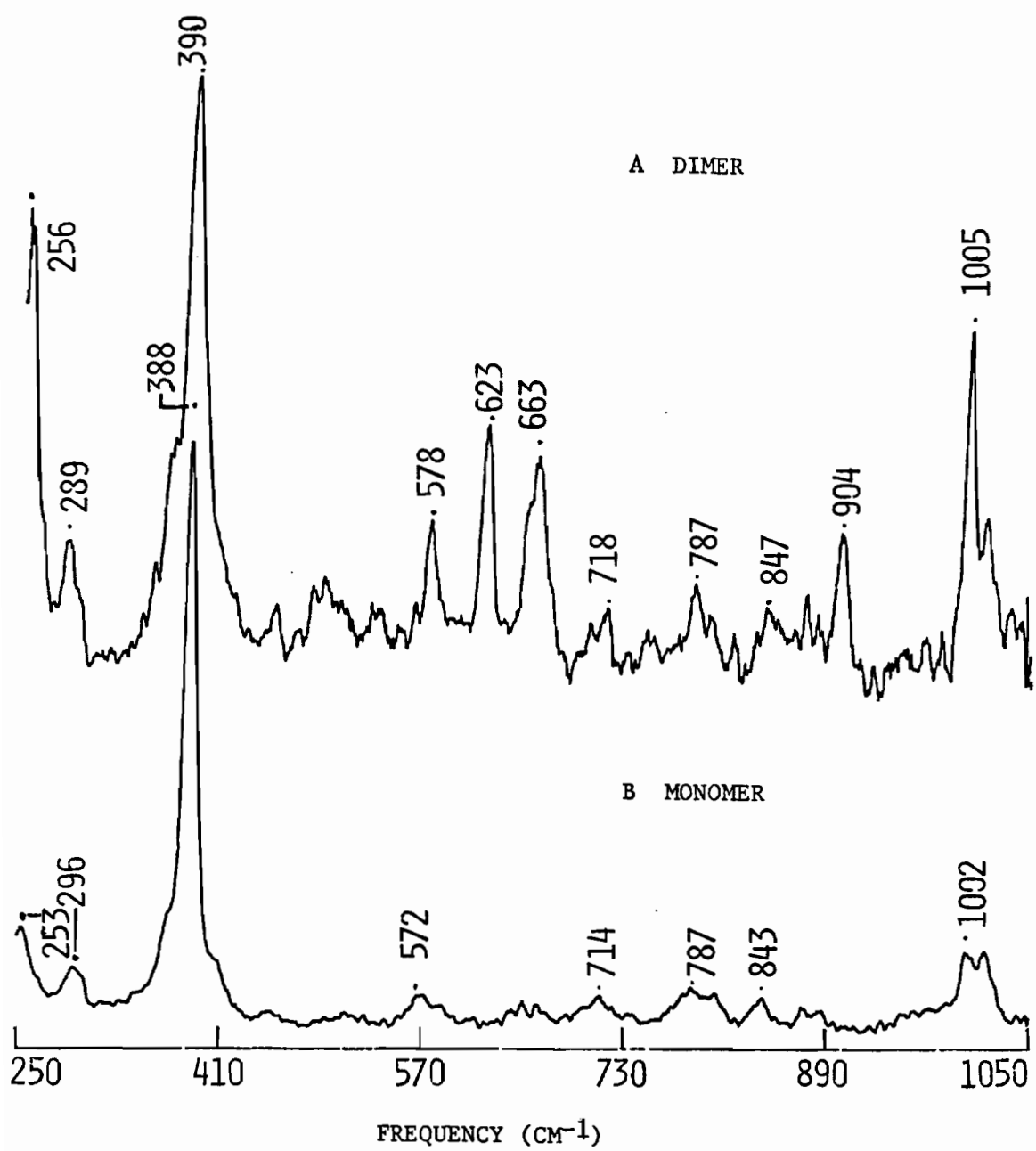
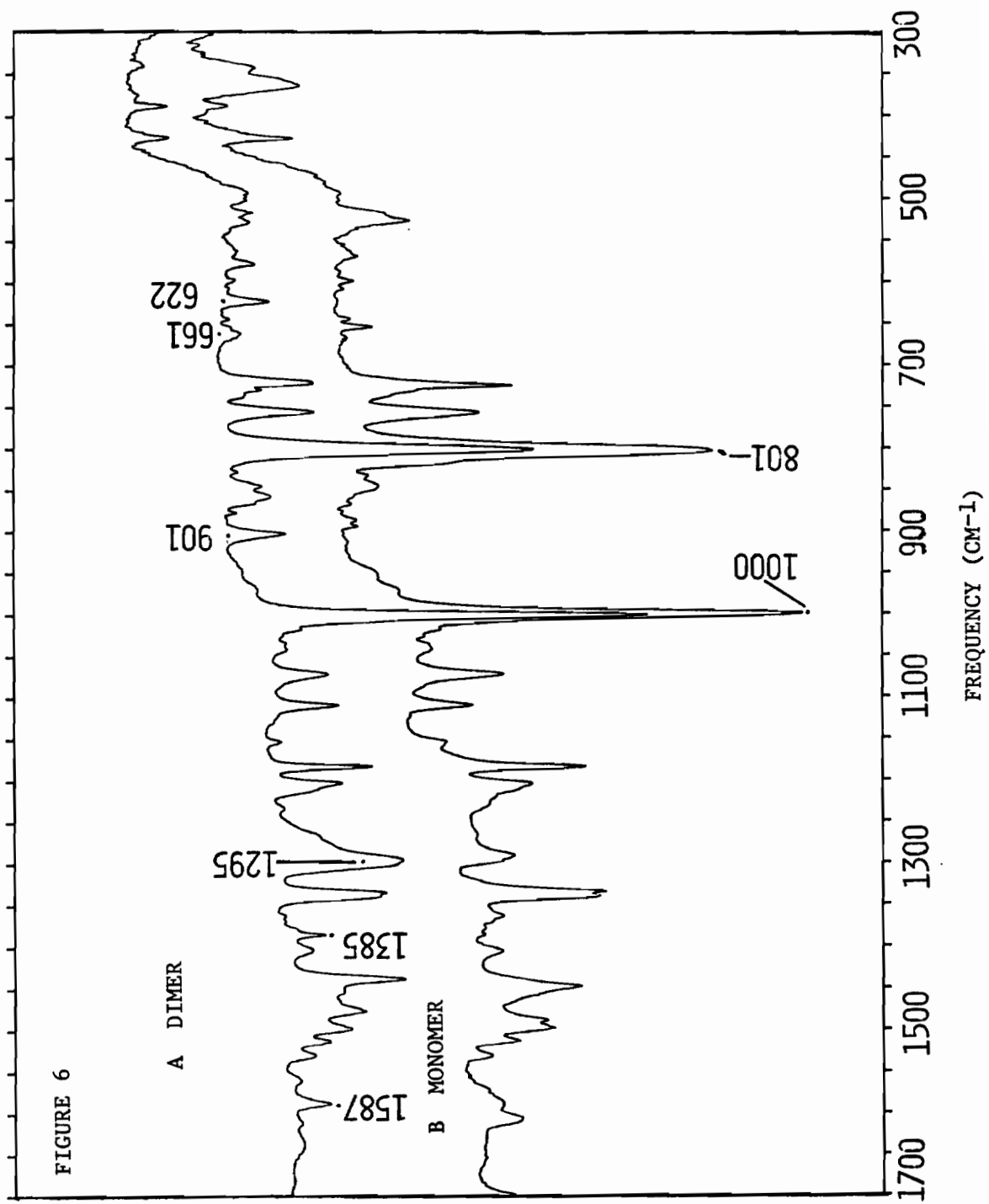


FIGURE 5



APPENDIX

RESONANCE RAMAN STUDIES OF CYTOCHROME c_1 AND c . A COMPARATIVE STUDY WITH AND WITHOUT HINGE PROTEIN

INTRODUCTION

Cytochromes abound in aerobic cells and play vital roles in the respiratory chain. Various cytochromes present in mitochondrial electron transport chain are cytochromes b , c_1 , c , a_1 , and a_3 . All the cytochromes have heme or modified heme as the prosthetic group. Cytochromes c and c_1 differ from other cytochromes in that the heme is covalently attached to the protein through thioether bonds (Fig. 1). These bonds are formed between the sulfhydryl groups of two cysteine residues and the vinyl groups of the heme.

To understand the roles of cytochrome c_1 and c in the electron transport chain in the mitochondrion, it is essential to elucidate their structures and to establish a structure-function relationship. Recently it was discovered that cytochrome c_1 forms a complex with cytochrome c and a mitochondrial protein named 'hinge protein' is essential for their complex formation (1-3).

Resonance Raman (rR) spectra of cytochrome c_1 , cytochrome c , a mixture of the two (with and without hinge protein), and c_1 plus hinge protein were collected. The purpose of the study was to

correlate the vibrational spectra of cytochrome c_1 with those of cytochrome c . Furthermore, we wished to determine whether hinge protein perturbs the vibrational spectra of either of the two cytochromes.

MATERIALS AND METHODS

Triplicate samples* for rR experiments from Drs. Tsao E. King and Chong H. Kim (State University of New York at Albany) arrived frozen and preloaded in capillaries and were used as received. Upon receipt, the samples were immediately stored at -40° C. For each Raman experiment, a single capillary was removed from the freezer and kept in liquid nitrogen until it was put in the sample Dewar. Just before the start of the experiment, the capillary was taken out of liq. N_2 , quickly wiped and placed in the Dewar fitted with a copper rod cold finger (sample temperature,

-
- *#1. Cytochrome c_1 (0.5 mM in 50 mM phosphate buffer (pH 7.4) + 1% cholate)
- #2. Cytochrome c_1 + hinge protein (H.P.), (same medium as in #1).
- #3. Cytochrome c (Horse Heart Type III), (0.5 mM in 50 mM phosphate buffer, pH 7.4).
- #4. Cytochromes c_1 + c (0.3 mM each in 50 mM phosphate buffer, pH 7.4).
- #5. Cytochromes c_1 + c + H.P. (0.3 mM each in 10 mM phosphate buffer, pH 7.4).

90 K). After the rR experiment, the capillary was again stored at -40°C , but stored separately from the remaining ones. Precautions were taken not to thaw the samples during any of the transfer steps. Excitation was provided by a Spectra-Physics argon ion laser (164-05), and our Raman spectrophotometer and computer interface have been described elsewhere (4). The rR spectra of the frozen samples were obtained in the high frequency region ($1000\text{--}1700\text{ cm}^{-1}$) with excitations of 457.9 and 514.5 nm using a back-scattering geometry. The conditions used were 90 K, a laser power of 90 mW at the sample Dewar, a slit width of 4 cm^{-1} and a scanning speed of $2\text{ cm}^{-1}\text{s}^{-1}$ for 514.5 nm excitation. Multiple scans were co-added to improve the signal-to-noise ratio.

RESULTS AND DISCUSSION

The rR spectra of \underline{c}_1 (sample #1), \underline{c} (sample #3) and the $\underline{c}_1 + \underline{c}$ mixture (sample #4) are compared in Figure 2. Figure 3 displays the rR spectra of \underline{c}_1 with and without hinge protein (samples #1 and #2). In Figure 4, the rR spectra of the mixture ($\underline{c}_1 + \underline{c}$) with and without H.P. are presented (samples #4 and #5). Table I gives a summary of some key vibrational frequencies of spin- and oxidation-state marker bands of heme proteins. A list of vibrational frequencies of all the samples is displayed in Table II.

Resonance Raman spectroscopy has been used extensively in the studies of numerous heme enzymes and heme proteins (including cytochrome \underline{c}) and shown to be extremely diagnostic of a variety of

prosthetic group properties, including oxidation and spin states of the metal ion, core size of the porphyrin ring, and environmental effects. Alteration of excitation wavelengths brings out different vibrational bands, especially in the high frequency region of 1000–1700 cm^{-1} , and their intensities serve to identify these modes. Excitation within the intense B band (near Soret around 400 nm) generally produces enhancement of Raman peaks from totally symmetric modes of vibration, and have been particularly characteristic of spin and oxidation states. Excitation within Q_0 and Q_1 bands at $\sim 500 - 550$ nm enhances peaks associated with those of non-totally symmetric modes.

To assign the spin and oxidation states in \underline{c}_1 and \underline{c} , we have focused on prominent peaks from the rR spectra of various heme proteins (5). The peaks that are most informative of the oxidation and spin states are the modes ν_4 , ν_{19} , ν_{10} and ν_3 . Literature values for the so called oxidation-state marker band ν_4 (insensitive to spin state) lie in the frequency ranges 1355–1365 cm^{-1} for Fe(II) and 1370–1380 cm^{-1} for Fe(III). An excellent spin-state marker band is ν_{19} (insensitive to oxidation state), occurring within the frequency regions of 1580–1590 cm^{-1} and 1550–1578 cm^{-1} for low spin and high spin Fe complexes, respectively. Another important band is ν_3 which is helpful in determining the spin-state of Fe(II) complexes, its respective values for low and high spin Fe(II) being ~ 1490 and ~ 1470 cm^{-1} . The ν_3 for low spin Fe(III) exists between 1490–1505 cm^{-1} and is lower by about 10 cm^{-1} for high spin complexes. The peak assigned to ν_{10} is sensitive to both oxidation and spin-states and exists at

$\sim 1636 \text{ cm}^{-1}$ and $\sim 1620 \text{ cm}^{-1}$ for low spin Fe(III) and low spin Fe(II) complexes, respectively. The frequency for high spin complexes is lower by at least 10 cm^{-1} than that for the low spin form in the same oxidation state. These values are summarized in Table I.

The rR spectra of \underline{c} (ferric) obtained with near-Soret excitation at 457.9 nm (inset in Fig. 2) and with 514.5 nm excitation (all other spectra shown) were identical to the respective spectra reported previously (6, 7^a). Cytochrome \underline{c}_1 produced a very strong fluorescence background on laser illumination at 457.9 nm (owing to detergent?), but visible excitation (514.5 nm) produced lower fluorescence and satisfactory results. The vibrational spectral features of \underline{c}_1 resembled those of \underline{c} in both frequencies and intensities in the region below 1350 cm^{-1} but varied considerably above 1350 cm^{-1} , where \underline{c} and \underline{c}_1 showed markedly different frequencies (Fig. 2A and 2B). The most prominent difference in the rR spectra of the two cytochromes is the presence of unique peaks at 1360, 1545, and 1625 cm^{-1} for \underline{c}_1 and at 1371, 1560, and 1636 cm^{-1} for \underline{c} . Furthermore, for \underline{c}_1 , the peak at 1128 cm^{-1} was less intense and the spectral regions 1560–1600, 1425–1530 and $1080\text{--}1200 \text{ cm}^{-1}$ have broad, anomalous background humps not observed for \underline{c} .

The oxidation state marker band ν_4 for \underline{c}_1 is at 1360 cm^{-1} whereas that for \underline{c} is $\sim 1370 \text{ cm}^{-1}$ and are characteristic of Fe(II)

^aAdar (7) used an excitation of 530.9 nm, whereas we used 514.5 nm; however both wavelengths are in the visible region and data should be comparable.

and Fe(III) complexes, respectively^a. ν_{10} is found at 1625 cm^{-1} for \underline{c}_1 and at 1636 cm^{-1} for \underline{c} , supporting that \underline{c}_1 is low-spin Fe(II) and \underline{c} is low-spin Fe(III), as expected for six coordinate cytochromes with strong field axial ligands. Furthermore, the ν_{19} of \underline{c}_1 at 1589 cm^{-1} and of \underline{c} at 1584 cm^{-1} are also consistent with the above observations that \underline{c}_1 has a low-spin ferroheme and \underline{c} has a low-spin ferriheme. Other spectral features, such as ν_{11} and ν_{20} or ν_{29} (\underline{c} has ν_{11} at 1560 and ν_{20} or ν_{29} at 1400 cm^{-1} whereas \underline{c}_1 has them at 1545 and 1395 cm^{-1} , respectively) also show that \underline{c} has a low-spin Fe(III) whereas \underline{c}_1 has a low-spin Fe(II)^b.

The rR spectrum of the mixture of $\underline{c}_1 + \underline{c}$ (Fig. 2C) is strongly reminiscent of that of \underline{c}_1 alone. In addition, the broad background humps observed for pure \underline{c}_1 are minimized and the sample fluorescence is considerably lower, thus resulting in a high quality spectrum for sample #4. The position of all the characteristic rR marker bands indicates that the cytochromes in this sample are both predominantly in the low spin Fe(II) configuration.

Although the individual components of \underline{c} and \underline{c}_1 exist as low spin

^aWith Soret excitation, ν_4 at 1374 cm^{-1} in \underline{c} is the strongest band in the spectrum and confirmatory of Fe(III) [Fig. 2, inset].

^bAlthough the spectral features of \underline{c}_1 are characteristic of low-spin Fe(II), the observation of a peak at $\sim 1470\text{ cm}^{-1}$ (which can be assigned as ν_3 for high-spin Fe(II)) suggests the possibility of traces of high-spin Fe(II) in all the samples containing \underline{c}_1 .

Fe(III) and Fe(II), respectively, their mixture behaves as low spin Fe(II) only. On this basis, it can be argued that in the mixture, \underline{c}_1 reduces \underline{c} to Fe(II) [consistent with redox potentials of 260 mV and 220 mV for \underline{c} and \underline{c}_1 , respectively] and that the resulting Fe(III) \underline{c}_1 is then photoreduced upon laser irradiation.

The effect of hinge protein on the rR spectrum of \underline{c}_1 is shown in Figure 3. Very similar spectral features are seen for $\underline{c}_1 \pm$ H.P.. Moreover, similar results are observed in the rR spectra of a mixture of the two cytochromes \pm H.P. (Fig. 4). These observations suggest that H.P. does not contribute to or perturb the vibrational frequencies of the cytochromes. Hence it must be concluded that the rR technique is insensitive toward elucidating the interaction between H.P. and \underline{c}_1 by following the vibrational modes of the chromophores. Presumably the hinge protein has little influence on the cytochrome electronic properties that would be "visible" in the rR spectrum.

In the spectra of the mixture \pm H.P. in Figure 4, the spectral features at 1625, 1585, 1545, 1494 and 1360 cm^{-1} correspond to ν_{10} , ν_{19} , ν_{11} , ν_3 and ν_4 respectively, and are all characteristic of a Fe(II) low-spin system. Again, no effect of H. P. on the rR spectra is observed.

REFERENCES

1. Kaminsky, L. S., Chiang, Y.-L., Yu, C.-A., and King, T. E. (1974) Biochem. Biophys. Res. Commun. 59, 688-692.
2. Chiang, Y.-L., Kaminsky, L.S., and King, T. E. (1976) J. Biol. Chem. 251, 29-36.
3. Kim, C. H., and King, T. E. (1983) J. Biol. Chem. 258, 13543-13551.
4. Loehr, T. M., Keyes, W. E., and Pincus, P. A. (1979) Anal. Biochem. 96, 456-463.
5. a) Spiro, T. G. (1983) in Iron Porphyrins, Part II (Lever, A. B. P., and Gray, H. B., eds.) Chap.3, Addison Wesley, Reading, MA.
b) Carey, P. R. (1982) in Biochemical Applications of Raman and Resonance Raman Spectroscopies, Chap. 5, Academic Press, N. Y.
c) Choi, S., Spiro, T. G., Langry, K. C., Smith, K. M., Budd D. L., and La Mar, G. N. (1982) J. Am. Chem. Soc. 104, 4345-4351.
d) Spiro, T. G., and Burke, J. M. (1976) J. Am. Chem. Soc. 98, 5482-5489.
6. Myer, Y. P., Srivastava, R. B., Kumar, S., Raghavendra, K. (1983) J. Protein Chem. 2, 13-42.
7. Adar, F. (1978) J. Phys. Chem. 82, 230-234.

Table I. Key Resonance Raman Frequencies (in cm^{-1}) for Heme Proteins

	ν_4	ν_3	ν_{19}	ν_{10}
Fe(III) low-spin	1370–1380	~1490–1505	1580–1590	~1636
high-spin	"	~1480–1500	1550–1578	~1626
Fe(II) low-spin	1355–1365	~1490	1580–1590	~1620
high-spin	"	~1470	1550–1578	~1610

Table II. Vibrational Frequencies (in cm^{-1}) of all the Samples.

\underline{c}_1	$\underline{c} + \text{H.P.}$	\underline{c}	$\underline{c}_1 + \underline{c}$	$\underline{c}_1 + \underline{c} + \text{H.P.}$	Assignments
1129 s	1128 s	1127 vs	1128 vs	1127 vs	
1151 w,br	1148 m	1153 m	1153 m	1153 m	
1174 s	1174 s	1173 vs	1173 s	1173 s	
1215 m	1214 w	*	1215 vw	1215 vw	
1230 s	1230 m	1231 s	1230 s	1230 s	
1244 m	1244 w	1247 [#] w	1243 sh	1243 sh	
1312 vs	1312 vs	1309 s	1310 vs	1310 vs	
1361 s	1360 s	1374 [#] vs	1360 s	1360 s	ν_4
1395 m	1395 m,br	1400 m	1397 m	1396 m	
1466 br	1470 br	*	1472 vw	1478 vw	
1491 br	1493 br	1500 [#] s	1496 w	1494 w	ν_3
1545 m	1545 m	*	1545 m	1545 m	ν_{11}
*	*	1560 s	*	*	ν_{11}
1589 m	1589 m	1585 s	1585 m	1585 m	ν_{19}
1626 m	1629 m	*	1625 m	1625 w	ν_{10}
?	?	1637 s	*	*	ν_{10}

vs= very strong, s= strong, m= medium, w= weak, br= broad,

*= possibly at noise level, ? = questionable peak, # = seen with Soret excitation.

FIGURE LEGENDS

Figure 1. Prosthetic group of cytochromes \underline{c}_1 and \underline{c} .

Figure 2. Resonance Raman spectra of cytochromes \underline{c} and \underline{c}_1 .

Conditions used are: (A) Cytochrome \underline{c}_1 (0.5 mM sample #1), 514.5-nm excitation, laser power of 90 mW, scan rate of $2 \text{ cm}^{-1} \text{ s}^{-1}$, slitwidth of 4 cm^{-1} , temperature of 90K, 150° back-scattering geometry, with 9 scans and 17 point smooth.

(B) Cytochrome \underline{c} (0.5 mM, sample #3) with 13 point smooth, other conditions same as in (A).

(C) Mixture of cytochrome \underline{c}_1 and \underline{c} (0.3 mM each, sample #4) with 9 point smooth, other conditions same as in (A).

Inset: Cytochrome \underline{c} (Fe^{+3}) (0.5 mM, sample #3), 457.9-nm excitation, scan rate of $1 \text{ cm}^{-1} \text{ s}^{-1}$, slitwidth of 5 cm^{-1} , 50 mW power at the sample dewar, with a total scans of 4. Other conditions same as in 2A.

Figure 3. Resonance Raman spectra of cytochrome \underline{c}_1 with and without hinge protein.

(A) Same spectra as in Figure 2A.

(B) Cytochrome \underline{c}_1 + hinge protein (0.5 mM, sample #2), all other conditions same as in Figure 2A.

Figure 4. Resonance Raman spectra of cytochrome $c_1 + c$ with and without hinge protein.

(A) Cytochrome $c_1 + c$ with hinge protein (0.3 mM each, sample #5) with 9 point smooth. Other conditions same as in Figure 2A.

(B) Mixture of cytochrome c_1 and c (sample # 4), same spectra as in Figure 2C.

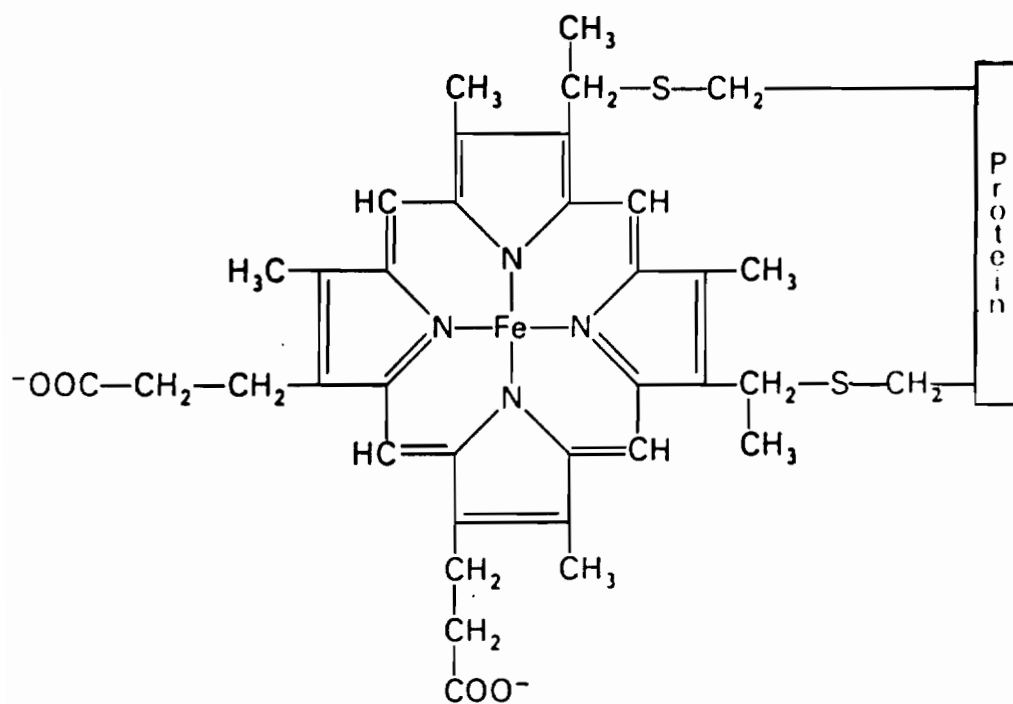


FIGURE 1

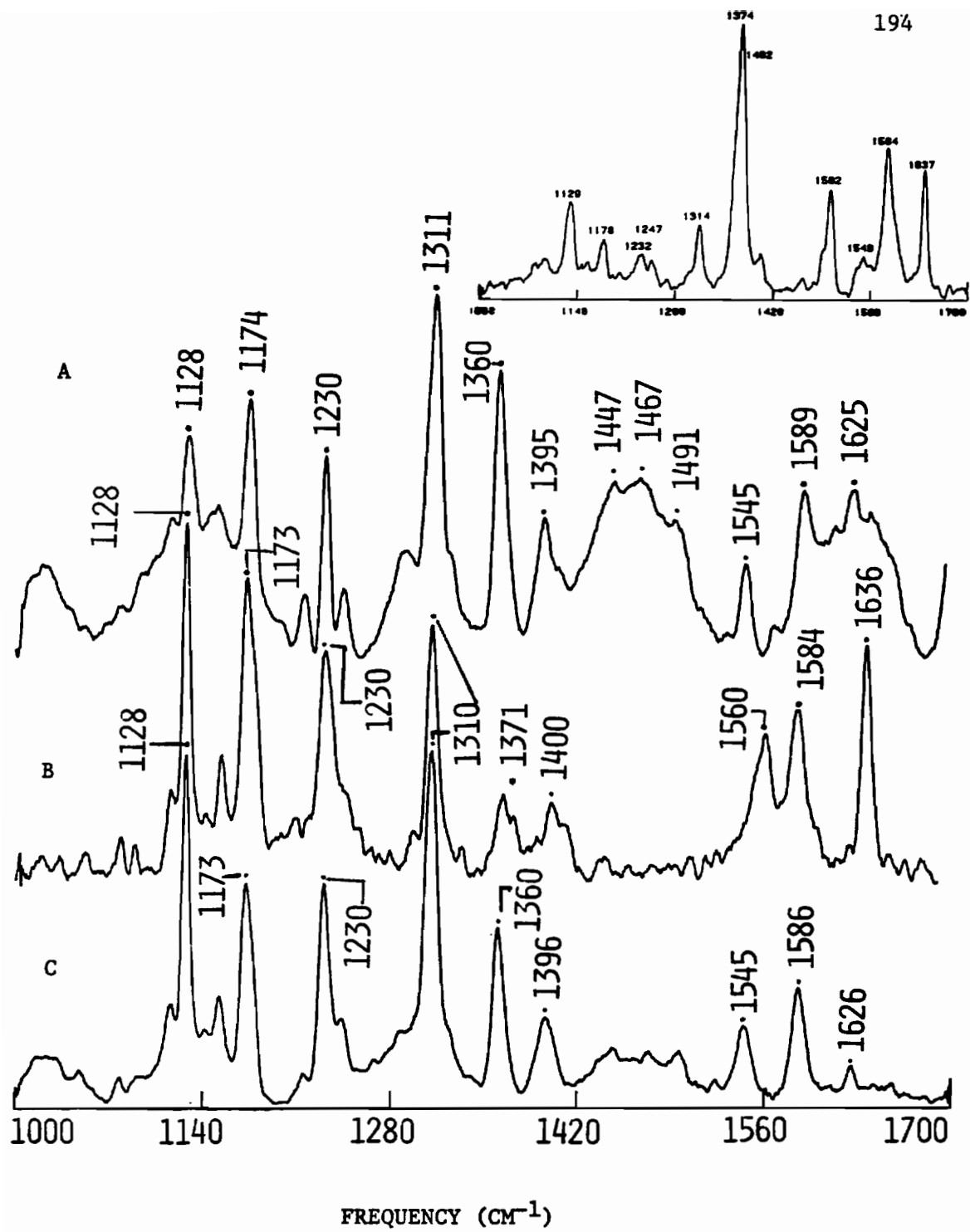


FIGURE 2

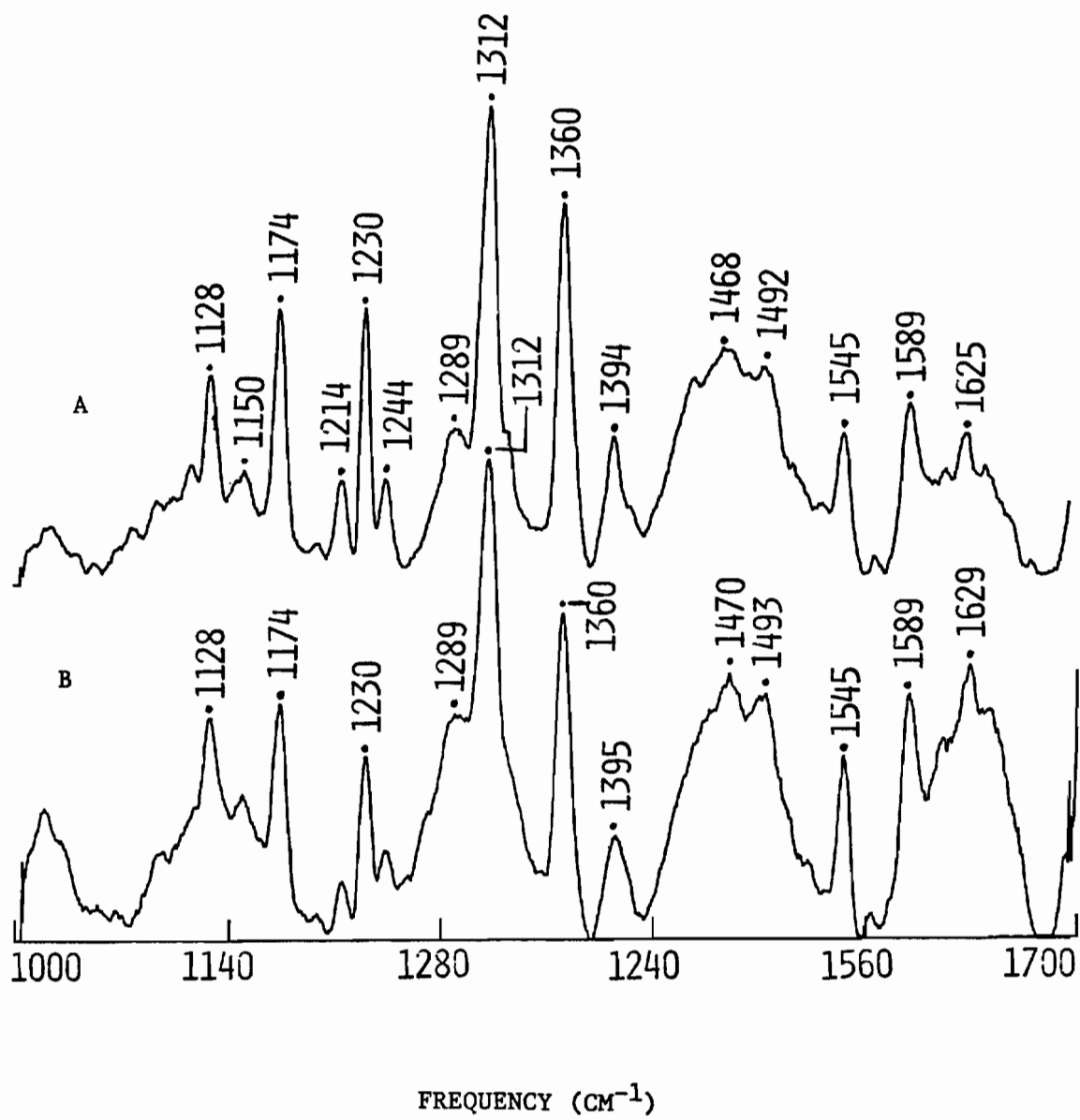


FIGURE 3

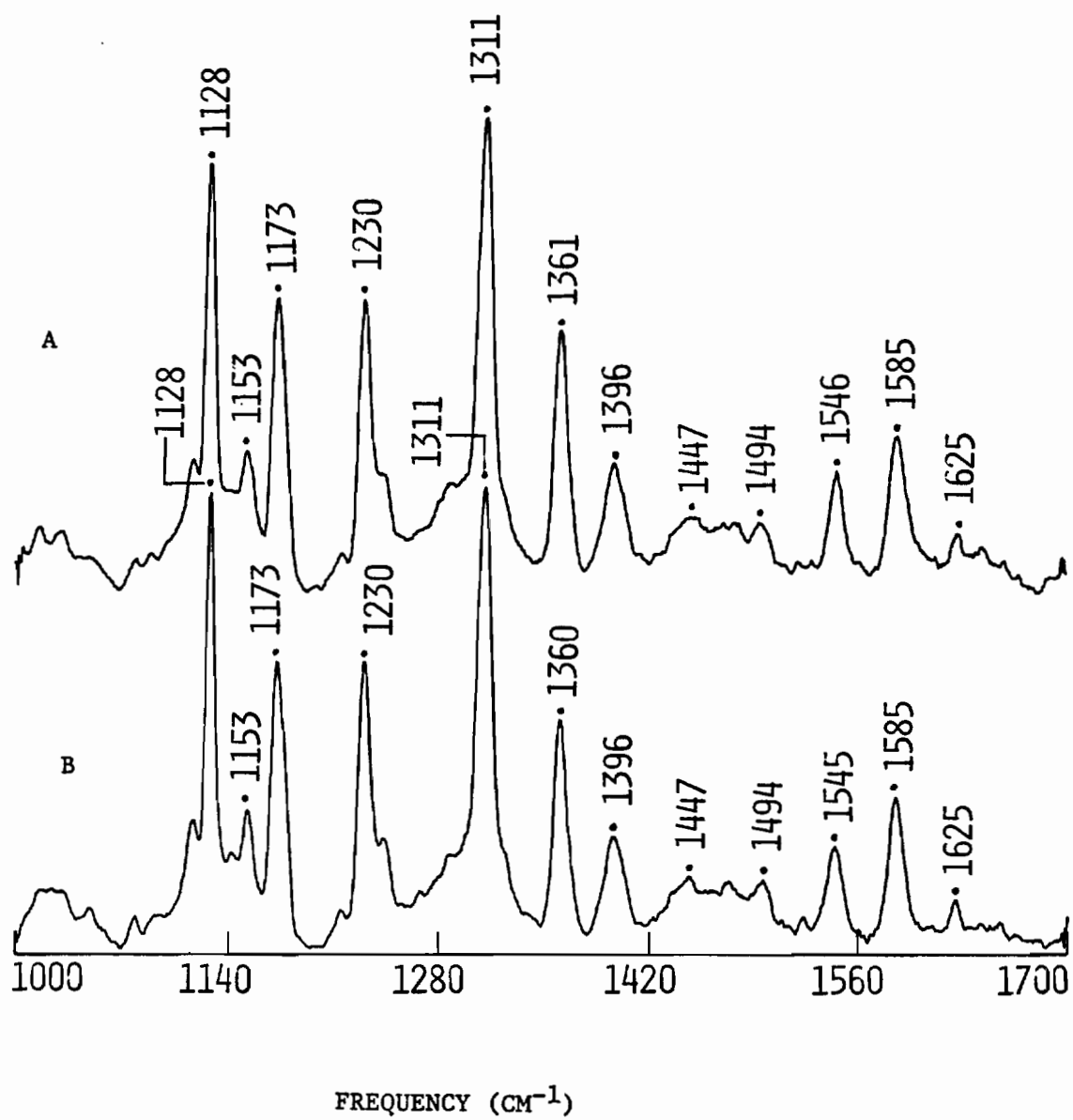


FIGURE 4

BIOGRAPHICAL NOTE

The author was born on May 1, 1946 in Khidim in the western foothills of the Himalayas in Nepal. She received her primary and high school education in Burma. She obtained her B.S. in 1970 and her M.S. in chemistry in 1973 from the University of Meerut (India). In the fall of 1973 she joined Tribhuwan University in Kathmandu, Nepal, as an assistant lecturer and was promoted to a lecturer in 1974. She came to the United States as a Fulbright scholar in 1981 and enrolled at the University of Oregon, Eugene. She graduated with an M.S. in chemistry in December 1983. The author then entered the Oregon Graduate Center in January 1984 to pursue her Ph.D. degree in Biochemistry. After finishing her degree, the author will return to Nepal to continue her teaching career at Tribhuwan University.